

Microfluidic-integrated vertical electrodes employed in impedance-based cytometry. Potential application in immunotherapies.

THÈSE N° 7367 (2016)

PRÉSENTÉE LE 19 DÉCEMBRE 2016

À LA FACULTÉ DES SCIENCES ET TECHNIQUES DE L'INGÉNIEUR
CHAIRE SWISS-UP EN INGÉNIERIE - LABORATOIRE D'ÉLECTRONIQUE POUR LES SCIENCES DU VIVANT
PROGRAMME DOCTORAL EN MICROSYSTÈMES ET MICROÉLECTRONIQUE

ÉCOLE POLYTECHNIQUE FÉDÉRALE DE LAUSANNE

POUR L'OBTENTION DU GRADE DE DOCTEUR ÈS SCIENCES

PAR

Enrica ROLLO

acceptée sur proposition du jury:

Dr G. Boero, président du jury
Prof. C. Guiducci, directrice de thèse
Prof. D. Di Carlo, rapporteur
Prof. A. Hierlemann, rapporteur
Prof. Y. Leblebici, rapporteur



ÉCOLE POLYTECHNIQUE
FÉDÉRALE DE LAUSANNE

Suisse
2016



To my dad,

always with me.

ACKNOWLEDGMENTS

I owe my deepest gratitude to my supervisor, Prof. Carlotta Guiducci, who gave me the opportunity to work in an exceptional research environment, guiding and encouraging me over all these years. She has been supportive since my first day the lab representing a constant source of enthusiasm and optimism in my research. Thanks for your scientific guidance and above all your friendship.

I would like to thank the members of my thesis committee Prof. Giovanni Boero and Prof. Yusuf Leblebici from EPFL, Prof. Dino Di Carlo from UCLA-Los Angeles and Prof. Andreas Hierlemann from ETH-Zurich for their insightful comments and valuable feedback.

I acknowledge our collaborators in Ludwig Centre, for providing us the samples for the experiments and for the helpful discussions. Furthermore, I want to thank all the staff in the Center of Micro- and Nanotechnology (CMi) at EPFL for the constant availability and for the many useful hints.

I am very grateful to Enrico Tenaglia for his scientific advices, many insightful discussions and suggestions. He assisted me in researching, conducting the experiments and he was essential helping me with this thesis. Thanks Enrico for your continuous support and our nice chats. I want to thank all my current and former colleagues and students of the lab, you made CLSE a pleasant place for working and learning and also a funny and joyful place where I have collected many precious memories.

I am grateful to all the friends I met in Lausanne, in particular Luisa and Ana for making the atmosphere of our flat always so friendly and familiar. Thanks to Cristina and Enrica for your encouragement, empathy and most of all your humor, in particular during the intense last year of my PhD. Thanks to my dear friends Ste, Marco M., Anna and Emma, who despite the distance were always present with a word of support or a listening ear.

Thanks to all those who have crossed my path and have left a mark during this journey. In particular to all the friends of the association 2HE and the group of IoPosso: ragazzi insieme siete una bomba di contagiosa solidarietà, allegria e positività!

A special thanks to my family, la mia “Meravigliosa Famiglia”. During these years our lives have been full of surprises that weren't always good. We have faced and enjoyed anyway each single moment, finding the strength in our union, always. Mamma, Gio e Rob siete le donne che mi ispirano ogni giorno: forti, determinate e piene d'amore. Gae e Ale siete due uomini unici e due cognati speciali di cui sono sempre più orgogliosa. To my dad who is always in my thoughts, you are missed. To my three nieces, my nephew and the fifth one who will arrive, you are the twinkle in my eyes, the source of happiness and entropy of the family, I love you so.

ABSTRACT

During the last decades, the growing interest for single-cell analysis has led to the creation of a number of microfluidic and lab-on-a chip (LOC) platforms for characterizing cellular samples. In that context label-free based platforms are minimally invasive and offer the notable advantages of reducing alteration of the analyzed sample and granting its re-employment.

The study of intrinsic features of single cells independent from markers is commonly attained using electrical and mechanical-based techniques. Electrical-based techniques have been widely employed in LOC applications, both for characterizing and for manipulating cell samples. The translation of these approaches to single-cells necessitates microelectrodes that can be singularly addressed and arranged in a high-density topography.

This thesis provides two fabrication solutions that comply with these requirements and allow to manufacture highly conductive vertical platinum microelectrodes with high aspect-ratio.

According to the two processes reported, the three-dimensional (3D) cores of the electrodes are fabricated in SU-8 or in silicon respectively. These tridimensional structures are successively coated by a metal layer, after a passivation step in the case of silicon. The planar metal connections which singularly address the free-standing microelectrodes are patterned differently for the two approaches, respectively by lift-off and spray coating. Importantly, the 3D microelectrodes can be co-fabricated with microfluidic structures to obtain multiple active sites for single-cell analysis.

In this thesis, in the framework of a collaboration with Ludwig Centre for Cancer Biology (Lausanne, Switzerland), the microelectrodes have been employed to detect activated T cells.

The encouraging results pave the way to a new generation of microfluidic platform based on 3D microelectrodes to attain real-time and label-free monitoring of individual T cells to employ in immunotherapy.

Keywords

Vertical microelectrodes, electrical impedance, microfluidics, microfabrication, activated T cells, immunotherapy, SU-8, silicon.

SOMMARIO

Negli ultimi decenni il crescente interesse per le analisi di singole cellule ha portato alla fabbricazione di un ampio numero di dispositivi microfluidici e sistemi 'Lab-on-a-chip' (LOC) per la caratterizzazione di campioni cellulari. In tale contesto, piattaforme che non richiedono l'utilizzo di marcatori -dette 'label-free'- si distinguono per essere minimamente invasive ed offrono il notevole vantaggio di ridurre l'alterazione del campione e di garantire il suo ri-utilizzo.

Lo studio delle caratteristiche intrinseche delle singole cellule indipendente da marcatori è comunemente ottenuto attraverso tecniche elettriche e meccaniche. Tecniche basate su campi elettrici sono ampiamente utilizzate in applicazioni LOC sia per la caratterizzazione che per la manipolazione di campioni cellulari. L'applicazione di questi approcci a singola cellula necessita di microelettrodi che possono essere singolarmente contattati e disposti secondo una topografia ad alta densità.

In questa tesi sono proposte due soluzioni di microfabbricazione che rispondono a questi requisiti e permettono di fabbricare microelettrodi verticali in platino altamente conduttivi e ad alto aspect-ratio.

Secondo i processi proposti, le strutture interne degli elettrodi sono rispettivamente fabbricate in SU-8 o in silicio. Tali strutture tridimensionali (3D) sono successivamente ricoperte da uno strato metallico, dopo la loro passivazione nel caso del silicio. Le connessioni metalliche planari che contattano singolarmente i microelettrodi sono definite in modo diverso per i due processi, rispettivamente per mezzo di tecniche di microfabbricazione di lift-off e spray coating. È importante inoltre osservare che i microelettrodi 3D possono essere anche co-fabbricati con strutture microfluidiche al fine di ottenere siti attivi multipli per analisi di cellule singole.

In questo studio, i microelettrodi sono stati utilizzati per individuare cellule T attivate, nel contesto di una collaborazione con l'istituto oncologico Ludwig (Losanna, Svizzera). I promettenti risultati finora ottenuti aprono la strada ad una nuova generazione di dispositivi microfluidici basati su microelettrodi 3D per monitorare singole cellule T da impiegare nel contesto dell'immunoterapia.

Parole chiave

Microelettrodi verticali, impedenza, microfluidica, microfabbricazione, cellule T attivate, immunoterapia, SU-8, silicio.

CONTENTS

Abstract	i
Sommario	iii
Contents	v
List of Figures	ix
List of Tables	xv
List of Equations	xvii
Introduction	1
Objectives and Organization of the Thesis	2
1 Impedance-based cell analytics on a chip	5
1.1 Fundamentals of Electrical Impedance Spectroscopy (EIS): theory and methods.....	5
1.1.1 Fundamentals of EIS.....	5
1.1.2 Equivalent circuit of the impedance of an object.....	8
1.1.3 Equivalent electric model of a single cell in suspension	11
1.2 Cell characterization based on electrical measurements	12
1.2.1 Cells in culture.....	14
1.2.2 Single-cells in suspension.....	16
1.3 Impedance microfluidic cytometry	19
1.3.1 Microelectrodes configurations.....	19
2 Metal-Coated SU-8 Structures for 3D Microelectrode Arrays	27
2.1 Fabrication of 3D electrodes integrated in microfluidic structures	27
2.1.1 Fabrication of metal-coated SU-8 micropillars.....	28
2.1.2 Patterning of Connection Lines.....	29
2.1.3 Integration of 3D Pillars into Microfluidic Channels	31
2.2 Electrical Characterization of the 3D Electrodes.....	32

2.2.1	Conductivity measurements	32
2.2.2	Impedance spectroscopy on microfluidic-integrated vertical electrodes	34
2.3	Summary	35
3 	Metal-coated silicon micropillars for freestanding 3D-electrode arrays.....	37
3.1	Introduction	37
3.2	Fabrication of 3D silicon-based electrodes.....	38
3.2.1	Microfabrication process of metal-coated silicon microelectrodes	38
3.2.2	Electron microscopy characterization of micropillar arrays and their connection lines	40
3.3	Electrical characterization of microelectrodes	42
3.3.1	Resistivity of micropillar arrays	42
3.3.2	Impedance characterization of free-standing micropillar electrodes	45
3.4	Integration of microelectrodes with SU-8 microfluidic structures	48
3.4.1	Fabrication process of SU-8.....	48
3.4.2	Impedance characterization of micropillar electrodes combined with SU-8 microfluidic structures	49
3.5	Summary	52
4 	Application of 3D microelectrodes: towards label-free sensing of single activated T cells ..	55
4.1	Introduction	56
4.1.1	The role of T cells and their activation	56
4.1.2	Label-free strategies on chip for the detection of Activated T cells.....	59
4.1.3	Electrical-based on chip solutions for activated T cells detection and characterization	61
4.2	Materials and methods	62
4.2.1	Device fabrication.....	62
4.2.2	Impedance-based characterization of cells in flow	64
4.2.3	Activation of CD8 ⁺ T lymphocytes and preparation of mixtures.....	65
4.2.1	Preparation of polystyrene beads mixtures.....	68
4.3	Results and discussion.....	68
4.3.1	Discrimination of polystyrene particles based on their size.....	69
4.3.2	Cell impedance measurements	75

4.4 Summary	80
5 Conclusions and future works	83
5.1 Summary of achievements	83
5.1 Future perspectives	84
References.....	89
Curriculum Vitae.....	105

LIST OF FIGURES

Figure 1.1: Graphical representation of impedance on complex-plane plot.....	6
Figure 1.2: Simplified model of parallel plate electrodes separated by a material to study.	7
Figure 1.3: Schematic representation of Stern model of electrical double layer at metal-electrolyte interface. The inner Helmholtz plane (IHP) and outer Helmholtz plane (OHP) are shown with the Stern and diffuse layers. The IHP refers to the distance of specifically adsorbed ions on the electrode surface. The OHP refers to the distance of the solvate ions, non-specifically adsorbed. The separation between the different charges results in a potential drop across the Helmotz planes establishing a double layer capacitor. Adapted from [19].....	9
Figure 1.4: Equivalent circuit model for a non-faradaic IS biosensor.	11
Figure 1.5: Modelling of a cell by means of: (a) a single-shell model, including cell membrane and cytoplasm and (b) a double-shell model including cell membrane, cell cytoplasm and nucleus.	12
Figure 1.6: Electrical model for a single cell suspended in a sensing region defined by the microelectrodes	13
Figure 1.7: Schematic of the typical ECIS setup. A small AC signal is applied between the WE and CE. A series resistance provides a constant current that makes the voltage measured by the lock-in proportional to the impedance of the system. WE typically has a smaller surface than the CE to ensure the impedance measurement is dominated by the cell layer on the WE; otherwise, the impedance of the medium bulk would screen the contribution of the interface.	14
Figure 1.8: Representation of two widely employed electrode configurations for ECIS: (a) interdigitate electrodes and (b) electrode array	15
Figure 1.9: Schematic representation of Coulter principle.	16
Figure 1.10: Scanning electron microscope images of micro Coulter counters from (a) Satake et al. [71] and (b) Saleh and Sohn [72]. A pair of electrodes are separated by an aperture obtained on a silicon (a) and on a glass substrate (b).....	17
Figure 1.11: (a) Dynamic controllable Coulter aperture ; (b) Experimental demonstration of the stable sheath flows and of the Coulter aperture achieved. [78].....	18
Figure 1.12: (a) [77] Schematic top view of four-channel device based on Coulter counting principle. The device has a common electrode at the entrance of the microchannel and four central electrodes fabricated at the centre of each microchannel; (b) [80] Schematic top view of a multi-aperture Coulter counter for micro particle detection. A polymer membrane with a single microaperture separates each peripheral reservoir and central reservoir.	19
Figure 1.14: Sketch of coplanar microelectrodes configuration.....	20

Figure 1.13: (a) Side view of a particle passing over coplanar electrodes in a microfluidic channel, b) Impedance signal over time. As the impedance is measured differentially the passage of the particle produces both a positive and a negative peak. The time separating the two peaks and the distance between the two electrodes allow to evaluate the speed of the particle in the sensing region. (a) and b) adapted by [22]).	20
Figure 1.15: Schematic view and cross-section views of electrical field distribution for two different electrodes configuration: (a) coplanar and (b) facing electrodes. Adapted by [95].	21
Figure 1.16 Sketch of the possible configurations of facing electrodes in a microfluidic channel: (a) planar facing electrodes, and (b) vertical facing electrodes.	22
Figure 1.17: (a) Differential impedance measurement scheme used with planar facing electrodes configuration. An AC signal is applied at top electrodes. An impedance change is detected when a cell pass through the detection volume. Modified by [93]. (b) Image of the device, modified by [32].	23
Figure 1.18: (a) 3D schematic of the liquid electrodes approach. Large metal electrodes are deposited on the bottom of the secondary channels perpendicular to the main channel. Liquid electrodes refer to the equipotential surfaces at the junctions of the lateral and the main channels. (b) SEM image of C-MEMS electrodes with underneath carbon contacts. [116]	24
Figure 2.1: Schematic of the proposed fabrication processes for free-standing pillar electrodes. The patterning of connection lines by means of lift-off are illustrated. Planar connection lines are patterned by lift-off (a) and SU-8 pillars are patterned on top of the wires (b). The electrodes are covered with a metal film by metal sputtering (c) and the metal on horizontal surfaces is etched away by means of dry etching (d).	28
Figure 2.2 SEM imaging of metal-coated 3D SU-8 pillars (all structures are 50 μm high). Structures resulting from a process making use of lift-off for planar line patterning prior to SU-8 fabrication (a–c). Planar and vertical features combined to show the alignment outcome (b); close-up suggesting conformity of the metal layer (c).	29
Figure 2.3: SEM imaging of SU-8 metal-coated micropillars fabricated on glass substrate.	30
Figure 2.4 SU-8 microfluidic channels integrating 3D electrodes. SEM imaging of sidewall-integrated and free-standing electrodes spanning the entire height of the channel (a-b).	31
Figure 2.5: a) Schematic representation of the section view of the microfluidic channel hosting the microelectrodes. A PDMS cover obtained from an SU-8 mold is bonded on the microchannel fabricated in SU-8. b) SEM imaging of two facing SU-8 metal coated micropillars integrated into a SU-8 microfluidic channel.	32
Figure 2.6: (a) Illustration of the test structures employed to quantify the resistivity of the 3D pillar (red: platinum, green: SU-8); (b) Representation of the sheet resistance of planar wires (experimental points: squares; linear fit: dashed line) and of single vertical sidewalls (experimental points: diamonds; linear fit: dashed and dotted line). Each diamond symbol corresponds to a single structure. The plot reports a total of 15 measurements on 15 different structures (diamonds), plus measurements performed on the planar wires (squares). The inset is a top-view representation of the 3D structures.	33
Figure 2.7: Cartoon representing the test structures to verify the exposure of vertical sidewalls to the solution (top view). SU-8 is indicated in green and coating metal layers in red. 3D pillars extrude by $d'=15\ \mu\text{m}$ from the channel main walls; (b) double layer capacitance of the single electrodes extracted by fitting the electrical equivalent model represented in the inset to a frequency spectrum acquired between 1 kHz and 10 MHz ($d = 100\ \mu\text{m}$: diamonds; $d = 200\ \mu\text{m}$: squares).	34
Figure 3.1: Fabrication process of metal-coated 3D silicon micropillars. Cross section of the silicon chip in correspondence of the microelectrodes array. Resist pattern (a) is transfer into the silicon by Bosch process (b). Silicon is passivated (c) before to cover it with a metal film by metal sputtering (d). The metal	

on horizontal surfaces is patterned by spray coating (e) and etched away by means of dry etching (f). An insulating layer is finally evaporated (g).....	39
Figure 3.2 (a) Section of a 20 μm gap between two 50 μm -high pillars. The colorized SEM picture shows the conformity of the metal layer (Ti/Pt 20/200 nm) on the vertical sides of the pillars and on the gap bottom. Inset: details of the metal layer on the pillar vertical sidewall; (b) vertical sidewall of a pillar. The region marked by the rectangle has been characterized by SEM-EDX and resulted in the spectrum represented in (c).	40
Figure 3.3 (a) Shrinkage of the planar lines due to photoresist overexposure. Dashed black lines indicate the patterns on the original mask design; (b) Bar chart of measured shrinkage over 96 measurements; (c)–(d) patterned connection lines in between pillars for square-shaped pillars with a 20 μm gap and round-shaped pillars with 10 μm gap ((c) and (d), respectively). The nominal width of the lines is 10 μm , 20 μm and 30 μm from bottom to top. Scale bars are 50 μm	42
Figure 3.4: SEM image of three sets of five round-shaped micropillar electrodes. The micropillars have a 30 μm diameter and a 20 μm gap between them. Platinum planar lines from 10 μm to 30 μm in width (bottom to top) connect each single array from point A to point B, through the five pillars. Metal surfaces were highlighted on the image by colorization of the corresponding regions.	43
Figure 3.5 (a) Inter-chip variability (18 chips) of the resistance of the arrays, normalized by the array length, vs. the gap between pillars. In the case of 10 μm gap, three out of 18 normalized resistance values were found to be substantially higher, thus they were indicated separately on the plot; (b) resistance of the arrays normalized by the array length, vs. the gap between pillars. Circles represent 30 μm -width lines and crosses represent 20 μm -width lines. Pillar diameter ranges from 20 μm to 70 μm (b).	44
Figure 3.6: a) Schematic representation of a 3D view of a metal-coated micropillar in a microfluidic channel. b) schematic cross-section and c) top view section of the micropillar.	45
Figure 3.7 Schematic representation of the side view of the microfluidic channel hosting the microelectrodes. A PDMS cover obtained from an SU-8 mould was bonded on the silicon chip by oxygen plasma.	46
Figure 3.8: (a) Impedance modulus and phase of two adjacent micropillar electrodes in dry (solid lines) and wet measurement conditions (dashed line); (b) equivalent circuit of the two pillars in the microfluidic channel used for fitting; (c) fit of the experimental data. Only 101 frequency measurement points out of the 201 sampled are represented on the plot.	47
Figure 3.9: Coloured SEM image of SU-8 microfluidic channel integrating silicon-based 3D microelectrode. The 3D microelectrodes are coloured in green, while SU-8 is colored in violet.	49
Figure 3.10: (a) 3D view of a metal-coated micropillar; (b) the schematic cross-section; and (c) the top view section of the micropillar.	50
Figure 3.11: (a) Top view schematic representation of the current path between two free-standing microelectrodes (in green) and (b) of two microelectrodes with SU-8 extensions (in violet).	51
Figure 3.12: Impedance modulus (a) and phase (b) acquired in wet conditions of two adjacent free-standing micropillar electrodes (blue dots) and integrated in two SU-8 extensions (yellow dots). Microscopy image (101 frequency measurements are represented in the plot).	51
Figure 4.1: Schematic representation of a possible adoptive cell immunotherapy strategy. Tumor mass can be excised from patient to extract T cell population (1). Upon stimulation with specific antigen, activated T cells, which have the desired TCR, can be detected and expanded (2) and then adoptively transferred into patient (3).	57
Figure 4.2: Schematics of the buoyant mass measurement using a suspended microcantilever. Single-cell density is evaluated by loading two different fluids in the channel. At first, the buoyant mass of a cell	

suspended in a low-density fluid is measured from the resonance peak. Then, when the cell enters in a greater density fluid, the direction of the flow is switched and the buoyant mass of the cell is measured in the high-density fluid. Pneumatic vacuum and two computer-controlled solenoid valves are required to control the flow [158]. 60

Figure 4.3: The schematic shows an overview of the microfluidic device. The dashed box shows the position of the impedance sensor in the microfluidic channel. The SEM pictures shows the 3D microelectrodes integrated in SU-8 passive structures (indicated by white arrows). 63

Figure 4.4: a) The sketch schematically shows the chip held in the PCB and docked onto the microscope. A syringe pump system provides the control of the fluid in the microchannel. b) Picture of the setup under the microscope. 63

Figure 4.5: A sinusoidal voltage is applied using six simultaneous frequencies (ranging from 100 kHz to 27 MHz) to the central microelectrode ('2' in the cartoon). The current outputs from the outer microelectrodes ('1', '3') are converted to voltage by transimpedance amplifiers (TA) and then processed differentially by a lock-in amplifier. The zoomed-in detail reports a sketch of the sensor in the microfluidic channel. 65

Figure 4.6: Typical GUI interface used for data processing. The signal represented in the dashed gray box (blue line) is filtered to remove noise and correct the baseline. Yellow triangles highlight the changes in the baseline which are identified as peaks. The line in green indicates the threshold for the peak detection. The noise filtered out from the signal is represented in red. The buttons on the right (violet dashed box in the figure) allow the user to change the parameters used for signal processing. 66

Figure 4.7: Schematic representation of the preparation of primary T lymphocytes samples. CD8⁺ T cells were purified from the spleen of laboratory animals and split in two subsets. One cell pool was activated with anti-CD3 and anti-CD28 antibodies, stained with anti-CD8 and anti-CD69 and then FACS sorted for CD69 expression. Sorted CD69⁺ cells were split in two and one of the subset was labelled with CFDA-SE for fluorescence imaging (acquired simultaneously to the electrical measurements). 67

Figure 4.8: Sketch of the sensor in the microchannel (top view) and of the signal change due to the passage of a single particle (cell/bead). Due to the differential configuration, the amplitude peak assumes positive (a) or negative sign (b) respect the signal baseline, depending on the position of the particle in the sensor (Gap #1/Gap #2 in the figure). 69

Figure 4.9: Raw in-phase component signals recorded at six different frequencies simultaneously. Peaks correspond to the passage of a single 8 μm -diameter beads in either interelectrode gaps. 70

Figure 4.10: Typical signal output for an 8 μm bead before (a) and after (b) the signal processing procedure. (c) Histogram of the measurement noise extracted for the in-phase component at 6MHz. Noise distribution is fitted by a normal density function (dashed line in red). 71

Figure 4.11: (a) Variation of noise standard deviation of the in-phase (blue) and out-of-phase component (yellow) of the output signal respect frequency. (b) Variation of the ratio between the peak amplitudes of 8 μm -diameter beads and the corresponding noise standard deviation versus frequency. 72

Figure 4.12: Variation of CV of the peak amplitudes of 8 μm -diameter beads evaluated for both in-phase (blue) and out-of-phase (yellow) components of the output signal recorded at six different frequencies simultaneously (more than 600 events). 72

Figure 4.13: Histogram of the impedance signature of 8, 10 and 15 μm beads (668, 169 and 238 events respectively) plotted against the in-phase component recorded at 6 MHz. 73

Figure 4.14: Variation of the in-phase component at 6 MHz for the mixture beads population respect their volume. 73

- Figure 4.15: (a) FACS analysis of stimulated T lymphocytes during cell sorting. Gated CD69⁻ cells are represented in red and the gated CD69⁺ population in violet. Optical microscope images of unstimulated (b), CD69⁻ (c) and of the CD69⁺ cells (d) sorted by FACS. (Bar size 50 μ m). 74
- Figure 4.16: Changes of the in-phase and out-of-phase components generated by the passage of single unstimulated CD8⁺ T cells. The values are the measured peaks averaged over around 200 events or 1200 events depending on the frequency. The error bars correspond to the standard deviation of the measurements..... 75
- Figure 4.17: Injections of mixture of CD69⁻ (in grey, 313 events) and labelled CD69⁺ (in red, 131 events). 76
- Figure 4.18: (a) Individual injections of CD69⁻ T cells / 10 μ m beads mixtures and CD69⁺ T cells / 10 μ m beads mixtures (yellow squares and blue circles, respectively) before correction. (b) The values of each population have been adjusted on both axes by subtracting the median value of the corresponding beads' population. The overlap of the beads populations before and upon correction is highlighted in the respective insets. 77
- Figure 4.19: Scatter plot corresponding to the signal peaks of single cells at frequency of 6 MHz and 14 MHz for CD69⁺ cells (a), CD69⁺ and CD 69⁻ cells (b) and CD69⁺, CD 69⁻ and unstimulated cells (c). The peak values of CD69⁺ cells have been adjusted with respect to the beads populations. The insets highlight the overlap of the beads populations upon correction. c) The dashed line, representing the iso-contour of the Gaussian distribution, allows to visualize a 2D confidence interval, showing the 50% and 99% confidence ellipses for the bivariate normally distributed data. This confidence ellipse defines the region that contains 50% (dark green) and 99% (light green) of the data. 78
- Figure 5.1: SEM picture shows SU-8-based 3D microelectrodes fabricated on a glass substrate and integrated in SU-8 microfluidic channel..... 85
- Figure 5.2: SEM picture of multiple sensors in a single microfluidic channel. The SU-8 separator prevents cells flowing through the interelectrode gap of the two different sensors. 85
- Figure 5.3: (a) Schematic of the microfluidic device featuring integrated coplanar electrodes (in yellow). (b) Schematic of a close up view of a single trapping site combined with the sensing electrodes..... 86
- Figure 5.4: (a) Schematic top view of the trap sites. The red dashed circles indicate the position that would be occupied by a cell in the trap sites between two round-shape pillars. According to direction of the flow one trap would be occupied by a cell and the other would remain empty, working as reference. The metal connections are represented in green and are partially buried by the SU-8 microfluidic pattern represented in blue. The microchannel is represented in white. According to the design proposed by Tan et al., when the trap is empty the flow resistance in the short channel is lower than that one in the loop channel. Therefore, a cell in the microchannel is carried into the trap if it is empty, while it is carried in the loop channel if the trap is filled. (b) SEM image of four round-shape pillars. The green circles indicate the top edge of the metal-coated SU-8 micropillars. (c) SEM image of the four round-shape pillars incorporated into the SU-8 microfluidic pattern. The green circles indicate the top edge of the metal-coated SU-8 micropillars. 87

LIST OF TABLES

Table 1.1: Ideal circuit elements most commonly used in IS models	8
Table 3.1: Values of the electrical parameters for two micropillar electrodes in a microfluidic channel extracted by fitting of the equivalent circuit in Figure 3.8 b.....	48
Table 3.2: Values of the electrical parameters for two micropillar electrodes without (indicated as ‘-SU-8’) and with SU-8 extensions (indicated as ‘+SU-8’) extracted by fitting the equivalent circuit in Figure 3.8 b	52
Table 4.1: Values of CV of 8 μm , 10 μm and 15 μm diameter beads measured by the sensor and provided by the manufacturer.....	74

LIST OF EQUATIONS

Equation 1.1.....	6
Equations 1.2.....	6
Equation 1.3.....	7
Equation 1.4.....	7
Equation 1.5.....	10
Equation 1.6.....	10
Equation 4.1.....	64

INTRODUCTION

Microfluidics is a technology that permits the analysis of the sample by exploiting the behavior of minute volumes of liquid in microscale fluidic channels. Microfluidics systems gained an enormous success in life science and biomedical research since the reduction of scale they entail allows to attain several improvements compared to macroscopic systems. In first instance, microfluidics allows to save samples and reagents and permits a precise control of liquids (i.e. characterized by laminar flow, diffusion mixing and rapid energy dissipation [1]). The small volumes employed in microfluidics shorten reaction times and the intrinsic design versatility of microfluidic configurations enables high-throughput and parallel analysis. The size of devices itself is also reduced making microfluidic platforms portable and low-power, hence ideal to develop point-of-care (POC) devices. A new class of POC systems based on microfluidics have begun to emerge in the market [2]. Commercial glucometers are commonly considered the archetype of a successful microfluidic product [3]. A glucometer takes a small drop of blood from a finger prick, transfers it by capillarity to an analyzing region where blood glucose is measured by a combination of enzymatic and electrochemical reactions.

A diverse array of technological developments as led to the establishment of an integrated implementation of microfluidics, denominated (LOC) technology. LOC platforms are miniaturized devices for integrated biological and chemical analysis [4]. These devices are developed using microtechnology techniques based (in an early phase) on silicon and using well-defined processes that have been derived from the microelectronics industry. Later in time also glass and quartz, whose transparent properties are convenient for optical inspection have also been employed together with polymers [5]. LOC systems rely on microfluidics to scale down and integrate multiple laboratory processes on the same device. In this way laboratory procedures can be automatized and accelerated. In addition, the possibility to process small volume of sample avoids the need for labor-intensive laboratory manipulation also reducing the risk of potential procedural errors.

The first examples of LOC devices were employed for molecular analysis of amino acids [6] and in particular for sequencing DNA [7]. Successively their application

was extended to the analysis and the manipulation of more complex systems, such as living cells [8]. Cell size is commensurate with the size of microfluidic channels and this allows an accurate control of the sample and of the environment, granting high sensitivity and repeatability of the analysis. All the procedures used in cell biology can be performed on microfluidic platforms. Namely cell culture [9], selection [10], cell treatment, interrogation and biochemical analysis [11].

Microfluidic cell assays can be performed using tissue or populations of cells or, alternatively, addressing cells at single level. Single-cell analysis offers the important advantage of avoiding information loss since some rare features of a diverse pool of cells can be masked when averaging the heterogeneity of cells populations. Yet importantly, microfluidic technology grants the possibility to process large quantity of single cells ensuring high throughput analysis [12].

Single cells interrogation through LOC platforms typically relies on label-dependent methods, such as fluorescence-based techniques. Despite their high informative content, these can be rather invasive and result in loss or damage of the sample [13]. In addition, their employment introduces an alteration of the sample, therefore affecting the possibility to re-employ cells. Label-free approaches harness intrinsic properties of cells, such as size and mechanical or electrical features, to characterize them less invasively reducing sample alteration. The detection of changes in mass or in electrical properties represents indeed an important alternative to fluorescent and luminescent detection [11].

The use of microfluidic systems embracing single-cell approach and label-free techniques is of great interest in the context of adoptive immunotherapy, where the processing and characterization of immune cells to reemploy therapeutically should characterize at high resolution the heterogeneity of the sample and avoid critical modifications of cells samples.

Objectives and Organization of the Thesis

The objective of the work reported in this thesis was to design and develop a label-free microflow cytometer for electrical impedance measurements. The main goal is to propose a microfabrication technology allowing to realize 3D microelectrodes either free-standing or integrated in channel sidewalls. Two different approaches are presented, each offering peculiar advantages but both notable for their high design flexibility and versatility. The successive objective is to demonstrate the functionality of the 3D microelectrodes as a non-invasive platform for the analysis for the detection of activated T lymphocytes in flow.

This thesis is divided in five chapters organized as follows.

Chapter 1 introduces the impedance spectroscopy as a method for the characterization of materials and their interface. It presents the basic definitions and the fundamentals of impedance-based approaches, as well as the current state of art of impedance-based chip solutions for cell analysis.

Chapter 2 and Chapter 3 present, respectively, two different fabrication processes for the generation of arrays of micropillar electrodes. The ones described in Chapter 2 are based on the conformal coating of 3D SU-8 structures with metal layers. This approach allows to define vertical electrodes in microfluidic channels having high aspect ratio and uniform coating of the vertical sidewalls. In Chapter 3, the fabrication of microelectrodes consisting of metal-coated pillars etched into silicon and decoupled from the substrate by means of a passivation layer is described.

Chapter 4 provides, at first, a brief introduction on the biology of T cells and adoptive immunotherapy and includes a review of the current techniques to attain the label-free detection of activated T cells on microfluidic chip. In addition, we present the employment of silicon-based 3D microelectrodes for in-flow label-free and single-cell detection of in vitro activated T lymphocytes. The results obtained from the electrical measurements of primary CD8⁺ lymphocytes activated through mitogenic stimulation support the possibility of using impedance to assess single T cell activation in label-free to characterize cells to employ in personalized immunotherapy.

Finally, Chapter 5 presents the summary of this research work and provides an outlook of the future work for the continuation of the project.

1 | IMPEDANCE-BASED CELL ANALYTICS ON A CHIP

Impedance spectroscopy (IS) is a monitoring method for characterizing the electrical properties of materials and their interfaces [14]. IS has been widely studied and has become an established technology used in various applications in the biomedical field. As a non-invasive and label-free technique, IS is suitable for studying living biological cells and providing quantitative information about their dielectric properties.

This chapter presents basic definitions and knowledge of impedance theory and the current state of art of impedance-based chip solutions for cell analytics.

1.1 Fundamentals of Electrical Impedance Spectroscopy (EIS): theory and methods

1.1.1 Fundamentals of EIS

Impedance spectroscopy (IS) involves applying an AC electric signal of small amplitude, a known voltage or current signal, between two electrodes and evaluating the response over a wide range of frequencies.

A sinusoidal voltage of small amplitude, $v(t) = V_m \sin(\omega t)$, applied to a linear system, generates a current of identical frequency: $i(t) = I_m \sin(\omega t + \theta)$. The radial frequency ω is related to the applied AC frequency f (in Hz) as: $\omega = 2\pi f$ (rad·s⁻¹), where θ is the phase shift between the voltage v and the current i ; it is zero for a pure resistive impedance, and f is the frequency of stimulation.

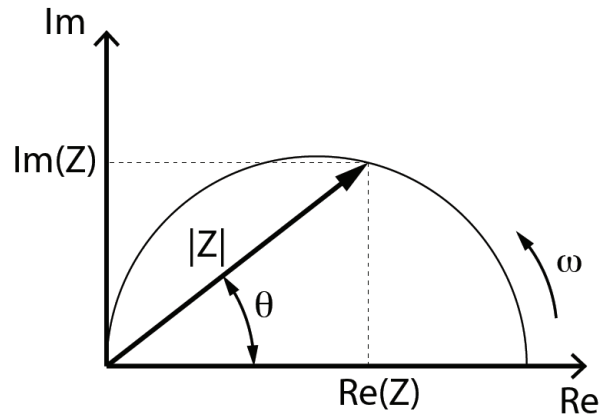


Figure 1.1: Graphical representation of impedance on complex-plane plot

Analogous to Ohm's law extended to the AC electric field, the complex impedance of the system is calculated as the ratio between the voltage and the current; it is expressed as:

$$Z(j\omega) = \frac{V(j\omega)}{I(j\omega)}$$

Equation 1.1

where $j = \sqrt{-1}$. As a complex number, it can be plotted in a planar vector and identified with both rectangular coordinates, as a combination of real (in-phase) Z_{Re} and imaginary (out-of-phase) Z_{Im} (Figure 1.1):

$$Z = Z_{Re} + jZ_{Im}$$

where:

$$Z_{Re} = Re(Z) = |Z| \cos(\theta)$$

and

$$Z_{Im} = Im(Z) = |Z| \sin(\theta)$$

Equations 1.2

and polar coordinates, as a combination of modulus ($|Z|$) and phase(θ):

$$Z = |Z|e^{j\theta}$$

where:

$$|Z| = \sqrt{Z_{Re}^2 + Z_{Im}^2}$$

and

$$\theta = \tan^{-1}\left(\frac{Z_{Im}}{Z_{Re}}\right)$$

Equation 1.3

The real part of the impedance demonstrates the ability of a circuit to resist the current flow, while the imaginary part reflects the circuit's ability to store electrical energy.

In the simplest case, for two parallel plate electrodes of cross-sectional area A and distance d , separated by the material to study (as shown in Figure 1.2) these properties are given by:

$$R = \rho \frac{d}{A} \quad \text{and} \quad C = \epsilon_0 \epsilon_r \frac{A}{d}$$

Equation 1.4

and the real and imaginary components are expressed as:

$$Z_{Re} = R \quad \text{and} \quad Z_{Im} = -\frac{1}{\omega C}$$

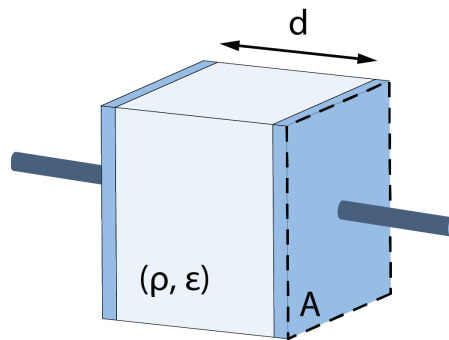


Figure 1.2: Simplified model of parallel plate electrodes separated by a material to study.

Table 1.1: Ideal circuit elements most commonly used in IS models

Component	Equivalent element	Impedance
Resistor	R (Ω)	R
Capacitor	C (F, or $\Omega^{-1}\text{s}$)	$1/j\omega C$
Inductor	L (H, or ($\Omega \text{ s}$))	$j\omega L$
Constant Phase Element	Q ($\text{Fs}^{\alpha-1}$)	$\frac{1}{Q(j\omega)^\alpha}$

ρ ($\Omega\cdot\text{cm}$) and ε_r are the electrical resistivity and the relative permittivity of the material, respectively, and ε_0 is the vacuum permittivity ($8.85\cdot 10^{-14}$ F/cm).

1.1.2 Equivalent circuit of the impedance of an object

In the framework of impedance spectroscopy, data are analyzed by means of a mathematical model based on an equivalent electrical circuit whose equivalent impedance fits the experimental data over frequency [14]. There are several possible approaches for fitting the impedance spectra, but the most widely used is the *Complex nonlinear least squares* fitting method, which is available in shared software versions (such as LEVM) or commercial software packages (for example, ZView, ZSimpWin) [15].

Circuit elements of the electrical model include standard ideal electrical elements such as resistors, capacitors, and inductors. Equivalent circuits should be chosen on the basis of the knowledge of the physical nature and physical phenomena of the system. They are then fit with the experimental data in an attempt to represent the electrical behavior of an object through electrical lumped elements.

However, the ideal circuit elements are not always adequate to describe the impedance response of a system. For this reason, distributed circuit elements, such as the constant phase element (CPE), and the Warburg diffusion impedance, have been introduced, in addition to the ideal ones[16]. These make it possible to represent the non-ideal nature of the equivalent electric circuit models. In the context of IS-based biosensors, Warburg resistance is considered only in faradaic IS. These sensors can be distinguished in faradaic and non-faradaic IS. Specifically, faradaic process includes the transfer of charges across the electrode interface. The transfer of an electron to and from the electrode alternatively oxidizes and reduces a redox species. Therefore, in order to avoid depletion of the metal electrode, the faradic IS requires a redox-active species and a DC bias [17]. On the contrary, non-faradaic IS – the focus of the present thesis – do not require additional species and bias signals. The most commonly used ideal and non-ideal circuits elements are listed in Table 1.1.

In the next section we consider the circuit elements used to fit impedance results described in this thesis.

Constant Phase Element (CPE) and Bulk resistance (R_{sol})

An electrode in contact with a surrounding electrolyte solution forms a specific interfacial region called an electrochemical double layer (EDL). The EDL is a consequence of the distribution of ions and of charged species across the electrode–electrolyte interface [18]. Figure 1.3 provides a simplified model of the double layer at the electrode surfaces. For positively charged electrode, a monolayer of specifically adsorbed ions forms on the electrode interface. The position of the electrical centers of these ions is called the *inner Helmholtz plane* (IHP). The second layer, the *outer Helmholtz plane* (OHP), is formed by non-specifically adsorbed ions that move in the solution and interact only through purely electrostatic forces. The IHP and the OHP form the Stern layer. From the OHP, the diffuse layer extends to the bulk solution [19]. The thickness of the double layer can be defined as the distance of the electrode surface from the external boundary of the diffuse layer, where the potential (ψ) becomes equal to the potential of the bulk solution. The potential drop across the EDL establishes the double layer capacitance, C_{DL} . The C_{DL} can be considered to arise from the contribution of the capacitances of the Stern layer (C_{Stern})

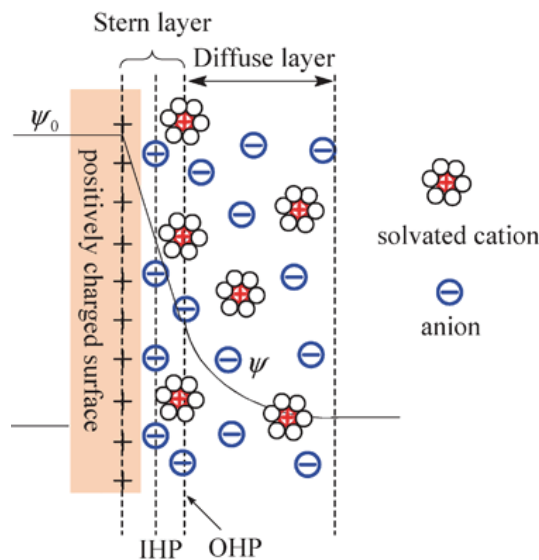


Figure 1.3: Schematic representation of Stern model of electrical double layer at metal-electrolyte interface. The inner Helmholtz plane (IHP) and outer Helmholtz plane (OHP) are shown with the Stern and diffuse layers. The IHP refers to the distance of specifically adsorbed ions on the electrode surface. The OHP refers to the distance of the solvate ions, non-specifically adsorbed. The separation between the different charges results in a potential drop across the Helmholtz planes establishing a double layer capacitor. Adapted from [19].

and the diffuse layer ($C_{Diffuse}$) and is expressed as:

$$\frac{1}{C_{DL}} = \frac{1}{C_{Stern}} + \frac{1}{C_{Diffuse}}$$

Equation 1.5

The C_{Stern} is usually considered a constant ($\sim 1-60 \mu\text{F}/\text{cm}^2$) for different solutions, while the $C_{Diffuse}$ is dependent on electrochemical potential and concentration of electrolytes. $C_{Diffuse}$ increases for higher applied voltage and higher concentrations of charged species [16].

The inhomogeneity, the roughness, the edge orientation, the porosity, the thickness, and the conductivity variability of the electrode surface are often causes of non-idealities and can lead to frequency-dependent effects. For this reason, the double layer capacitance is far from an ideal capacitor and serves as a CPE. The impedance of CPE is expressed as:

$$Z_{CPE} = \frac{1}{Q(j\omega)^\alpha}$$

Equation 1.6

Where $j = \sqrt{-1}$ and α is a constant that can assume values between 0 and 1. Q is expressed in $(\Omega^{-1}\cdot\text{s}^\alpha)$ and represents the interfacial charging by surface and electro-active species [16]. For $\alpha=0$, Z_{CPE} describes an impedance response of a pure resistor ($Q=1/R$); for $\alpha=1$, Z_{CPE} describes an impedance response of a pure capacitor ($Q=C$).

The EDL typically dominates the impedance response at low frequency. This effect can be reduced by increasing the value of the Q . For this purpose – that is, for what concerns the application of IS-based biosensors – mathematical corrections and special electrode fabrication methods, such as platinum black or porous film, have been proposed in order to increase the effective area of electrodes and thus reduce the impedance of the CPE [20]. A layer of platinum black can be electrodeposited on the electrodes upon their fabrication [21]. This treatment has been shown to reduce the electrode impedance by a factor greater than 100 [22].

The bulk solution is represented by specific parameters in the model, distinguished from the interface parameters. In aqueous systems, the conductance of ions in the bulk is typically modeled as a simple resistor that represents the resistance of the

solution (R_{SOL}), defined as in Equation 1.4-1.

In a first approximation, the most common model, which is used to fit the impedance response of non-faradaic IS biosensor, includes both a CPE and a R_{SOL} in series as shown in Figure 1.4.

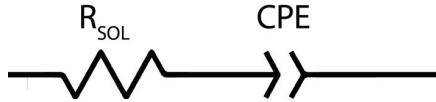


Figure 1.4: Equivalent circuit model for a non-faradaic IS biosensor.

1.1.3 Equivalent electric model of a single cell in suspension

A biological cell is a heterogeneous system composed of a plasma membrane surrounding the internal cytoplasm (see Figure 1.5a). The plasma membrane consists of a lipid bilayer containing proteins. Due to its ionic permeability it can be considered as an insulating thin shell [23]. On the other hand, the cytoplasm is assumed to be a homogeneous phase and it can be modeled as a conductive sphere. This model, known as “single-shell” model, is derived by Maxwell’s mixture theory [24] and is the simplest model for describing the dielectric properties of single cells in suspension. In order to simplify the analysis of the system, an equivalent electrical circuit can be used to represent a cell in suspension, as shown in Figure 1.6a. The resistance of the electrolyte (R_{sol}) is in parallel with the series of the capacitance of the plasma membrane (C_{mem}) and the resistance of the cell cytoplasm (R_{cyl}) [25]. When a low-frequency AC electric field is applied, charges accumulate at the interface of the insulating cell membrane and the medium, causing the cells to become polarized. The membrane insulating properties make the cell appear to be an insulating sphere that decreases the conductivity of the medium. As the frequency increases, the plasma membrane polarization decreases; this effect is known as β -dispersion or dielectric relaxation [26]. The plasma membrane becomes more conductive and its short-circuiting effect generates a current inside the cell. Impedance spectroscopy in this frequency range may provide information about the electrical properties of the plasma membrane. For higher frequencies, the polarization of the plasma membrane is almost absent. Thus, the plasma membrane becomes completely transparent to the current that penetrates the cell interior, providing information about the cytoplasmic conductivity [25], [27]–[29]. The ratio between the impedance acquired at high and low frequencies is known as “opacity” [30], which can be used to normalize the data with respect to the size of the cell and its position.

Gawad et al. [31] used simulation to demonstrate that the opacity is almost unaffected by the size and the position of cells with respect to the sensing electrodes, but it carries information about cell structure.

The simplified reported model is used to interpret single-cell impedance measurements [27], [22], [32]–[34] (described in the next sections). This model is obviously an approximation and, in certain cases, such as cell electroporation and cell lysis [35], more accurate equivalent circuit models including cell membrane conductance and cytoplasmic capacitance are required (Figure 1.6b).

A multi-shell model can also be used in order to consider other phenomena of dielectric dispersions inside the cell, such as those due to organelles and membranous structures of the cytoplasm [23]. Double-shell models Figure 1.5b have been applied to study lymphocytes [27], and yeast cells [36], also including vesicles for studying bacteria [37].

1.2 Cell characterization based on electrical measurements

In the 1910s, Höber detected the presence of the cell membrane by means of impedance-based techniques [38]. Later on, Fricke [39]–[41] and Cole [42], [43] investigated different cellular systems in suspension. Cole used Maxwell's equations to derive the complex impedance of a single-shelled cell in suspension [44], [45] In

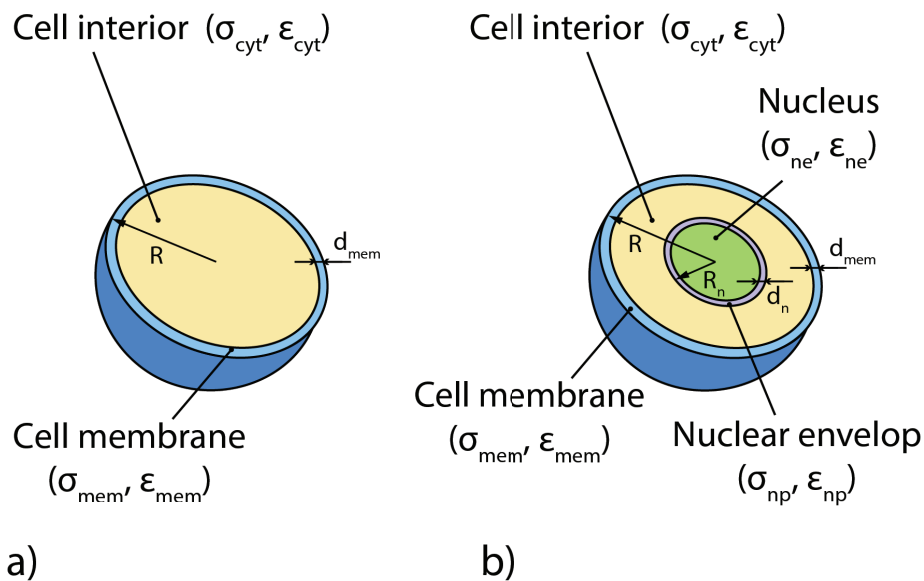


Figure 1.5: Modelling of a cell by means of: (a) a single-shell model, including cell membrane and cytoplasm and (b) a double-shell model including cell membrane, cell cytoplasm and nucleus.

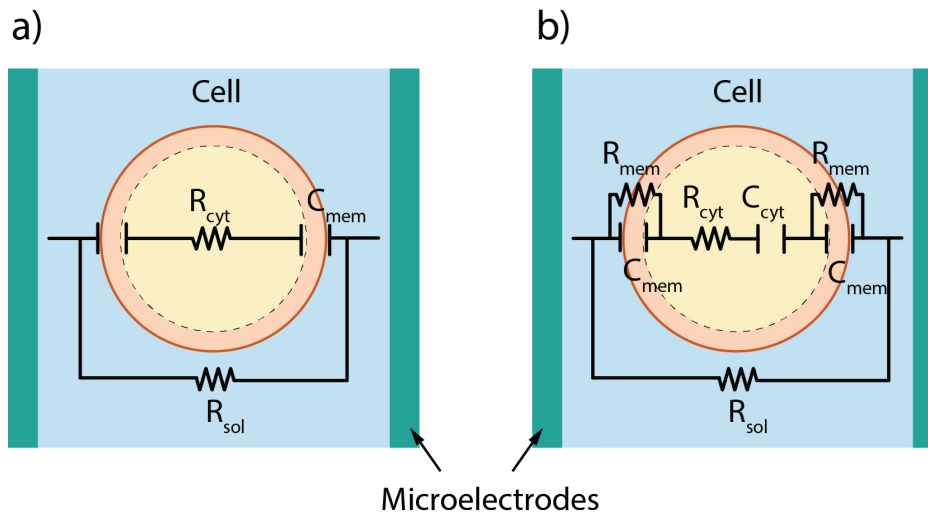


Figure 1.6: Electrical model for a single cell suspended in a sensing region defined by the microelectrodes

1937, Cole and Curtis performed, for the first time, a measurement of a single *Nitella* cell, using two electrodes embedded in a groove in which the cell was placed. Schwan [26] later identified the three major dielectric dispersions for a biological cell in suspension.

Since then, extensive research has been carried out thanks to the advancement of the technology. The development of new and more sophisticated electrical monitoring systems based on microfabrication has allowed for high-throughput processing and reduced sample consumption. Thanks to microfabrication methods, electrodes can be miniaturized and integrated in microfluidic devices with faster and more accurate analysis and more efficient solutions for the investigation and the manipulation of the sample.

Cell samples can be investigated either in culture – obtaining information about the overall population – or at the single-cell level, in order to overcome the cellular heterogeneity. In the first case, cells are grown on electrodes; in the second case, cells typically flow in microchannels or are immobilized by a single trap in the sensing region. Both methods offer different kinds of information and different instruments of analysis and are described in more detail in the following sections.

1.2.1 Cells in culture

Giaever and Keese were the first to demonstrate how electrical impedance spectroscopy can be applied for monitoring cellular functions in [46]. In their study, mammalian fibroblasts were grown on small gold electrodes (2 cm^2 counter electrode (CE) and $3 \cdot 10^{-4} \text{ cm}^2$ working electrodes (WE)) evaporated on the bottom surface of a polystyrene culture dish and exposed to small AC electric fields [47], (Figure 1.7). The impedance of the system, measured over time at 4 kHz by a lock-in amplifier, was determined by the presence of the cells on top of the WE. In particular, the attachment and the spreading of cells on the electrodes surface alters the sensing area, causing an increase in the impedance of the overall system. This is a consequence of the fact that cells at low frequency behave essentially like insulating particles, because of their plasma membrane, and impede current flow between the electrodes, thereby increasing the impedance of the system. During cultivation of cells, fluctuations of the impedance response were observed. Larger cell density decreased the amplitude of the fluctuations, which were interpreted as the result of the motion of individual cells on top of the electrodes. During experiments, microscopic observation of the cell sample demonstrated that cells were not affected by the presence of the electrodes or by the electric fields.

The same authors described the idea of the measurements in greater detail in subsequent studies. They presented an interpretation and the formulation of the experimental observations and how to extract relevant parameters from the electrical signal

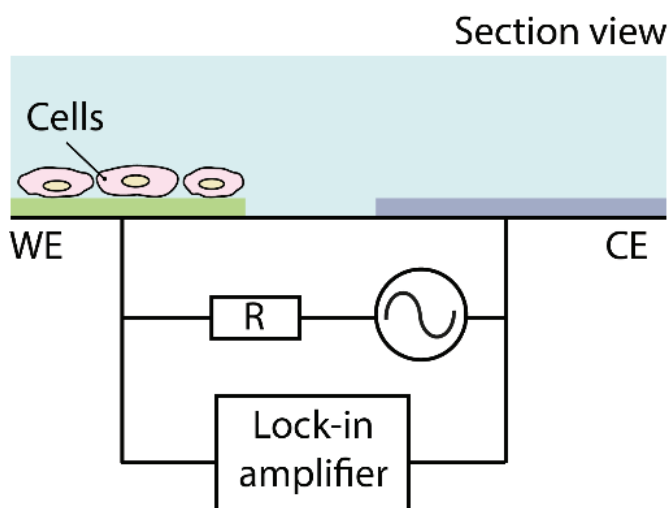


Figure 1.7: Schematic of the typical ECIS setup. A small AC signal is applied between the WE and CE. A series resistance provides a constant current that makes the voltage measured by the lock-in proportional to the impedance of the system. WE typically has a smaller surface than the CE to ensure the impedance measurement is dominated by the cell layer on the WE; otherwise, the impedance of the medium bulk would screen the contribution of the interface.

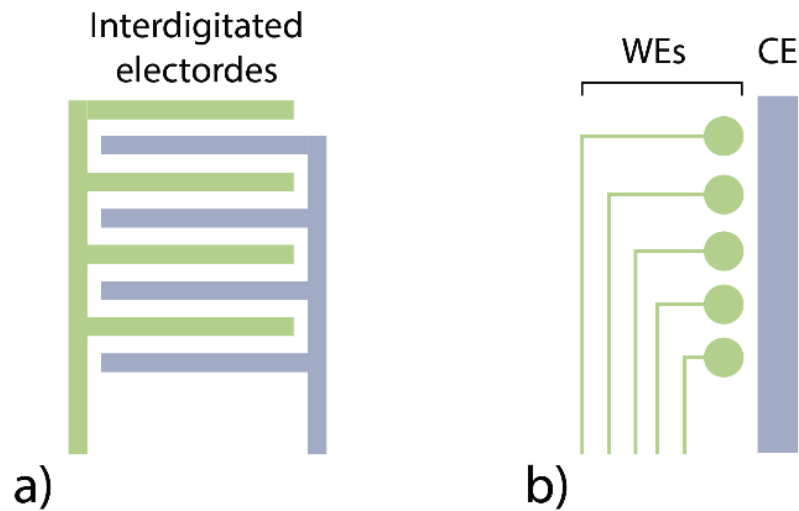


Figure 1.8: Representation of two widely employed electrode configurations for ECIS: (a) interdigitate electrodes and (b) electrode array

with its associated model [48], [49]. This measurement method became known as electrical cell-substrate impedance sensing (ECIS); Ehret et al. later employed this technique using interdigitated electrode structures (IDES) [50] (Figure 1.8a). In this case, cells are grown on symmetrical comb-shaped interdigitated electrodes on non-conductive substrate [51], [52].

Microfabrication has led to further variations of electrodes design being proposed to harness the ECIS potential as in the case of microelectrode arrays featuring multiple WEs that share the same larger CE electrode (Figure 1.8b). This configuration can be even adapted to address single-cell analysis. Indeed, WEs with an appropriate size can host single-cells revealing the heterogeneity of cells that is concealed within cell population. In [53] the authors demonstrated that impedance monitoring technique is suitable and sensitive enough to detect cellular responses at the single-cell level.

Thanks to the simplicity of ECIS enabling label-free and real-time analysis, and its compatibility with microfabrication technology, several ECIS systems have been developed as on-chip devices, for different biological applications, such as cell viability [54], [55], adhesion [56], migration [57], [58], cytotoxicity [59], [60], apoptosis [61], [62], cell-cell interactions [63] and functionality in response to biochemical stimulations [64], [65].

Moreover, commercial products that are currently on the market include the ECIS system from Applied BioPhysics, xCelligence from ACEA Biosciences-Roche, the Cellkey system from Molecular Device, and the Bionas Discovery 2500 system by Bionas. All of these systems are impedance-based label-free cellular assay platforms that record the impedance shifts related to changes in morphology, adherence, and

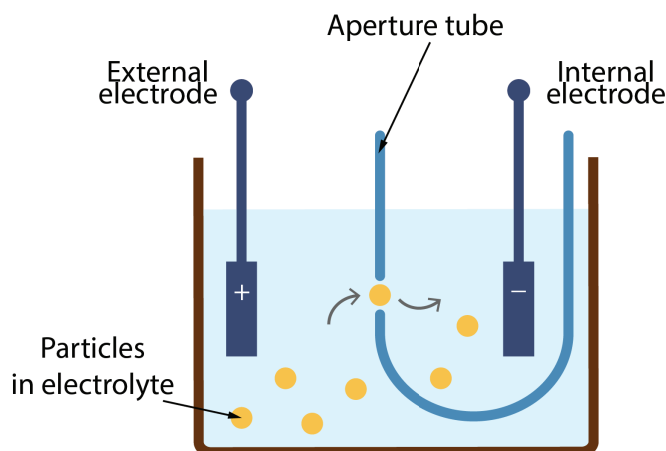


Figure 1.9: Schematic representation of Coulter principle.

cell numbers. The xCelligence system also offers the possibility to perform invasion/migration assays integrating a microporous membrane, such as those performed in a Boyden chamber [66].

1.2.2 Single-cells in suspension

In 1953, Wallace H. Coulter radically transformed the field of blood tests in clinical laboratory by presenting the first flow cytometer [67]. The so-called Coulter principle is schematically represented in Figure 1.9. It relies on measurement of the change of electrical current generated by an individual particle passing through a small aperture separating two reservoirs. Particles are suspended in an electrolyte solution and each reservoir hosts an electrode for measurements. A DC or a low-frequency voltage is applied between the pair of electrodes. The passage of a particle through the aperture causes a displacement of the conductive solution and reduces the current flowing between the electrodes. The measurement of the current provides information about the number of particles flowing through the system and about their volume. Indeed, as a particle passes through the aperture, it induces a change in current that is proportional to the amount of liquid displaced.

The Coulter counter was rapidly commercialized and became an established tool in clinical and research laboratories thanks to its simplicity and the high sensitivity [68]. Moreover, portable and automated instrumentation was recently proposed by Merck Millipore (*Scepter™ 2.0 Cell Counter*). This system employs the Coulter principle in a handheld pipette-like format and is intended for research use.

In recent decades numerous miniaturized versions of Coulter counter have been

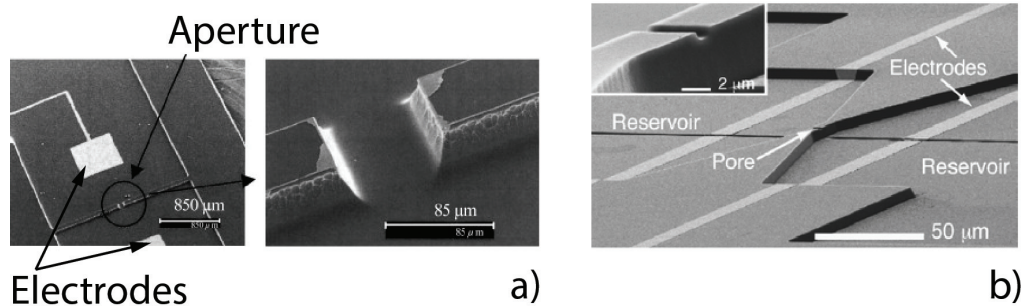


Figure 1.10: Scanning electron microscope images of micro Coulter counters from (a) Satake et al. [71] and (b) Saleh and Sohn [72]. A pair of electrodes are separated by an aperture obtained on a silicon (a) and on a glass substrate (b).

proposed by different research groups. In the 1990s, the first micro-Coulter counters were proposed by Larsen et al. [69] and Koch [70]. Other research groups then introduced further designs, all mostly based on a microfabricated aperture separating a pair of microelectrodes. Satake et al. [71] utilized a silicon substrate featuring a microchannel with an aperture and platinum microelectrodes, as shown in Figure 1.10a, to measure polystyrene beads and red blood cells. Saleh and Sohn measured smaller particles, such as colloids ranging from 190 to 640 nm [72], single DNA molecules and antibody binding into nano beads [73]. In both publications, they patterned platinum electrodes across two reservoirs connected by a pore of $5.1 \times 1.5 \times 1 \mu\text{m}^3$ (Figure 1.10b). The reservoirs and the pore were previously obtained by etching a quartz substrate. Similarly, other groups used innovative and more sophisticated technology to measure nano-scale particles, including DNA [74], [75], viruses [76], and pollen [77].

With the aim of improving the sensitivity and address the issue of channel clogging in micro-Coulter counters, Nieuwenhuis et al. presented a device with a dynamic liquid aperture [78]. This made it possible to adapt the size of the aperture to the size of the particles. The authors defined the aperture by a non-conductive sheath liquid that surrounded the conductive sample liquid on three sides (Figure 1.11a). In this way, the size of the aperture can be controlled by changing the flow-rates of the sample liquid and the sheath liquid. Figure 1.11b shows that a stable sheath flow is formed and the Coulter aperture can be varied over a large range. Since the physical dimensions of the channel remains much larger than the Coulter aperture, this method also makes it possible to prevent channel clogging. Similarly, Rodriguez-Trujillo et al. used coplanar microelectrodes in a PDMS channel with a hydrodynamic focusing to define an adjustable aperture in two dimensions [79]. The authors increased the detection speed and further characterized the device, revealing its potentiality and versatility. They analyzed 20 μm polystyrene beads as well as yeast cells of 5 μm diameter.

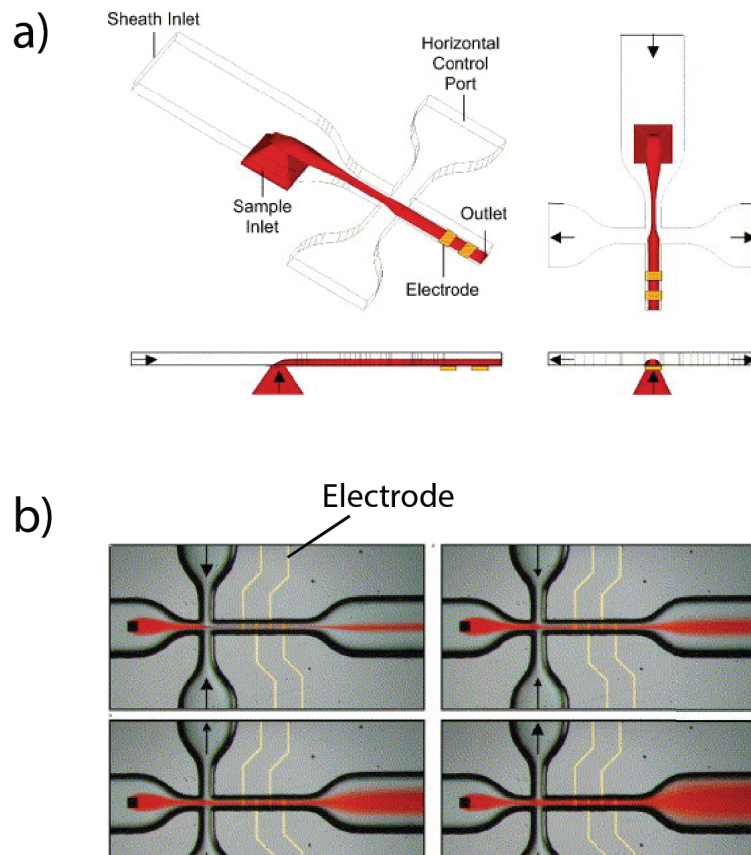


Figure 1.11.: (a) Dynamic controllable Coulter aperture ; (b) Experimental demonstration of the stable sheath flows and of the Coulter aperture achieved. [78]

The throughput of micro-Coulter counters can be improved fabricating multi-apertures, as suggested by Zhe et al. [77]. The developed device consists of a common electrode placed in a shared reservoir at the entrance of the microchannels and four central electrodes fabricated at the center of each microchannel (Figure 1.12a). The design of electrodes reduces the crosstalk between each pair of electrodes, which enables multiple channels in a single device. With the same of improving the counting efficiency, Jagtiani et al. [80], [81] proposed an alternative design fabricating a multi-aperture Coulter counter, as shown in Figure 1.12b.

As seen so far, Coulter counters are based on DC or low-frequency measurements that only provide information about the number and size of cells, thus limiting their use. The extension of the Coulter principle employing higher frequencies makes it possible to obtain information about other properties of cells, such as their membrane and internal composition [58]. Moreover, it solves the problems associated with DC sensing with microelectrodes, such as the significant loss of metal electrodes due to redox reactions at the electrode interfaces. An example is the work proposed by Zheng et al., who measured human blood cells at 10 kHz comparing the performance of the device to a conventional counter [21]. Mernier et al. used

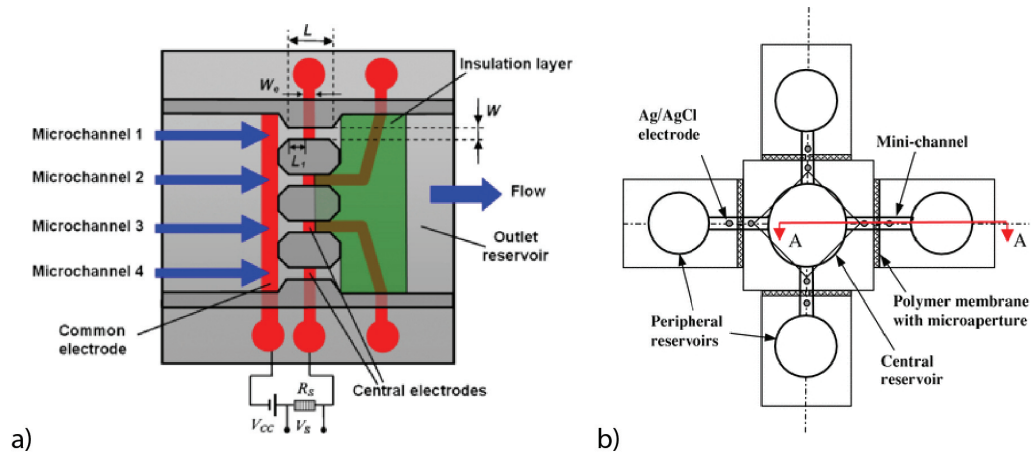


Figure 1.12: (a) [77] Schematic top view of four-channel device based on Coulter counting principle. The device has a common electrode at the entrance of the microchannel and four central electrodes fabricated at the centre of each microchannel; (b) [80] Schematic top view of a multi-aperture Coulter counter for micro particle detection. A polymer membrane with a single microaperture separates each peripheral reservoir and central reservoir.

AC signals in order to count and differentiate living and dead yeast cells. They integrated the electrodes arranged in a Coulter counter configuration with a lysis region (based on AC electric field effect) [82] and, in another study, with a sorting region (based on dielectrophoretic separation) [83].

Microcytometry based on AC signals attracted a great deal of interest and led to the evolution of the micro-Coulter devices in impedance-based microcytometers; these are described in more detail in the next section.

1.3 Impedance microfluidic cytometry

1.3.1 Microelectrodes configurations

Impedance-based microfluidic cytometry can be considered as an evolution of the Coulter microcounter. In this case, AC fields are applied at multiple frequencies to study particles and determine their dielectric properties. The design of the electrodes plays an important role in this technique as well as in others such as dielectrophoresis and electro-manipulation. The simplest electrode configuration typically consists of planar electrodes that are deposited on the bottom of microfluidic channels (see Figure 1.13).

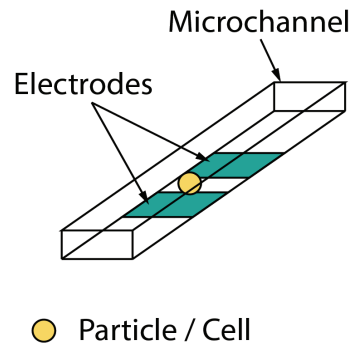


Figure 1.13: Sketch of coplanar microelectrodes configuration

Gawad et al. was the first to propose a coplanar microelectrodes design [22] which was later adapted by other research groups [79], [84]–[87]. The device featured three platinum electrodes patterned at the bottom of the channel. A two-frequency impedance signal was acquired differentially from the external electrodes (named A and C in Figure 1.14a) by applying the stimulation voltage at the central one. The

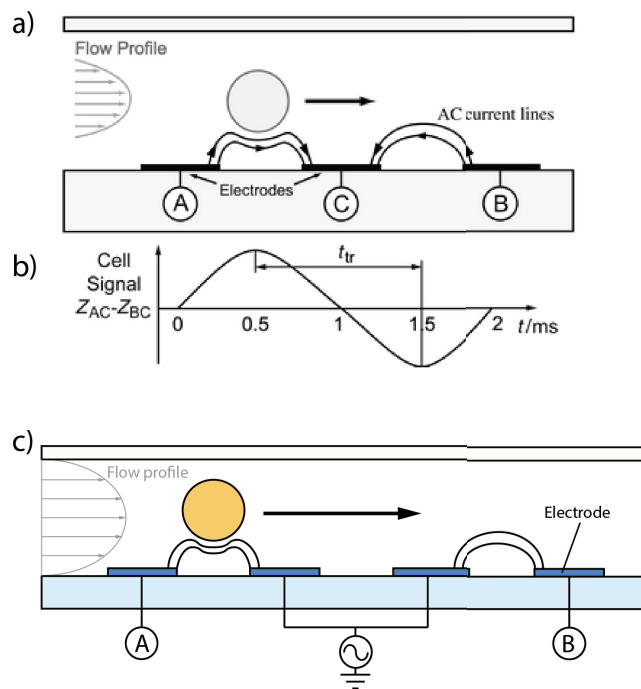


Figure 1.14: (a) Side view of a particle passing over coplanar electrodes in a microfluidic channel, b) Impedance signal over time. As the impedance is measured differentially the passage of the particle produces both a positive and a negative peak. The time separating the two peaks and the distance between the two electrodes allow to evaluate the speed of the particle in the sensing region. (a) and b) adapted by [22]).

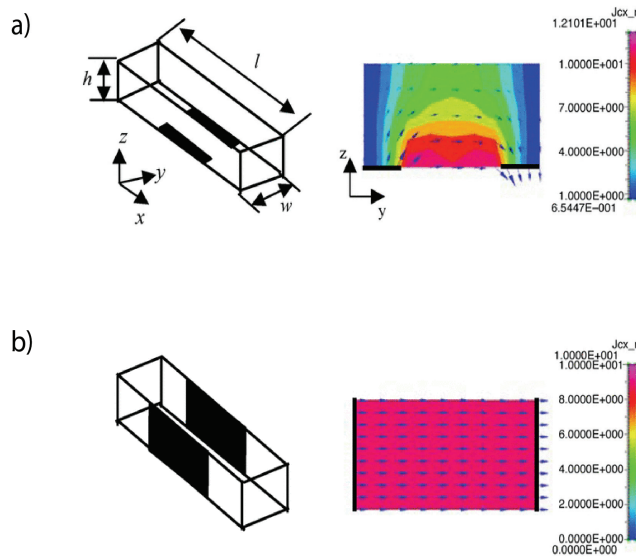


Figure 1.15: Schematic view and cross-section views of electrical field distribution for two different electrodes configuration: (a) coplanar and (b) facing electrodes. Adapted by [95].

authors successfully characterized and differentiated 5 and 8 μm latex beads, erythrocytes, and erythrocytes ghost cells (that is, dead cells where the outline remains visible). Differential measurement makes it possible to increase the dynamic range and reject the common-mode signals [88]. In this electrode configuration, cells passed consecutively through the two segments of the channel, allowing the determination of the speed of the particle (Figure 1.14b). Similarly, Benazzi et al. [89] applied the same electrode design, but used four electrodes on the bottom of the channel instead of three, as shown in Figure 1.14c. Various coplanar electrodes designs have been used for the discrimination of cell disease state, such as the detection of cells infected by parasites, as in the case of the detection of *Babesia bovis* [90] and *Plasmodium falciparum* [91].

Despite the simplicity of fabrication, coplanar design leads to a non-homogeneous electric field distribution on the channel height. Hence, particles flowing in the channel at different heights experience different electric field and, consequently, different impedance signals. The need for positioning particles in the sensing volume is addressed by particle focusing techniques that inevitably make the system more complex [79], [84], [92]. This necessitates technological solutions that make it possible to apply electrical signals homogeneously across the full channel height. Better results can be achieved by placing the electrodes so that they face each other. Such an arrangement means that the induced field lines exhibit better linearity in between the electrodes, which makes it possible to achieve improved field homogeneity throughout the channel. Sun et al. used numerical simulation of the electric field distribution verifying analytical expressions to demonstrate that, for the same geometrical features, parallel facing electrodes configuration is more sensitive than

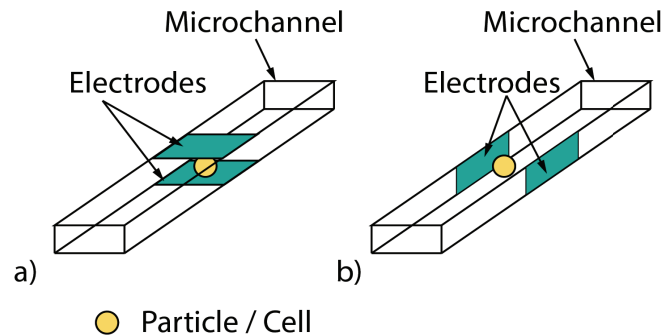


Figure 1.16 Sketch of the possible configurations of facing electrodes in a microfluidic channel: (a) planar facing electrodes, and (b) vertical facing electrodes.

the coplanar electrode one [93]. This result was also demonstrated by Bürgel et al. [94] who showed a lower sensitivity and precision with coplanar electrodes configuration. Figure 1.15 shows the electrical field distribution for coplanar and facing electrodes simulated by Wang et al. [95]. The authors showed that the electrical field concentrates at the bottom of the channel, where it is approximately three times higher than in the top part (Figure 1.15a). Unlike when facing microelectrodes, the electric field distributes uniformly along the height of the channel (Figure 1.15b).

In order to attain a uniform electric field distribution, electrodes can either be placed at the top and bottom of a chamber (Figure 1.16a), or they can be fabricated parallel to the channel's sidewalls (Figure 1.16b). The first solution has been extensively exploited by different authors and for different applications. Differential measurements are usually preferred for planar electrodes as well. One of the first examples of planar facing electrodes for impedance employed in impedance microfluidic cytometry was presented by Cheung et al. [32]. They fabricated an impedance microcytometer featuring platinum electrodes on a float glass substrate. Figure 1.17a shows the standard measurement configuration for planar facing electrodes: a pair of electrodes is fabricated separately on the top and on the bottom of the microfluidic channel; a stimulus voltage is applied on the electrodes on a side and the current is measured differentially from the electrodes in front. Authors tested the device (shown in Figure 1.17b) measuring polystyrene beads of different sizes, red blood cells, ghost, and red blood cells fixed in glutaraldehyde at different frequencies. The authors showed that red blood cells and fixed cell could be differentiated using opacity (1.1.3). Schade-Kampmann et al. used a similar system to discriminate various types of cells and cell viability [96]. Similar systems were also used to analyzed lymphocytes [97]–[99] platelets [100], tumor cells [101] and smaller samples as yeast cells [102], [103] and bacteria [104].

In all of the above-mentioned examples using parallel facing microelectrodes configuration, the top and bottom electrodes must be fabricated separately on two substrates that must then be aligned and bonded together. Also, the packaging of such

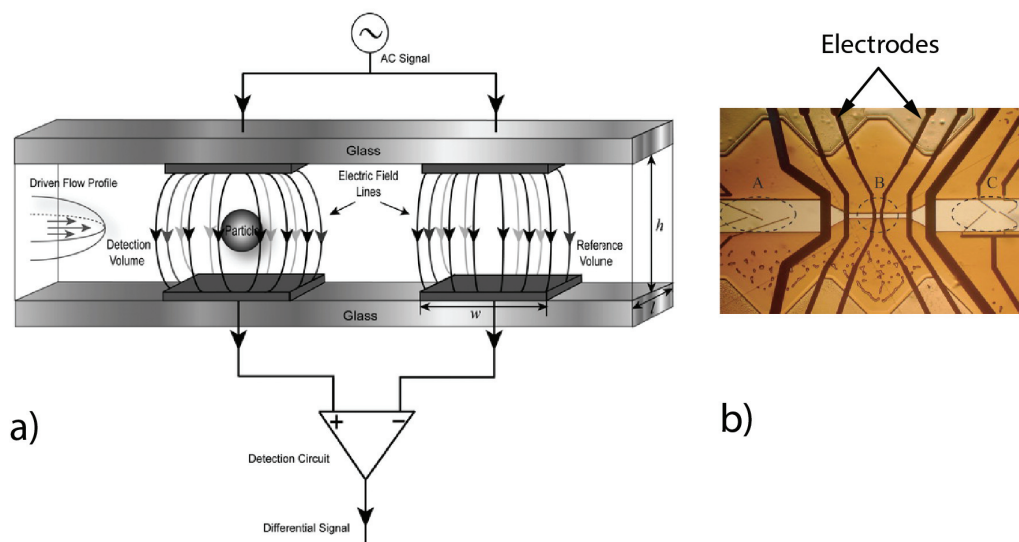


Figure 1.17: (a) Differential impedance measurement scheme used with planar facing electrodes configuration. An AC signal is applied at top electrodes. An impedance change is detected when a cell pass through the detection volume. Modified by [93]. (b) Image of the device, modified by [32].

devices is critical, since the electrical contacts of the chips face one another, making it impossible to simply use wire-bonding.

Along this line, vertical electrodes (Figure 1.16b) represent an ideal solution to increase the efficiency of lab-on-a-chip applications, especially when working with high microfluidic channels. In this case, the electrodes are placed parallel to the sidewalls and are fabricated and connected on the same substrate. These electrodes have been fabricated by such methods as etching microfluidic channels into highly doped silicon [105]. Another approach involves obtaining so-called “vertical liquid electrodes” on the channel sidewalls by electric current injections in the channel by planar electrodes in dead-end chambers placed perpendicular to the main flow [106] (Figure 1.18a). Sidewall electrodes can also be obtained by combining wet etching and metal deposition in order to develop elliptic-like channels with electrodes on their internal surfaces [107]. Furthermore, electrodes were fabricated from polymers such as PDMS that turned conductive by mixing them with metal ions [108] such as gold or silver [109], [110], with carbon black particles [111] or with single and multiwall carbon nanotubes [112].

In the two outlined solutions for realizing facing electrodes (planar facing and vertical facing configuration), the electrode distance is determined either by the channel width or height. The advantage of freestanding electrodes is that electrode gaps can be designed with more flexibility. This additional degree of freedom makes it possible to design smaller gaps, leading to higher field strength, and to arrange them in a way that reduces the electric crosstalk.

Freestanding pillar electrodes in microfluidic channels will obviously introduce additional flow resistance and lead to flow disturbances that could be critical for some

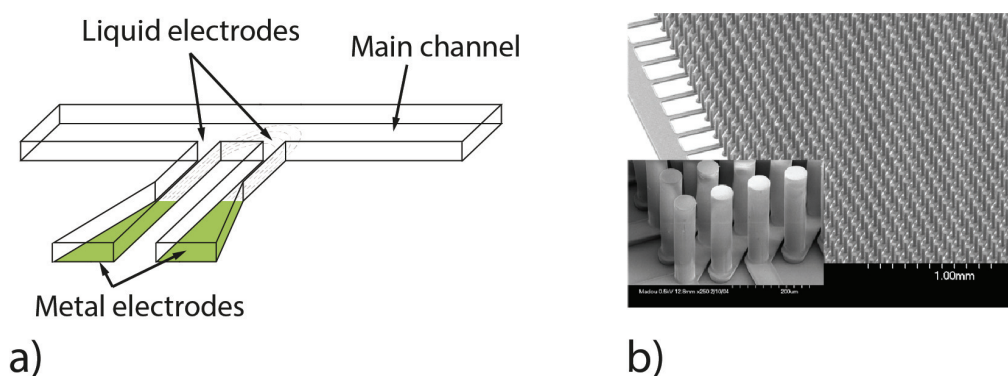


Figure 1.18: (a) 3D schematic of the liquid electrodes approach. Large metal electrodes are deposited on the bottom of the secondary channels perpendicular to the main channel. Liquid electrodes refer to the equipotential surfaces at the junctions of the lateral and the main channels. (b) SEM image of C-MEMS electrodes with underneath carbon contacts. [116]

applications. Nevertheless, freestanding pillar electrodes might also be integrated into channel sidewalls [113], if necessary, in order to avoid flow disturbances caused by the pillars.

Although freestanding pillar electrodes offer advantages for electrical-based techniques, their implementation entails specific fabrication challenges. Different processes for such structures have been proposed. Electroplating has been used to realize pillar electrodes consisting of metals [114] or conductive polymers [115]. 3D carbon structures have been realized by patterning thick photoresist that was subsequently turned into conductive carbon structures (C-MEMS) by means of pyrolysis [116] (Figure 1.18b). Freestanding carbon structures have also been fabricated by replica molding of carbon black particles into microfluidic devices [117]. 3D MEAs have been fabricated by a method that combines sputtering, laser-scribing, and electroplating [118].

All of the above-mentioned technologies have drawbacks. In the case of electroplating, process parameters must be accurately controlled in order to achieve good surface properties of the structures. Moreover, the geometry of the structures also has an influence on their surface properties, resulting in design constraints. In cases where electroplating is used in conjunction with laser-scribing, the same problems and restrictions arise regarding the additional fabrication complexity, making it a time-consuming and expensive technology. C-MEMS are a cost-effective alternative to the above-mentioned technologies, but the resulting carbon structures have a conductivity that is some orders of magnitude lower than similar metal structures. Furthermore, the shrinkage of the precursor during the pyrolysis step must be taken into consideration during the design phase and also limits the types of shapes that can be obtained. Moreover, the shrinkage observed during pyrolysis almost does not affect the bottom of the pillars where they adhere on the substrate. For this reason,

the pillars have an original diameter close to the substrate and then shrink with height, making it difficult – especially for smaller pillars – to achieve uniform gap widths over the full channel height.

With replica molding of carbon black particles, on the other hand, the resolution and design restrictions correspond to the ones related to the fabrication of the micro-mold masters. The main drawback of this technology is the high resistivity of the electrodes, which are made from a mixture of PDMS and carbon black particles.

The two following chapters present two new fabrication approaches for achieving 3D free-standing microelectrodes while overcoming the drawbacks of existing solution described above.

2 | METAL-COATED SU-8 STRUCTURES FOR 3D MICROELECTRODE ARRAYS

This chapter presents a fabrication process for arrays of high aspect-ratio micropillar electrodes. The micropillar electrodes are based on a conformal metal coating of 3D SU-8 structures, defining vertical electrodes in microfluidic channels with high aspect ratio and uniform coating of the vertical sidewalls. In order to accomplish the adhesion of the metal layers to the SU-8 micropillars, we define the most suitable formulation by investigating the role of different SU-8 post-processing steps. The development of the SU-8 structures is shown both on silicon and glass substrates. The presented strategy makes it possible to achieve a high density of singularly electrically connected structures, leveraging the additive SU-8 fabrication process. In particular, high density of connections is achieved by first patterning of the connection lines by lift-off and then defining the 3D SU-8 topography.

Standard resistive and impedance measurements show high conductivity of the structures whose fabrication process grants standard photolithographic resolution in the definition of the electrode features. The vertical electrodes are integrated into microfluidic channels, showing that it is possible to achieve electrodes that span the full height of the channel.

2.1 Fabrication of 3D electrodes integrated in microfluidic structures

As discussed in section 1.3.1 facing vertical electrodes are considered to be a key

solution in microdevice technologies, as they are able to improve the efficiency and accuracy of electrical methods by generating homogeneous electric fields along the height of microfluidic channels. Despite the acknowledged advantages of using vertical microelectrodes, current microfabrication technologies do not allow the realization of such structures with the same resolution and versatility of planar electrodes.

We propose a solution that achieves vertical high-conductive electrodes based on SU-8 photolithography, standard thin-film deposition, and patterning techniques, which enables the simultaneous integration of 3D microelectrodes and micro-channels. SU-8 is an inexpensive material that is used to fabricate structures that have high-aspect[119] and gap ratios [120] and offers good chemical resistance [119]–[121]. In addition, SU-8 enables high resolution patterning [120], [121] and it results in structures with straight and smooth sidewalls [119], [121]. Despite these advantages, SU-8 requires additional processing to obtain functional electrodes due to its insulating properties. Mixing silver nanoparticles into the SU-8 [122] or turning it into carbon structures using the above-mentioned C-MEMS process [116] have been proposed, although both approaches lead to a much lower conductivity than that of metal.

2.1.1 Fabrication of metal-coated SU-8 micropillars

A 50 μm -thick SU-8 (Gersteltec GM 1070) layer is applied by spin coating A 50 μm -

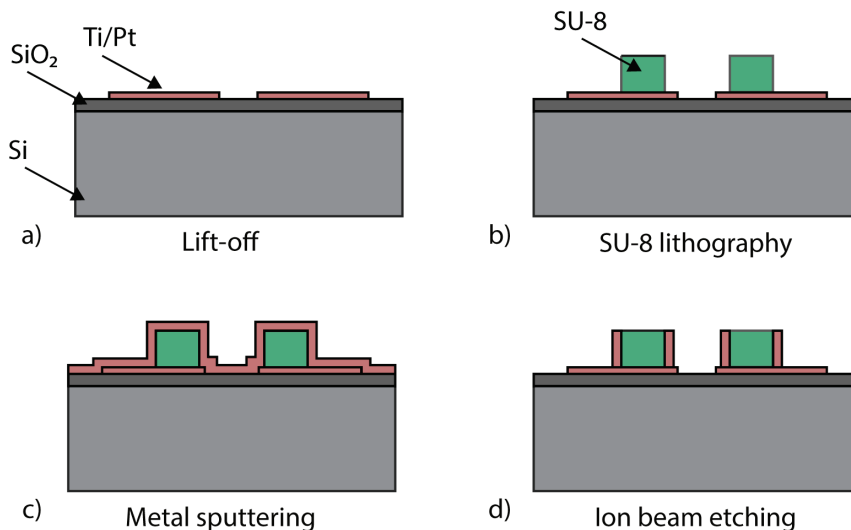


Figure 2.1: Schematic of the proposed fabrication processes for free-standing pillar electrodes. The patterning of connection lines by means of lift-off are illustrated. Planar connection lines are patterned by lift-off (a) and SU-8 pillars are patterned on top of the wires (b). The electrodes are covered with a metal film by metal sputtering (c) and the metal on horizontal surfaces is etched away by means of dry etching (d).

thick SU-8 (Gersteltec GM 1070) layer is applied by spin coating at 1600 rpm, with a soft-bake performed at 90 °C for 5 min and a UV exposure at a dose of 400 mJ/cm² (Karl Süss MJB 4). A post-exposure bake at 90 °C for 30 min is then performed to catalyze cross-linking, followed by development in propylene-glycol-monomethyl-ether-acetate (PGMEA). Finally, the SU-8 is hard-baked at 135 °C for 2 h in order to improve the adhesion of the metal layer (Figure 2.1b). The SU-8 surface is then activated by oxygen plasma (Tepla 300, 400 ml/min O₂, 500 W, 30 s) and metallized. Metallization is performed by sputter coating (Alliance Concept DP 650), resulting in the ions hitting the target with a random incident angle upon colliding with the sputtering gas (Figure 2.1c). The sputtering is performed with a distance of 80 mm between the target and the wafer, without rotation of the latter. Argon plasma pressure is $5 \cdot 10^{-3}$ mbar and DC power is 400 W for Ti and 250 W for Pt. 20 nm of Ti are deposited at an average rate of 3.1 Ås⁻¹ and 200 nm of Pt at 6.7 Ås⁻¹ (Figure 2.1c).

The adhesion of the metal to the SU-8 pillars is a critical feature of the process. We found that adhesion was more critical for bigger structures than for small ones, especially without hard-baking of the SU-8. On our test structures, adhesion was improved by both hard-baking and oxygen plasma activation prior to metal deposition. We also observed that a short oxygen plasma treatment (500 W, 30 s) was an effective compromise between achieving good adhesion and avoiding significant etching of the hard-baked SU-8 pillars.

2.1.2 Patterning of Connection Lines

In order to achieve a higher density of connection lines, these are patterned by lift-off on the plain substrate prior to the fabrication of the SU-8 structures. To this end, a double layer of lift-off and AZ1515 resist is applied by spin coating (EVG 150 automatic coater), exposed with a dose of 24 mJ/cm² (Karl Süss MA/BA 6) and developed by spray development (EVG 150 automatic coater). A triple metal layer (20 nm Ti, 200 nm Pt and 20 nm Ti) is evaporated by e-beam (Leybold Optics Lab

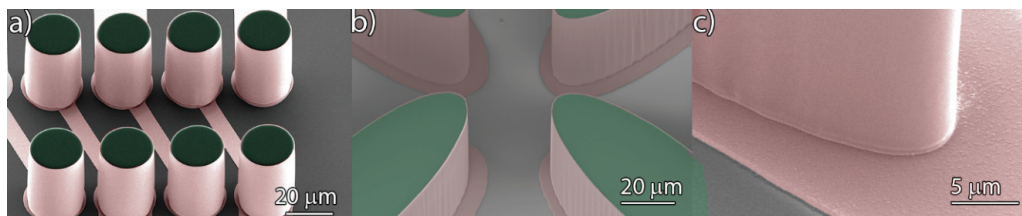


Figure 2.2 SEM imaging of metal-coated 3D SU-8 pillars (all structures are 50 μm high). Structures resulting from a process making use of lift-off for planar line patterning prior to SU-8 fabrication (a–c). Planar and vertical features combined to show the alignment outcome (b); close-up suggesting conformity of the metal layer (c).

600H), followed by dissolution of the underlying photoresist in a remover bath (Remover 1165) (Figure 2.1a1). The 3D electrodes are then obtained by patterning the SU-8 on top of the connection lines and by sputtering metal layers, as described in 2.1.1 (Figure 2.1a2 and a3). Anisotropic ion beam etching with argon ions (Veeco Nexus IBE 350) is then performed on the full wafer without any mask. This allows the second horizontal metal layer to be removed while preserving the vertical metal features. The etching process was monitored by a secondary ion mass spectrometer (SIMS) to limit the etching into the planar layer that was previously deposited for the connections (Figure 2.1a4).

Lift-off processing is used to define connection lines prior to SU-8 fabrication and metal sputtering. In this case, the most critical step is the mask-less ion-beam etching. In order to prevent excessive thinning of the previously patterned lines, SIMS is used to monitor the etching process and stop it before critically etching into the first metal layer. We developed a variety of 3D pillars with a height of 50 μm and spacing, down to 10 μm . The density of the structures depends on the resolution of the 3D structures and on the resolution of the photolithography employed to pattern the planar connections by lift-off. The aspect ratio of the pillar structures depends on the SU-8 process, which can achieve an aspect ratio of 20:1 and height beyond 200 μm .

In addition, the process allows high patterning resolution of the connection lines; we designed lines down to 5 μm in width (Figure 2.2 a). The 3D features are then aligned with photolithographic precision to the planar wires, granting high flexibility when designing the electrodes combining planar and vertical features (Figure 2.2 b). Critical aspects for this approach are the connection between planar and vertical metal structures, as well as the homogenous metal coverage of the vertical sidewalls. The uniform metal coverage of vertical surfaces is granted by the isotropy of the sputtering, as reported in [123]. We performed SEM imaging to confirm the presence of the metal layer on the sidewalls, apart from the electrical measurements reported in 2.2 (see Figure 2.2). The fabrication of the singularly addressed 3D electrodes was proved to work on both silicon and glass substrates (Figure 2.3), but other substrates could also be employed.

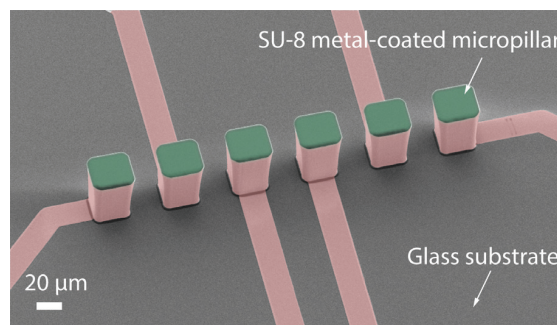


Figure 2.3: SEM imaging of SU-8 metal-coated micropillars fabricated on glass substrate.

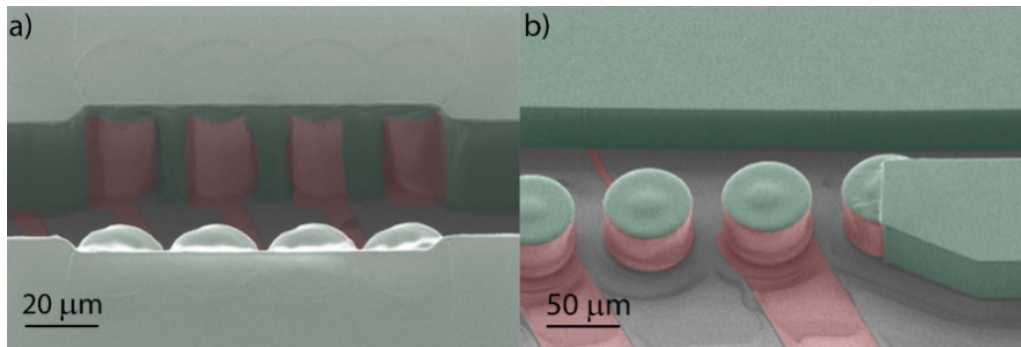


Figure 2.4 SU-8 microfluidic channels integrating 3D electrodes. SEM imaging of sidewall-integrated and free-standing electrodes spanning the entire height of the channel (a-b).

2.1.3 Integration of 3D Pillars into Microfluidic Channels

The microfluidic structures were fabricated by a second SU-8 lithography step, after the fabrication of the metal-coated 3D pillars. This made it possible to align the channels and 3D structures with photolithographic precision. SU-8 microfluidic structures are processed on the wafer after the fabrication of the 3D electrodes by the same SU-8 fabrication process used for the pillar cores, with the exclusion of the hard-baking step (2.1.1) to allow the bonding of the SU-8 to a PDMS cover for the realization of the microfluidic channel. The application of the same process parameters for the two SU-8 steps resulted in microfluidic structures with a height equal to the one of the 3D pillar electrodes (Figure 2.4 a and b). Using SU-8 for both the processing of pillars and of the channels has the advantage of avoiding the fine-tuning of the microfluidic fabrication parameters to match the height of previous 3D structures.

The realization of the microfluidic channel is obtained by bonding a PDMS cover on top of the SU-8 structures (Figure 2.5). The PDMS cover (mix ratio 10:1) is degassed in a vacuum chamber and baked for 2 h at 80 °C to catalyze crosslinking. The PDMS is bonded to the chip by oxygen plasma activation (Diener electronic Femto, 100 W, 0.6 Pa, 1 min) and silanization of PDMS. The latter is performed by placing a flask of (3-Aminopropyl) triethoxysilane (APTES) in a vacuum desiccator. The flask, together with the PDMS, are left in the chamber once the vacuum is built up for 2 h, in order to catalyze polymerization. The chip is sealed with the PDMS cover provided of punched inlet and outlet to access the microfluidic channel.

2.2 Electrical Characterization of the 3D Electrodes

2.2.1 Conductivity measurements

Electrical characterization of the 3D electrodes was performed both in air and in the presence of electrolyte solutions. The tests made it possible to verify the conductivity of the 3D electrodes, their connection to the planar metal lines, and the proper exposure of the electrode surface. The test structures were realized with the process described in section 2.1.1, which grants high resolution of the planar lines. We developed test structures to assess the resistive contribution of the pillars, that consisted of planar lines interrupted by 20 μm gaps shorted by 3D pillars (Figure 2.6a). The electrical resistance was extracted by applying a voltage sweep from -5 V to 5 V (Agilent 4155C Semiconductor Parameter Analyzer, Süss PM8 manual probe station). Moreover, vertical electrodes with lengths varying from 200 μm to 800 μm were measured (Keithley 2400) to extract the sheet resistance of the vertical metal layers (sidewalls).

The quality of the electrical connection between 3D electrodes and planar wires and the conductivity of the vertical sidewalls depends on the conformity of the metal layer deposited on the SU-8 cores. This was inspected by SEM imaging on a sample of structures and thoroughly assessed by electrical characterization. A proper connection between vertical layers and planar tracks was verified in 93 percent of the cases (192 3D electrodes fabricated on different wafers). In order to quantify the resistance of the connection between pillars and planar wires, we fabricated the test structures made out of six pillars in series and depicted in Figure 2.6a. By characterizing 96 different structures electrically, we evaluated the resistance of the single pillar to be $12.56 \pm 0.52\ \Omega$. Apart from the planar-to-vertical connection, the quality of the 3D electrodes is determined by the conductivity of vertical metal layers, which needs to ensure negligible potential drops along the electrodes height. In order to measure the sidewall's sheet resistance, we fabricated rectangular pillars of

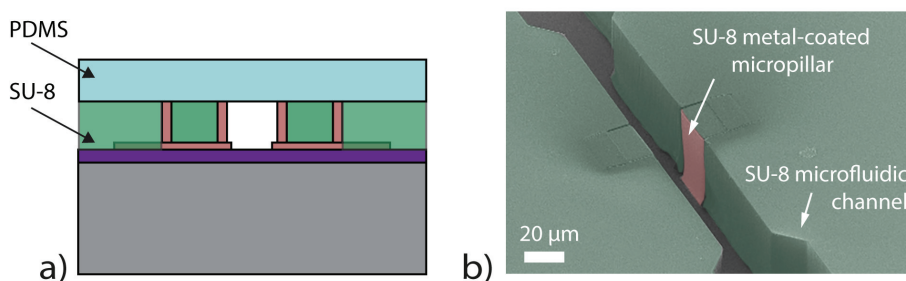


Figure 2.5: a) Schematic representation of the section view of the microfluidic channel hosting the microelectrodes. A PDMS cover obtained from an SU-8 mold is bonded on the microchannel fabricated in SU-8. b) SEM imaging of two facing SU-8 metal coated micropillars integrated into a SU-8 microfluidic channel.

different lengths, connected by planar wires at their extremity (Figure 2.6b, inset). We first determined the sheet resistance of simple planar wires (Figure 2.6b, $1.14 \Omega/\square$, square symbols) and used it to extract the sheet resistance of vertical sidewalls, (Figure 2.6b, $1.80 \Omega/\square$, for the single sidewall, diamond symbols). Therefore, the approach described is suitable for high-density arrays of 3D electrode structures and/or high channels. The electrical characterization performed on structures built on silicon and glass proves that the vertical electrodes are connected to the planar lines through low-resistive horizontal-to-vertical paths and that the resistivity of the vertical metal layers shows only a moderate increase with respect to that of planar lines.

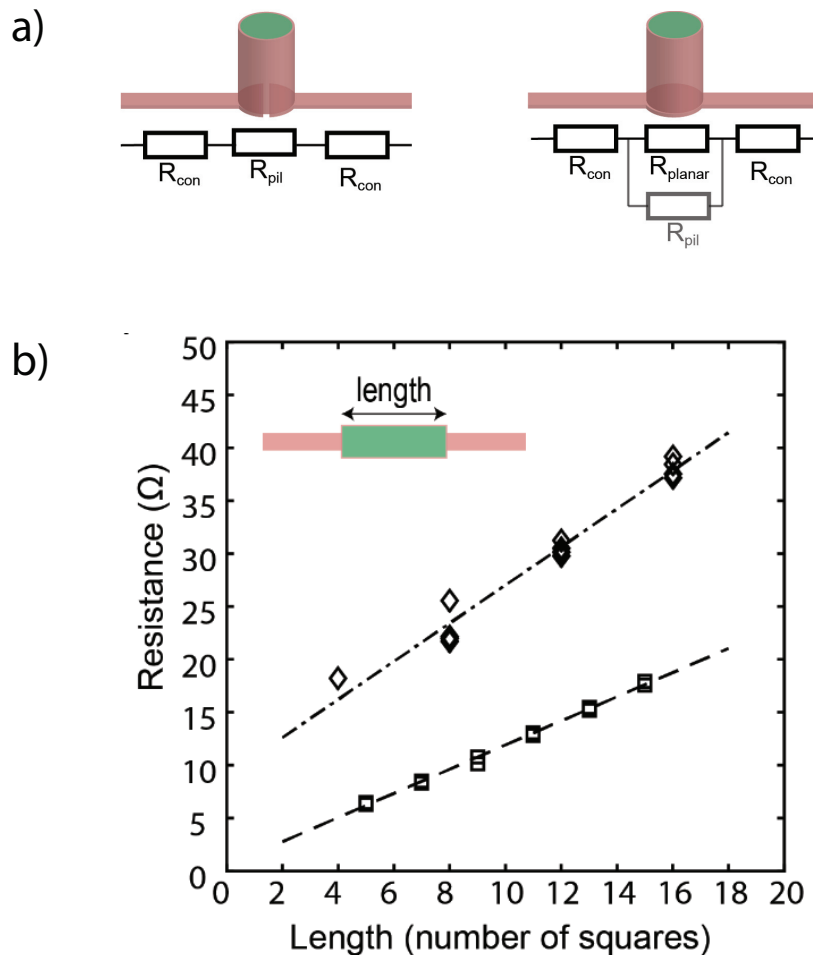


Figure 2.6: (a) Illustration of the test structures employed to quantify the resistivity of the 3D pillar (red: platinum, green: SU-8); (b) Representation of the sheet resistance of planar wires (experimental points: squares; linear fit: dashed line) and of single vertical sidewalls (experimental points: diamonds; linear fit: dashed and dotted line). Each diamond symbol corresponds to a single structure. The plot reports a total of 15 measurements on 15 different structures (diamonds), plus measurements performed on the planar wires (squares). The inset is a top-view representation of the 3D structures.

2.2.2 Impedance spectroscopy on microfluidic-integrated vertical electrodes

To verify the exposure of the 3D electrode-sidewalls, the microfluidic structures were filled with an electrolyte solution (PBS 1X), leading to the generation of a double-layer capacitance at the electrodes/solution interfaces. This parameter has been characterized by impedance spectroscopy (Zürich Instruments, HF2TA transimpedance amplifier and HF2LI Lock-in amplifier) to assess the presence of the double-layer capacitance and to observe its dependence on the exposed area of the pillar. Test structures are represented in Figure 2.7a. Pillars were embedded into the channels sidewalls, protruding $15\ \mu\text{m}$ (d'), and their length L ranged from 30 to $500\ \mu\text{m}$. We characterized electrodes spaced out either 100 or 200 μm .

We tested the exposure of vertical metal electrodes on three different microfluidic chips with $50\ \mu\text{m}$ high electrodes and channels. We injected an electrolyte solution

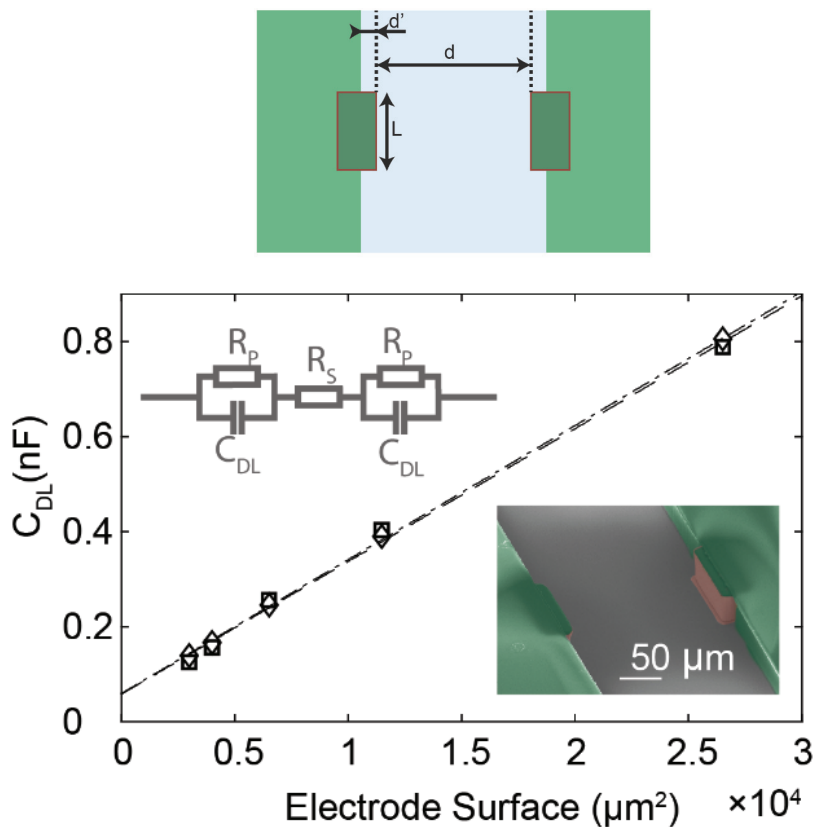


Figure 2.7: Cartoon representing the test structures to verify the exposure of vertical sidewalls to the solution (top view). SU-8 is indicated in green and coating metal layers in red. 3D pillars extrude by $d'=15\ \mu\text{m}$ from the channel main walls; (b) double layer capacitance of the single electrodes extracted by fitting the electrical equivalent model represented in the inset to a frequency spectrum acquired between 1 kHz and 10 MHz ($d = 100\ \mu\text{m}$: diamonds; $d = 200\ \mu\text{m}$: squares).

(PBS 1X) into the microfluidic channel (Figure 2.7 a) and characterized the impedance of the electrode interfaces in the frequency range from 1 kHz to 10 MHz. Ten couples of identical facing electrodes, with length L ranging from 30 μm to 500 μm , were integrated in the channel sidewalls (Figure 2.7 a and Figure 2.7 b inset). The distance between the electrodes (d) was 100 μm or 200 μm . The electrical double-layer capacitance was extracted according to the electrical equivalent model of the two electrodes represented in Figure 2.7 b. An average low-frequency capacitance value of $2.7 \pm 0.54 \mu\text{F}/\text{cm}^2$ was calculated, which indicates the presence of an electrochemical capacitor. The low standard deviation of the extracted interface capacitance suggests a homogeneous exposure. According to the results obtained by impedance spectroscopy on electrode pairs of different sizes and interelectrode spacing, we can conclude that vertical metal layers were entirely exposed.

The low resistivity of the electrodes and their connections means that this technology can be used for a wide range of electrical-based lab-on-a-chip applications. The process can be performed with any metal that can be sputtered. Some applications might have to avoid exposure of the planar wires. In this case, it is possible to passivate the horizontal surface by evaporation of insulating layers, as illustrated in section 3.2.1 [123].

2.3 Summary

We have developed a process based on SU-8 photolithography and standard thin-film deposition and patterning techniques that enables the fabrication of 3D microelectrodes integrated in microchannels. SU-8 makes it possible to achieve high aspect-ratio and high-resolution 3D electrode structures. These structures were coated with metal layers to realize vertical electrodes with low-resistivity connections to planar wires. This technology makes it possible to create 3D electrodes, either free-standing or integrated in the channel sidewall. Our work addresses various issues, including the adhesion of the metal layers to the SU-8 and individual connections of single pillars in high-density arrays. The latter is enabled by patterning the connection lines in a lift-off process prior to the fabrication of the 3D structures, avoiding metal patterning inside the high topography of the 3D electrode arrays, which would limit the density of the connections and the minimum inter-electrode distance.

Vertical electrodes make it possible to achieve uniform field strengths over the full channel height and lead to negligible electrical field gradient in the direction normal to the chip surface. Such features, combined with the possibility of singularly ad-

draining the vertical electrodes, offer significant advantages and new design possibilities in the field of electric-based techniques for lab-on-a-chip devices. Moreover, the use of higher channels and densely packed arrays of pillars has the potential to scale up throughput. The results presented have been published in [124].

3 | METAL-COATED SILICON MICROPILLARS FOR FREESTANDING 3D-ELECTRODE ARRAYS

This chapter describes an alternative fabrication process to the one presented in Chapter 2 for obtaining arrays of high-aspect-ratio micropillar electrodes. Microelectrodes consist of metal-coated pillars that are etched into silicon and decoupled from the substrate by means of a passivation layer. The width of the round and square-shaped pillars ranged from 10 μm to 70 μm , with gaps down to 10 μm and a maximum aspect ratio of 5:1. Metal deposition and patterning are revealed to be the critical steps of the process. Deposition is achieved by sputtering, while patterning is performed by photolithography, and the photoresist is applied by spray-coating. The pattern is then transferred into the metal layer by means of dry etching. This new process can be adapted to any metal that is suitable for depositing by sputtering and patterning by dry etching. In addition, the micropillar electrodes are integrated in microfluidic structures fabricated in SU-8 as shown in Chapter 2. The presence of the metal layer on the vertical sidewalls is confirmed by SEM imaging combined with EDX analysis. The arrays are then characterized by electrical conductivity measurements and impedance spectroscopy.

3.1 Introduction

Despite the good results achieved employing SU-8 for the fabrication of micropillar electrodes (see Chapter 2), we propose a different process herein based on silicon as an alternative to avoid the limits of SU-8. SU-8 is known for its poor adhesion,

particularly to metal layers, and it encounters severe adhesion problems when exposed to even mild humidity conditions [125]. Thus, the success of the fabrication is strictly dependent on the environment conditions where SU-8 is processed. Consequently, continuous readapting of parameters is required. Additionally, the high internal stress of SU-8 induces cracks in the pattern and poor adhesion to the substrate, which in some cases causes complete delamination of the layer. This aspect is critical in the presented fabrication process of microelectrodes, since even a mild loss of adhesion of SU-8 micropillars prevents the electrical connection between the metal-coated micropillar and the horizontal line.

For this reason, we propose an alternative process of obtaining micropillar electrodes that avoids the additional structural layer. In this new approach, micropillar electrodes are directly obtained by etching the silicon wafer and combining sputtering and evaporation to selectively deposit conductive and insulating layers, either on the entire wafer surface or only on the horizontal planes.

3.2 Fabrication of 3D silicon-based electrodes

3.2.1 Microfabrication process of metal-coated silicon microelectrodes

The micropillars are obtained on 4" silicon wafers. For this purpose, first a 4 μm positive tone photoresist (thinned AZ 9260) layer is applied by spin coating and exposed on a mask aligner (Karl Süss MA/BA 6) with a dose of 220 mJ/cm^2 . After the resist is developed, the pattern is transferred into the silicon using a Bosch process (Alcatel AMS 200 DSE) targeting a final etch depth of either 50 μm or 30 μm . The entire wafer is passivated by chemical vapor deposition (Centrotherm furnace) of either silicon nitride (Si_3N_4 500 nm) or silicon dioxide (SiO_2 1 μm). A platinum layer with a titanium adhesion layer (Ti/Pt 20/200 nm or 20/140 nm) is then sputtered (Pfeiffer SPIDER 600) on the wafer. For adhesion purposes of a final passivation layer, an additional layer of titanium (20 nm) is evaporated on top of the platinum (Leybold Optics LAB 600H). We chose evaporation for this specific layer formation in order to avoid depositing titanium on the vertical sidewalls of the pillars where only platinum is meant to be exposed to the solution. For the patterning of the metal layers, a diluted AZ photoresist (AZ 9260:PGMEA:MEK 4:8:90) is spray-coated in three superposed layers with successive baking steps for each layer (EVG 150). A short treatment with oxygen plasma (30 s 500 W, 400 ml/min, Tepla 300) is performed prior to spray coating. The resist is exposed with a dose of approximately 780 mJ/cm^2 on a standard mask aligner (Karl Süss MA/BA 6) and

developed by an automated development system (EVG 150). The pattern is then transferred into the metal layer by dry etching (STS Multiplex ICP). After photoresist removal, an additional cleaning with piranha solution is performed to remove resist residues.

Finally, for the purposes of electrical insulation, a 200 nm thick layer of either SiO_2 or Al_2O_3 is evaporated on the horizontal surfaces (Leybold Optics LAB 600H). Individual chips are obtained by dicing the wafer, after a protective sacrificial layer of resist is spun on top of it. Figure 3.1 schematically shows the steps of the microfabrication process.

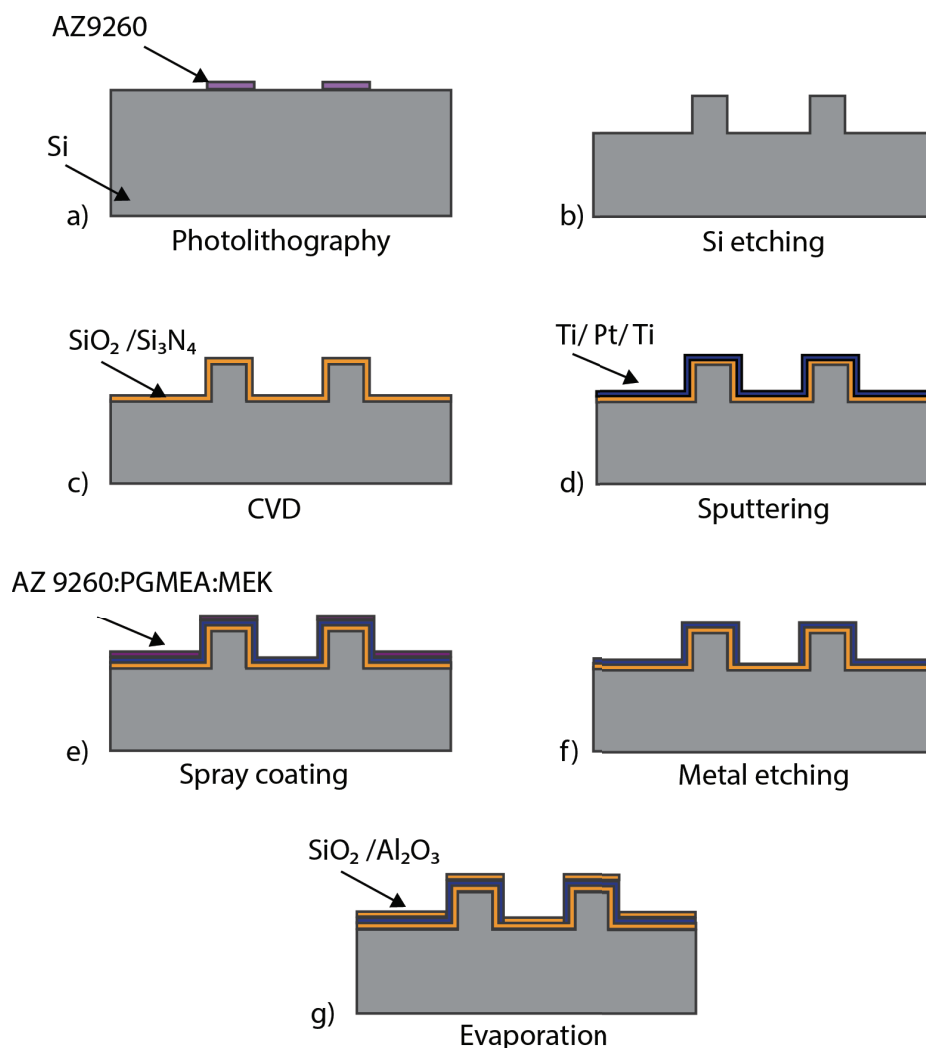


Figure 3.1: Fabrication process of metal-coated 3D silicon micropillars. Cross section of the silicon chip in correspondence of the microelectrodes array. Resist pattern (a) is transfer into the silicon by Bosch process (b). Silicon is passivated (c) before to cover it with a metal film by metal sputtering (d). The metal on horizontal surfaces is patterned by spray coating (e) and etched away by means of dry etching (f). An insulating layer is finally evaporated (g).

3.2.2 Electron microscopy characterization of micropillar arrays and their connection lines

After the fabrication, the Scanning Electron Microscopes (SEM, ZEISS LEO and ZEISS MERLIN) were used to inspect the metal patterning. An energy dispersive X-ray detector (EDX, Oxford Instruments EDX X-MAX) mounted on the Scanning Electron Microscopes (SEM, ZEISS MERLIN) was employed to analyze the material composition of the vertical sidewalls in order to further confirm the presence of platinum on the sidewalls of the electrodes. Data were treated using the AZTEC software (Oxford Instruments). Figure 3.2b and c show EDX analysis of the sidewalls of the pillars. Silicon, platinum and nitrogen peaks were identified. The presence of nitrogen is due to the passivation layer of silicon nitride underneath the metal layer. The Ti peaks could not be measured due to the limited thickness of the layer.

The patterning of the metal layer inside the gaps was observed through SEM. For this purpose, we realized arrays of 50 μm high pillars with different shapes (square and round), dimensions (10–70 μm) and gaps (10–60 μm). The SEM picture in Figure 3.2a shows uniform metal coverage of the pillar sidewalls and the continuity, with the horizontal metal layer constituting the wires.

The patterning of metal connections between the pillars was achieved using spray coating. This technique allows for more homogenous coatings, especially for sub-

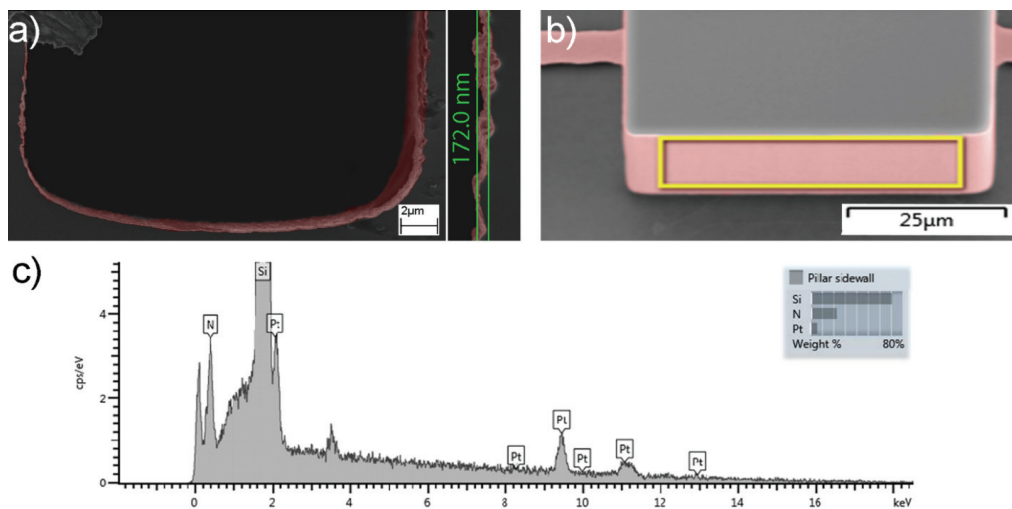


Figure 3.2 (a) Section of a 20 μm gap between two 50 μm -high pillars. The colored SEM picture shows the conformity of the metal layer (Ti/Pt 20/200 nm) on the vertical sides of the pillars and on the gap bottom. Inset: details of the metal layer on the pillar vertical sidewall; (b) vertical sidewall of a pillar. The region marked by the rectangle has been characterized by SEM-EDX and resulted in the spectrum represented in (c).

strates with high topography, since the layer is sprayed uniformly on the entire wafer, which means it does not need to be spread by centrifugal forces [126].

We noted that treating the photoresist coating with oxygen plasma before spray coating and employing freshly deposited clean metal surfaces play an important role in achieving the best adhesion and uniformity of the coating. Since smaller droplets adhere better to the substrate, the resist was applied accordingly, starting with a low dispense rate (5 $\mu\text{L/s}$). Additional resist was then sprayed, increasing the dispense rate at each passage over the wafer up to 60 $\mu\text{L/s}$. This procedure was chosen since an increased dispense rate leads to the formation of bigger droplets, which are more favorable for adhering to already deposited resist and also lead to a smoother surface [127].

The wafer was rotated while the spray nozzle was moved over the wafer in order to achieve coverage of all sides of the pillars; however, the rotation was kept at a low spin speed (20 rpm) in order to minimize the centrifugal force effects. Nevertheless, photoresist accumulation and inhomogeneity in resist thickness were observed between the pillars, and a dependency between gap size and resist accumulation was also observed. Arrays with smaller gaps result in greater accumulation inside the gaps than similar arrays with bigger gaps. This can be explained by two effects. Firstly, more resist is deposited in a small gap, since the ratio of vertical surfaces to horizontal surfaces is higher. Secondly, capillary forces have a greater effect in small gaps than in larger gaps.

To achieve a sufficiently high exposure dose for the full resist thickness in critical regions, the dose had to be increased. While a dose of 210 mJ/cm^2 was sufficient to pattern planar regions, doses of up to 780 mJ/cm^2 were necessary to pattern into the arrays with smaller gaps. The fact that the patterning of the metal layer of planar regions and arrays was achieved in the same step meant that planar regions were overexposed. Moreover, during exposure of the resist, a gap separating the wafer from the mask appeared due to the presence of the pillars. The combination of the gap and overexposure led to an important shrinkage of planar features, particularly those located far from the pillars.

SEM imaging was used to characterize this effect by measuring the shrinkage of planar test structures consisting of 10 lines with nominal width ranging from 5 μm to 50 μm . Figure 3.3a shows SEM images of five of the 10 planar metal lines, while Figure 3.3b shows the distribution of the shrinkage of this set of lines over 96 measurements. The shrinkage corresponds to an average of 6.52 μm , with a standard deviation of 1.14 μm . Furthermore, we observed that shrinkage was less evident for gaps between the square-shaped pillars (Figure 3.3c) than for the round-shaped pillars (Figure 3.3d). This observation agrees with the explanation above, since the spacing between square-shaped pillars is narrower than the round-shaped ones due to larger facing surfaces in the case of square-shaped pillars.

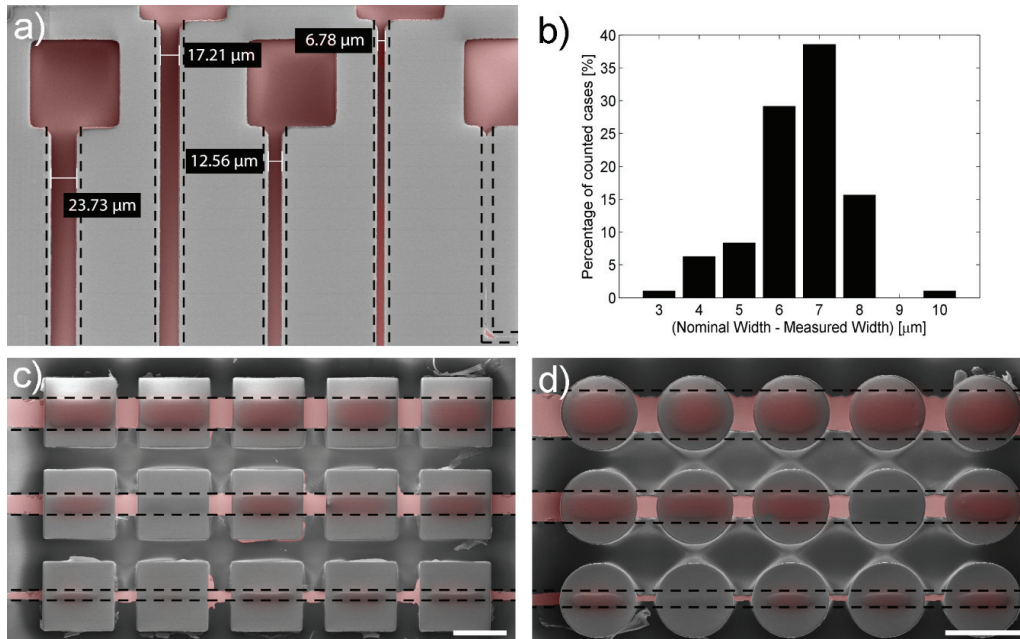


Figure 3.3 (a) Shrinkage of the planar lines due to photoresist overexposure. Dashed black lines indicate the patterns on the original mask design; (b) Bar chart of measured shrinkage over 96 measurements; (c)–(d) patterned connection lines in between pillars for square-shaped pillars with a 20 μm gap and round-shaped pillars with 10 μm gap ((c) and (d), respectively). The nominal width of the lines is 10 μm , 20 μm and 30 μm from bottom to top. Scale bars are 50 μm .

3.3 Electrical characterization of microelectrodes

3.3.1 Resistivity of micropillar arrays

We developed silicon chips featuring sets of five connected round-shaped pillars of different size, spacing and wire width in order to evaluate the resistivity of connection lines that comprehended metal-coated micropillars and to identify the critical features for the proposed technology. In particular, our purpose was to evaluate the metal thin film continuity between planar wires and vertical pillar sidewalls and the impact that the pillars have on the resistivity, particularly with respect to their dimension and position. The diameter of the pillars varied from 10 μm to 70 μm and the spacing between them ranged from 60 μm down to 10 μm . Each array consisted of five adjacent pillars connected by a metal line of 10 μm , 20 μm , or 30 μm in width, ending with two opposite pads (indicated as A and B in Figure 3.4). Test structures consisting of standard horizontal line patterns having a width between

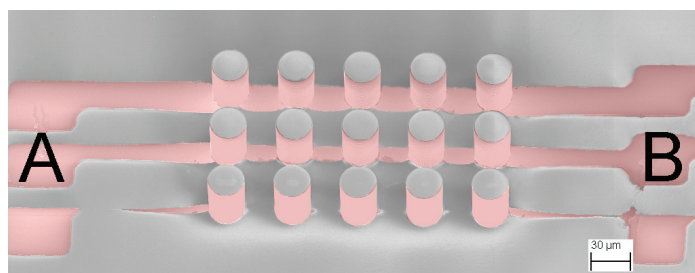


Figure 3.4: SEM image of three sets of five round-shaped micropillar electrodes. The micropillars have a $30\ \mu\text{m}$ diameter and a $20\ \mu\text{m}$ gap between them. Platinum planar lines from $10\ \mu\text{m}$ to $30\ \mu\text{m}$ in width (bottom to top) connect each single array from point A to point B, through the five pillars. Metal surfaces were highlighted on the image by colorization of the corresponding regions.

$5\ \mu\text{m}$ and $50\ \mu\text{m}$ were fabricated on the same layout.

The purpose of the final passivation step of the chip surface is to insulate the metal wires from an electrolyte solution. This step was not applied on these chips since measurements were performed in dry conditions.

Measurements of electrical conductivity on the five-pillar arrays were performed in dry conditions with a Keithley 2400 SourceMeter and a Karl Süss PM8 probe station. We measured the electrical resistance of lines of five round-shaped pillars, connected by a metal wire with a nominal width of either $20\ \mu\text{m}$ or $30\ \mu\text{m}$. The sets of pillars also differ in diameter ($20\text{--}70\ \mu\text{m}$) and spacing ($10\text{--}60\ \mu\text{m}$).

The measured resistances of the lines with different geometrical features varied from $14\ \Omega$ to $90\ \Omega$. Figure 3.5 reports the data for lines obtained on two different wafers. The plots report the resistance normalized by the total length of the corresponding array, including the connection lines to the pads (Figure 3.4 from point A to point B). While electrical connection was successfully achieved for each array, the normalized resistance was shown to be mainly affected by the gap size, resulting in higher resistance in cases of smaller gaps. Figure 3.5a shows the inter-chip variability (18 chips) of the resistance per unit length plotted vs. the gap size between the pillars. This plot reports the measurements on arrays having the same pillar diameter ($30\ \mu\text{m}$) and line width ($20\ \mu\text{m}$). Normalized resistance ranges from approximately $40\ \text{m}\Omega/\mu\text{m}$ to $90\ \text{m}\Omega/\mu\text{m}$, with a maximal variability of 10 percent. Figure 3.5b reports the normalized resistance of lines with different gap sizes, pillar diameter, and line width. No relationship can be found between the resistance of the array and the pillar diameter, which ranges from $20\ \mu\text{m}$ to $70\ \mu\text{m}$. As expected, the resistance decreased when the line width was increased from $20\ \mu\text{m}$ (crosses) to $30\ \mu\text{m}$ (circles). This analysis only considered the arrays for which the pillar diameter was equal to or larger than the line width. This choice was motivated by the intention to exclude cases in which the electrical current was allowed to circumvent the pillars.

We compared the normalized resistance of the pillar arrays with the normalized

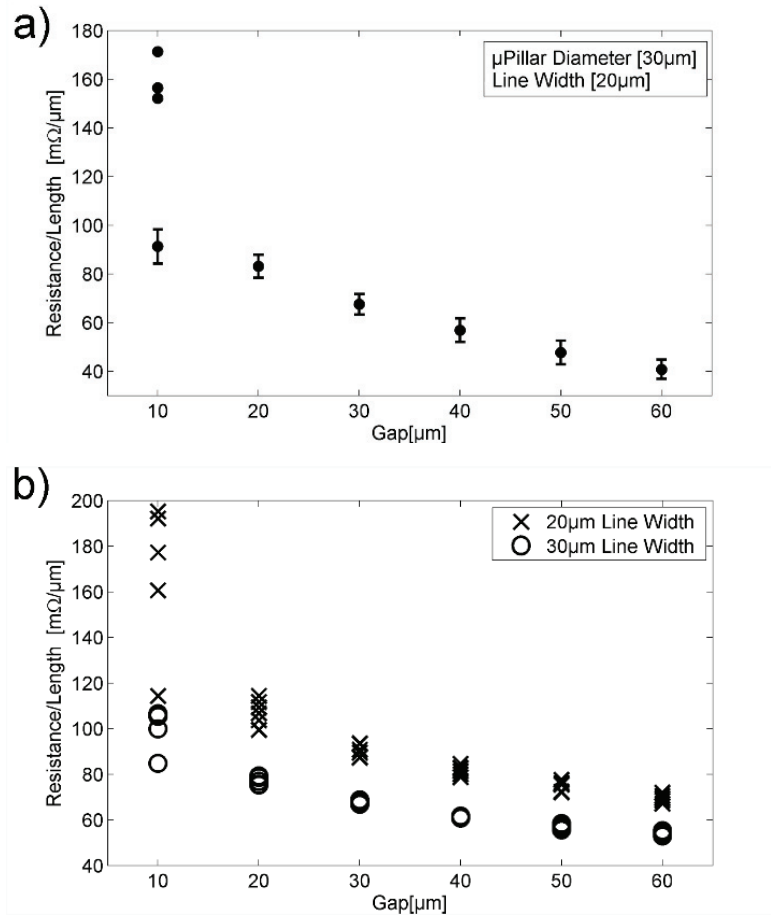


Figure 3.5 (a) Inter-chip variability (18 chips) of the resistance of the arrays, normalized by the array length, vs. the gap between pillars. In the case of 10 μm gap, three out of 18 normalized resistance values were found to be substantially higher, thus they were indicated separately on the plot; (b) resistance of the arrays normalized by the array length, vs. the gap between pillars. Circles represent 30 μm -width lines and crosses represent 20 μm -width lines. Pillar diameter ranges from 20 μm to 70 μm (b).

resistance of the planar lines implemented on the same chip. We observed an increase of the normalized resistance due to the presence of the pillars, which was maximal for the 10 μm gap and corresponded to approximately four times the normalized resistance of the planar lines.

Overall, we can conclude that gap size is the main parameter that affects the resistance of the pillar lines. This effect can be explained by considering that the amplitude of the sputtering angle in the gap region is reduced during metal deposition, which leads to a thinner metal layer inside the gaps and on the sidewalls of the pillars.

3.3.2 Impedance characterization of free-standing micropillar electrodes

A specific micropillar layout was conceived in order to facilitate the coupling of the chips with a microfluidic channel to perform electrical impedance measurements in wet conditions. Two adjacent $50\ \mu\text{m}$ high micropillars with a width of $40\ \mu\text{m}$ and spacing of $40\ \mu\text{m}$ (Figure 3.6) were located in a $130\ \mu\text{m}$ -large flow channel obtained by bonding a PDMS cover to the chip. The upstream and downstream faces of the micropillars exhibit a rounded shape to improve the hydrodynamic behavior by reducing the flow perturbation (Figure 3.6a). In this design, each single pillar is connected by a $1\ \text{cm}$ long horizontal metal line to a dedicated pad located on the chip border outside the PDMS-bonded region. The PDMS cover was obtained from an SU-8 mold. The PDMS and chip surface were cleaned with an isopropanol bath for 10 min and then bonded by oxygen plasma (100 W, 0.6 mbar, 12 s, Diener Electronics, Femto) (Figure 3.7).

Impedance spectroscopy was performed in both dry and wet conditions. The microfabrication process includes the final surface passivation by SiO_2 , as described above, in order to insulate the horizontal metal wires from the electrolyte solution. The resulting pillars expose platinum on their vertical surfaces, while the horizontal wires lie beneath an SiO_2 passivation layer.

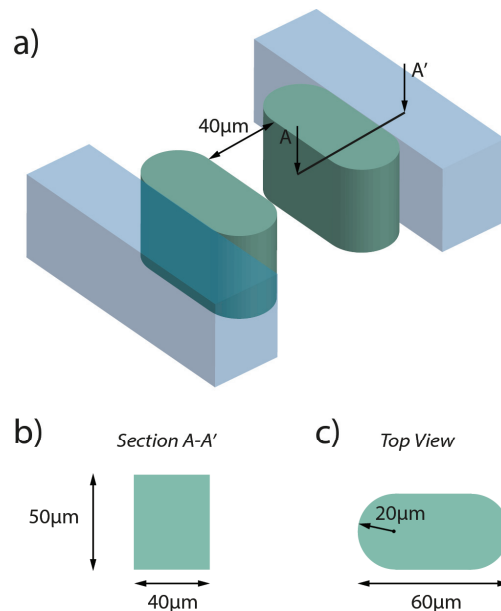


Figure 3.6: a) Schematic representation of a 3D view of a metal-coated micropillar in a microfluidic channel. b) schematic cross-section and c) top view section of the micropillar.

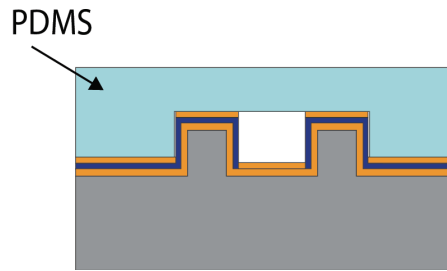


Figure 3.7 Schematic representation of the side view of the microfluidic channel hosting the microelectrodes. A PDMS cover obtained from an SU-8 mould was bonded on the silicon chip by oxygen plasma.

A PCB was designed to hold the chips and to provide electrical connection. The backside of the chips was connected to ground in order to suppress capacitive coupling between the metal wires on the chip and the silicon substrate. The micropillar electrodes were characterized using an Agilent 4294A Precision Impedance Analyzer (Agilent Technologies, Santa Clara, CA, USA) acquiring data in LabView (National Instruments Corp., Austin, TX, USA). Data were then analyzed in Matlab (Mathworks, Natick, MA, USA). The electrical characterization of the pillars inside the channel was performed both in air and in PBS 1X (Phosphate Buffered Saline, Sigma–Aldrich) solution. Impedance spectra were obtained over 201 measurement points distributed logarithmically between 10^3 Hz and 10^6 Hz, with an excitation signal of 50 mV. In order to identify the equivalent electrical components, data points were fitted in ZView (Scribner Associates, Inc.). Equivalent electrical parameters of the device formed by two micropillar electrodes in solution were extracted using both dry and wet measurements.

From the measurements in dry conditions, it is possible to extract the geometrical capacitance between the micropillars in air, which includes the contribution of the connection lines. Impedance spectra in dry conditions show purely capacitive behavior (Figure 3.8a) and the geometric capacitance can be estimated as 55 pF. The measurements in wet conditions (performed by means of the Impedance Analyzer), which are reported on the same plot, show the occurrence of the electrode/solution interface capacitance of the vertical platinum sidewalls.

The impedance spectra of the microelectrodes in solution can be modeled using the equivalent electrical circuit shown in Figure 3.8b. The Constant Phase Element (CPE_{DL}) accurately describes the peculiar interfacial double-layer capacitance at the electrodes and can be observed at frequencies lower than 10^4 Hz.

Frequencies between 4×10^4 Hz and 5×10^5 Hz are dominated by a resistive behavior, which depends on the solution resistance, R_{buffer} . The parasitic capacitance C_{stray} , which is mainly due to the capacitive coupling between the electrodes, is observed at frequencies higher than 5×10^5 Hz. Finally, an additional element that consists of a parasitic resistance R_{PAR} in parallel with a capacitance C_{PAR} is in series with the electrode impedance.

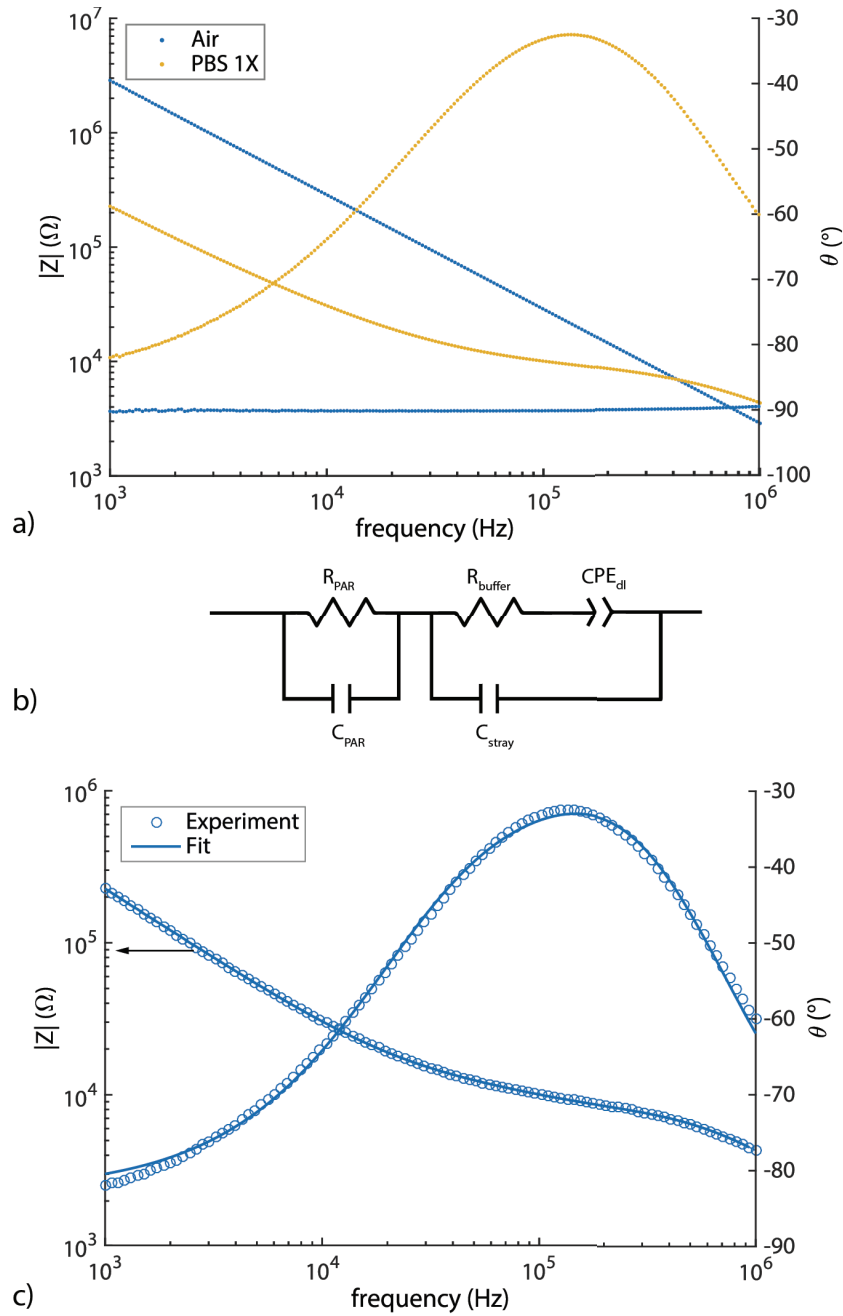


Figure 3.8: (a) Impedance modulus and phase of two adjacent micropillar electrodes in dry (solid lines) and wet measurement conditions (dashed line); (b) equivalent circuit of the two pillars in the microfluidic channel used for fitting; (c) fit of the experimental data. Only 101 frequency measurement points out of the 201 sampled are represented on the plot.

The data obtained were fitted with the described model in ZView (Scribner Associates, Inc.) in order to extract the values of each component. The extracted electrical parameters are fitted with errors below 3 percent, indicating the suitability of this

electrical model to represent our samples (Table 3.1).

The presence of a large capacitance at low frequencies can only be attributed to the existence of an electrode/solution interface; this further demonstrates the exposure of the platinum on the pillar sidewalls to the solution. Following the procedure reported by Brug et al., the effective capacitance corresponding to the extracted constant phase element was found to be $1.3 \mu\text{F}/\text{cm}^2$ [128].

Table 3.1: Values of the electrical parameters for two micropillar electrodes in a microfluidic channel extracted by fitting of the equivalent circuit in Figure 3.8 b

	R_{buffer} (Ω)	$\text{CPE}_{\text{DL-}Q}$ ($\text{nF}\cdot\text{s}^\alpha$)	$\text{CPE}_{\text{DL-}\alpha}$	C_{stray} (pF)	R_{PAR} (Ω)	C_{PAR} (pF)
Value	12246	1.26	0.88	2.82	7206	0.36
Fitting error (%)	2.9	1.6	0.2	1.5	0.5	0.3

3.4 Integration of microelectrodes with SU-8 microfluidic structures

3.4.1 Fabrication process of SU-8

The microfluidic structures were fabricated in a SU-8 lithography step, after the fabrication of the metal-coated 3D pillars. In this case, the wafer is diced just after the additional SU-8 lithography step described here. A $50 \mu\text{m}$ -thick SU-8 (Gersteltec GM 1070) layer is spin-coated at 1600 rpm, matching the height of the 3D pillar electrodes. A soft-bake is performed at 90°C for 5 min and then exposed to UV at a dose of $400 \text{ mJ}/\text{cm}^2$ (Karl Süss MJB 4). A post-exposure bake is executed at 90°C for 30 min to catalyze cross-linking, followed by development in propylene-glycol-monomethyl-ether-acetate (PGMEA).

SU-8 makes it possible to integrate microelectrodes into microfluidic structures, with three purposes: (i) to define the walls of microchannels with lithographic precision; (ii) to electrically passivate, in a selective manner, the vertical faces of the microelectrodes (due to the insulating properties of SU-8); and (iii) to improve the hydrodynamic behavior in the microchannel by reducing the flow perturbation.

SU-8 microfluidic structures were fabricated after the 3D electrodes directly on the

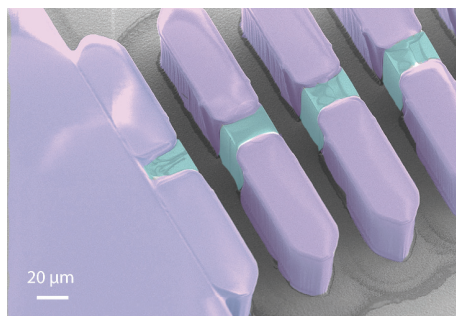


Figure 3.9: Coloured SEM image of SU-8 microfluidic channel integrating silicon-based 3D microelectrode. The 3D microelectrodes are coloured in green, while SU-8 is coloured in violet.

chip. This enabled the alignment of channels and 3D structures with photolithographic precision. Fabrication parameters were tuned to achieve an SU-8 layer of the same height as the metal-coated microelectrodes (see Figure 3.9).

3.4.2 Impedance characterization of micropillar electrodes combined with SU-8 microfluidic structures

Impedance spectroscopy was also performed using 3D electrodes integrated in SU-8 microfluidic structures, as schematically shown in Figure 3.10a. In this case, adjacent $50\ \mu\text{m}$ high micropillars with a $30\times 30\ \mu\text{m}^2$ base (Figure 3.10) were located in a $95\ \mu\text{m}$ wide microchannel. At the upstream and downstream faces of micropillars, SU-8 microfluidic extrusions passivated the electrode surfaces. Each single pillar was connected by a 1 cm long horizontal metal line to a dedicated pad located on the chip border outside of the PDMS-bonded region, as in the chip described previously. PDMS was bonded on the silicon chip following the same procedure as above

In this case, the chip cleaning performed prior to the PDMS bonding required further attention due to the presence of SU-8 structures. The chip was gently rinsed with IPA in order to remove the larger amounts of the positive resist used as protective layer during dicing. Bath in IPA was avoided due to the presence of SU-8 that might be attacked by the solvent. Hence, further residues of positive resist were removed only following the PDMS bonding, directly accessing the microchannel. Filtered IPA was injected at $30\ \mu\text{l}/\text{min}$ for approximately 2 min in the microchannel and immediately rinsed by injecting Milli-Q ($30\ \mu\text{l}/\text{min}$ for 10 min) to prevent SU-8 adhesion. The presence of the PDMS bonded directly on the silicon chip help to avoid the SU-8 detachment during the chip cleaning.

SU-8 extensions of the 3D microelectrodes made it possible to reduce the size of the

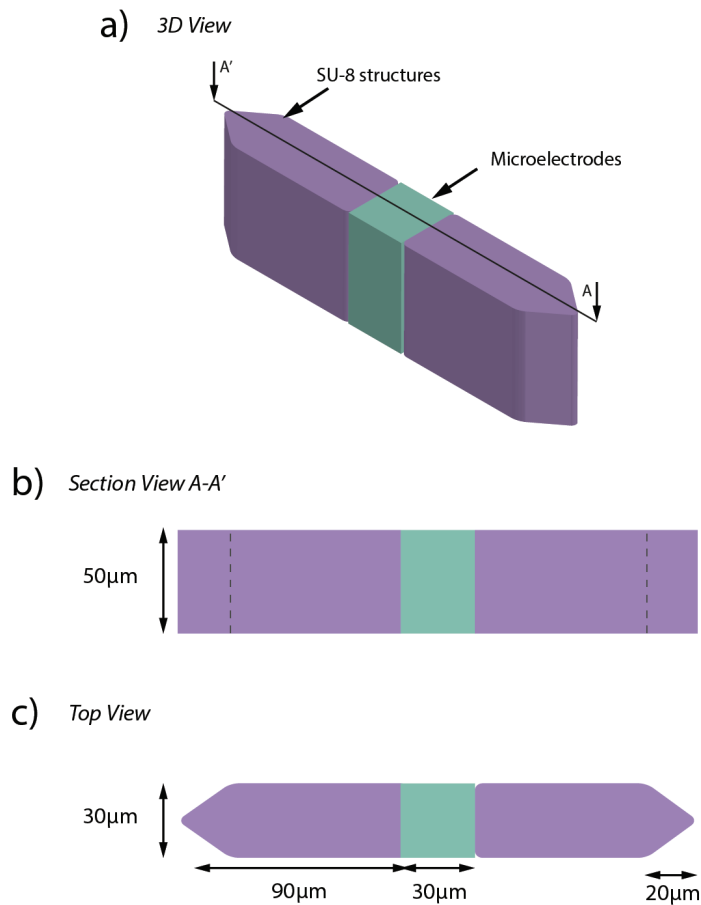


Figure 3.10: (a) 3D view of a metal-coated micropillar; (b) the schematic cross-section; and (c) the top view section of the micropillar.

electrodes surface exposed to the solution in the microchannel, which had several implications. Reducing the size of the electrodes turns on a higher electric field line concentration, constraining the current paths into a smaller volume around the cell or the particle under test (see Figure 3.11). Finally, the presence of the SU-8 prevents cells collision with microelectrodes, which would happen particularly at low flow rates and would generate ripples in the electrical signal.

Figure 3.12a and b shows the impedance spectra in wet conditions of free-standing micropillar electrodes (Figure 3.11a) and of micropillar electrodes featuring upstream and downstream SU-8 extensions (Figure 3.11b). Measurements were performed by means of the lock-in amplifier (HF2LI) and a current amplifier (HF2TA) by applying a 100 mV simulation voltage.

Similarly, to the Bode plot described above, the effect of the double-layer capacitance and the resistance of the solution are visible at frequencies below $2 \cdot 10^4$ Hz. As expected, impedance is overall higher for the micropillars featuring SU-8 extensions

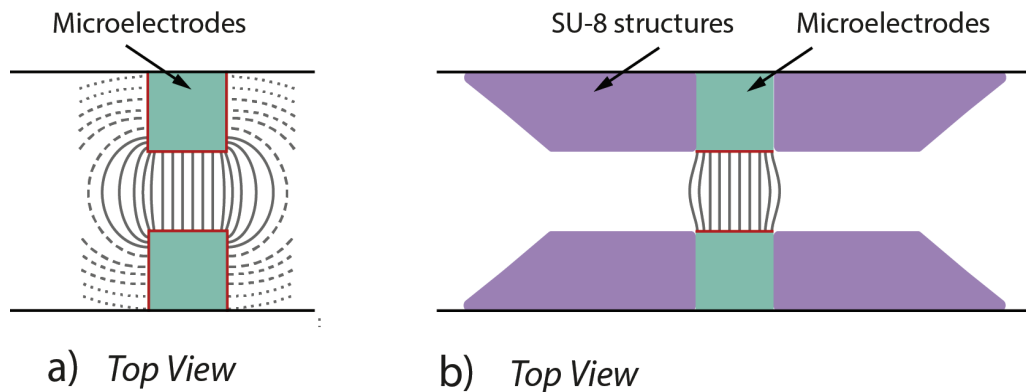


Figure 3.11: (a) Top view schematic representation of the current path between two free-standing microelectrodes (in green) and (b) of two microelectrodes with SU-8 extensions (in violet).

because of the reduced electrode area exposed to the electrolyte. In fact, SU-8 structures passivate a portion of the electrodes' surface, which results in a decrease of the double-layer capacitance (visible at low frequency in the range of $10^3 - 2 \cdot 10^4$ Hz) and in an increase of the resistance of the solution (visible in the range of $2 \cdot 10^4$ Hz - $4 \cdot 10^5$ Hz). Beyond 10^6 Hz, the effect of parasitic elements is evident and the HF2TA preamplifier introduces a phase offset as a function of frequency from 1-2 MHz. The values of the electrical elements obtained by fitting the measurements with the model in Figure 3.8b are shown in Table 3.2.

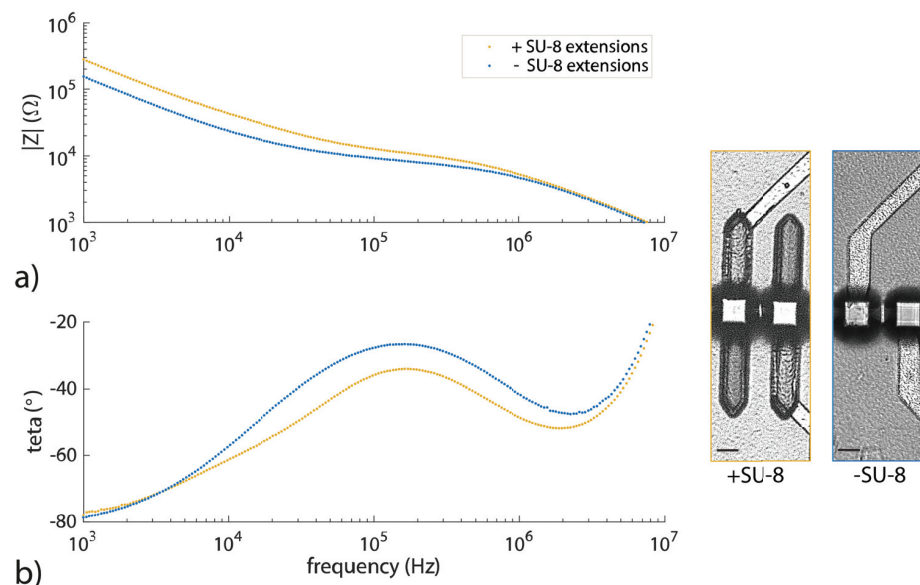


Figure 3.12: Impedance modulus (a) and phase (b) acquired in wet conditions of two adjacent free-standing micropillar electrodes (blue dots) and integrated in two SU-8 extensions (yellow dots). Microscopy image (101 frequency measurements are represented in the plot).

Table 3.2: Values of the electrical parameters for two micropillar electrodes without (indicated as '-SU-8') and with SU-8 extensions (indicated as '+SU-8') extracted by fitting the equivalent circuit in Figure 3.8 b

		R_{buffer} (Ω)	$\text{CPE}_{\text{DL-Q}}$ ($\text{nF}\cdot\text{s}^\alpha$)	$\text{CPE}_{\text{DL-}\alpha}$	C_{stray} (pF)	R_{PAR} (Ω)	C_{PAR} (pF)
-SU-8	Value	6500	3.23	0.86	62	2884	18
	Fitting error (%)	1	2.3	0.2	3.4	3	2.5
+SU-8	Value	9797	2.49	0.82	35	1925	13
	Fitting error (%)	0.6	1.8	0.2	1.9	3.2	7.4

3.5 Summary

We have presented a new fabrication process to realize freestanding pillar electrode arrays with metal coverage of the vertical sidewalls. The fabrication is based on standard silicon machining technologies, which offers advantages in terms of availability of equipment as well as compatibility with other processes. The fabrication process presented here is CMOS-compatible and could be implemented together with circuits in order to, for example, address a large number of pillar electrodes.

The two most critical steps for the fabrication are the metallization of the vertical sidewalls of the pillars and the patterning of metals in between closely spaced pillars. The presence of the metal was confirmed using different methods, such as imaging, surface analysis and electrical measurements, and was found to form a homogenous layer. The minimal gap that it could be patterned into was found to be 10 μm for round-shaped pillars and 20 μm for square-shaped pillars. Therefore, the proposed technology makes it possible to develop arrays with pillars that can be addressed one by one, or to realize connected pillars that are on the same lines.

During the patterning of the metal layer, planar features experience shrinkage in a way that is influenced by the topography of the substrate, due to high exposure doses and a resulting exposure gap. The topography of the substrate was found to have an influence on the shrinkage. Planar features in low topography regions were found to suffer the most from shrinkage, determining a mean size reduction of about 6.5 μm . However, the high repeatability of the extent of the shrinkage makes it possible to compensate for this effect in the design of the layout. The shrinkage within the gaps depends on the gap size and on the pillar shape. Shrinkage was found to be consistently more important for bigger gaps. The smaller gaps lead to higher photoresist accumulation, which means that higher exposure doses are necessary to entirely develop features inside the smaller gaps. Since different arrays were

developed in parallel the same substrate, the photoresist inside larger gaps was over-exposed.

One of the main advantages for the obtained pillars is their metal coverage and the possibility to use metal connection lines that result in low resistivity of such electrode features. Lower resistance of the electrodes results in better performance for measuring signals with small amplitude and reduces Joule heating of the medium when the electrodes are used to apply signals.

Test structures with five pillars were connected with lines of different widths in order to characterize the resistance of the pillars and their connection lines. The resistance of these structures was found to be in the range of tens of Ohms. The presence of the pillars was found to increase the resistance values by only four-fold, most of which depended on the gap dimension. The option to build the pillars out of silicon makes it possible to apply only thin layers of expensive metals on the pillar sidewalls. This represents an advantage with respect to other techniques, such as electroplating, in which the resulting pillars are made from one specific conductive material. Furthermore, with electroplating it is generally challenging to achieve both good surface properties and precise geometries. On the other hand, the fabrication process proposed here makes it possible to realize any pillar geometry that is compatible with photolithography and dry etching. Moreover, the presented technology makes it possible to achieve sharp edges, as opposed to techniques such as C-MEMS, which involve shrinkage of the precursor that occurs during pyrolysis.

The described fabrication process for passivated freestanding 3D silicon pillars coated with metal is suitable for use with various lab-on-a-chip applications. This process makes it possible to achieve arrays that consist of high-aspect-ratio pillars exposing metal on their sidewalls and exhibit well-defined cross-sections. Finally, the combination of 3D microelectrodes with SU-8 structures opens up a range of opportunities in the design of new layouts of microfluidic devices.

In particular SU-8 structures can be used as passivating extensions of the microelectrodes, as shown in this case, but they might be also patterned to integrate the microelectrodes and form trapping sites for cell analysis and manipulation (0). The majority of the presented results have been published in [123].

4 | APPLICATION OF 3D MICROELECTRODES: TOWARDS LABEL-FREE SENSING OF SINGLE ACTIVATED T CELLS

In this chapter we describe the employment of silicon-based 3D microelectrodes for in-flow label-free and single-cell detection of T lymphocytes activated in vitro. The microelectrodes employed, which are fabricated following the process described in Chapter 3, present passive upstream and downstream extensions. We preferred to use the silicon-based approach (Chapter 3) instead of the SU-8-based one (Chapter 22) for its higher reliability and straightforwardness, despite the fact that the use of silicon might introduce capacitive couplings through the substrate at higher frequency. SU-8 based fabrication revealed critical issues in achieving and preserving the electrical contact between the vertical side of the microelectrode and the horizontal metal line, due to the poor adhesion properties of SU-8.

3D microelectrodes were used to measure the impedance change associated with the activation of primary CD8⁺ lymphocytes. Measurements were performed at electrical frequencies maximizing the difference between non-activated and activated T cells.

The proposed impedance flow cytometer highlights the possibility of using impedance to assess single T cell activation in label-free suggesting the intriguing possibility of employing this technique in cell immunotherapy. The motivation of this work stems from the great interest in methodologies for the non-invasive analysis and manipulation of cell samples. This is particularly true in the context of adoptive immunotherapy, where the processing and characterization of activated immune cells to reemploy therapeutically should be minimal, to avoid critical modifications. The challenging application we propose arises from the collaboration with the Ludwig Centre for Cancer Biology (Lausanne, Switzerland).

4.1 Introduction

4.1.1 The role of T cells and their activation

The immune system operates as defense against harmful cues originating from the environment or from abnormalities in the organism's physiology (as is the case for many types of cancers) [129]. The immune system response is divided into innate and adoptive, also defined as nonspecific and specific, respectively. White blood cells (also called lymphocytes), play a key role in establishing and coordinating the immune response. They are generally distinguished in B cells and T cells, and these last ones have a central role in the adoptive cellular immune response. In particular, cytotoxic T lymphocytes (CD8⁺) are the responsible for the effector function [129], since they directly attack target cells by secreting lytic enzymes causing the death of the cells [130]. CD8⁺ cells are implicated against virus-infected cells, tumor cells and transplant rejection.

T cell precursors (denominated thymocytes) differentiate in the bone marrow and migrate to the thymus for maturation before moving through the tissues. After maturation, T cells are considered *naïve* until exposed to foreign antigens and to appropriate co-stimulator molecules that specifically activate their T cell receptors (TCR). Foreign antigens are typically presented on the surface of specialized host cells, called antigen-presenting cells (APC) [131].

With the engagement of the TCR complex, a number of signalling events leads to cell activation, a rather complex process that induces an immediate increase of the concentration of cytoplasmic calcium (Ca²⁺) and cytoskeletal rearrangements, which, in the context of T cell – APC cell interplay, favour and stabilize their interaction [132], [133]. Long-term effects of activation include proliferation and the expression of activation-associated genes which triggers the differentiation from the naïve state [134].

A number of strategies to generate, educate, and/or empower T cells against tumors have been developed during the last 60 years, [135], [136] leading to two main different strategies to stimulate antitumor immunity: therapeutic vaccination and passive immunization. Passive immunization, also known as adoptive T cell therapy (ACT), is a promising powerful approach for cancer treatment that relies on the infusion of tumor-specific T cells expanded *ex vivo* for mediating tumor attack in the host (Figure 4.1). Currently there are no FDA-approved ACTs for cancer, but ongoing clinical trials of adoptive T cell transfer have begun in recent years for

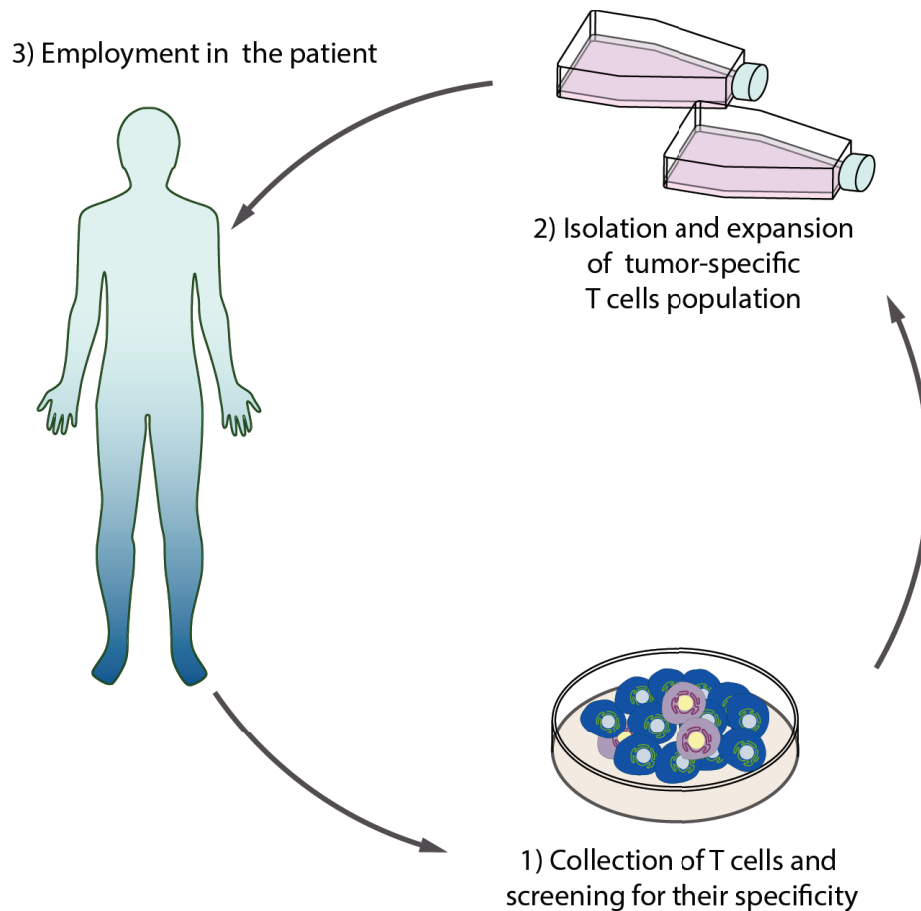


Figure 4.1: Schematic representation of a possible adoptive cell immunotherapy strategy. Tumor mass can be excised from patient to extract T cell population (1). Upon stimulation with specific antigen, activated T cells, which have the desired TCR, can be detected and expanded (2) and then adoptively transferred into patient (3).

melanoma [137] and other malignancies including, cervical cancer, lymphoma, leukemia, bile duct cancer, and neuroblastoma [138].

Tumor-specific T cells can be harvested in different ways starting from both tumor-infiltrating lymphocytes (TIL) and peripheral blood lymphocytes (PBL) [139]. In the first case, TILs can be isolated from cancer tissue, since they are preferentially tumor-specific, expanded non-specifically *in vitro*, and infused back into the patient. PBLs instead can be isolated from peripheral blood, subsequently they can be either non-specific or antigen-specific stimulated, and then expanded *in vitro* before to be reinfused. PBLs can be furthermore genetically engineered to express engineered cell receptors before expansion [140]. These receptors can be traditional TCRs, or they can be chimeric antigen receptors (CARs), which are antibody single-chain variable fragments joined with TCR [137]. Promising results, including mediation of tumor regression, have been already shown employing modified antigen-specificity of PBLs in humans, so that genetically modified T cells to target cancer made immunotherapy being designated as the Science's "Breakthrough of the Year"

in 2013 [141].

In the perspective of personalized immunotherapy, some research teams at the Ludwig Centre for Cancer Biology (Lausanne, Switzerland) (LCCB) currently aim to interrogate T cells (either circulating T cells or tumor-infiltrating cells) against a large panel of specific antigens, unique for each tumor/patient, in order to identify and validate immunogenic antigens. After a preliminary prediction of antigenic epitopes, *in silico* these have to be experimentally validated to demonstrate their antigenicity. A major technical limitation of this approach is represented by the validation of the predicted antigens. In other words, patient-specific T cells have to be screened to assess their activation upon exposure to cognate antigens, and this validation step requires a level of sensitivity that complies with the stringent requirements for the detection of antigen-responsive T cell clones (down to 0.6 – 60 cells over 10^6) [142].

The presence of antigen-specific T cells can be traditionally assessed indirectly by means of antibody-based assays, such as the ELISA or the ELISPOT. These are based on the detection of signaling molecules and secreted proteins produced by T cells with their activation [143]. More specifically, ELISA assays allow to measure the proteins in the culture and ELISPOT to quantify the frequency of single protein-releasing cells [144]. These are end-point assays, and notably they are laborious and indirect (the analytes are cell products, not the cells themselves). Other approaches, such as real time PCR, allow to highlight the accumulation of activation-specific mRNA transcripts in activated cells [145]. Also this technique is highly laborious and reagent-consuming, and most importantly, it requires the purification of RNA from individual cells. It is hence sample destructive, thus precluding the downstream re-employment of analyzed cells.

A routine approach to detect activated T cell relies on fluorescence-assisted cell sorting (FACS). This technique evaluates the expression of specific surface markers on activated cells, among which CD25, CD69, CD71, and HLA [146]. Although a well-established technique, it requires the staining, and in some cases the fixation, of cells together to multiple washing and incubation steps. An additional limitation of this methodology is that the detection of antigen specific T cells responding to a certain epitope often requires the preliminary expansion of cellular pools *in vitro*, due to the scarcity of antigen-specific clones. This process can introduce bias in the cells population [147] affecting the reliability of the analysis.

New methods sensitive to low frequency antigen-specific T cells *ex vivo* would improve the current detection and recovery approaches, allowing to characterize and isolate T cells with minimal loss and, importantly, without introducing alteration that would prevent the re-employment in patients for treatments.

The advancements in biocompatible microfabricated system has enabled the development of new strategies for single cell analysis which rely on microfluidic or arrays of microwells or traps to position them [148]. An interesting review of the recent

developments in microfluidics based immunology has been published recently [149] highlighting the current interest for the topic.

The advantages offered by microfluidics allowed to develop lab-on-a-chip platforms to identify and analyses T cells activation. In particular, microfluidic systems mainly allow to: (i) reduce the volume and so the consumption of expensive reagents and samples; (ii) improve experimental reproducibility and control by handling fluids automatically using custom designed chip architectures; (iii) accelerate biochemical reactions increasing the surface area to volume ratio; (iv) achieve large-scale parallelization analysis, hence increasing throughput; (v) profile single-cells considering heterogeneity of cell population.

Most microfluidic systems involve the use of fluorescent marker to label activated cells or the use of fluorescent probes to assess the cytoplasmic response to T cell activation (e.g. the cytoplasmic accumulation of calcium triggered by the activation process) [150]–[156]. The number of label-free on-chip solutions to assess T cells activation are still limited and, differently from label-based approaches, they offer clear advantages. In first instance, label-free assays are less invasive and suffer less from procedural bias. In fact, the identification of cells depends on cell intrinsic features that are not highlighted through markers, and are hence not affected by labelling errors. Some examples of label-free strategies that harness cell shape, deformability, density and dielectrical properties, and employ to detect activated T cells are described below.

4.1.2 Label-free strategies on chip for the detection of Activated T cells

In [157] Gossett et al. relied on changes in cell shape and deformability, which are related to cytoskeletal and nuclear reorganization, to examine activation of peripheral blood mononuclear (PBM) cells. By means of inertial focusing, cells are uniformly carried to a stretching extensional flow where they are deformed at high strain rates and monitored by a high-speed camera. An automated image processing analysis extracts mechanical information by measuring the initial diameter and the deformation of cells, defined as the ratio between the longest and the shortest perpendicular axis of the cell under stress.

PBM cells revealed more deformability and bigger dimensions upon stimulation due to a reorganization of the cytoskeleton and microtubule structures. The system of Gosset et al. attained remarkable throughput (approximately 2'000 cells/s) but suffered from the general drawbacks of optical detection, which require expensive a high speed camera and bulky setups that are difficult to miniaturize into low-cost

portable devices.

Another label-free approach, based on the quantification of single-cell mass, volume and density, is presented by F. Delgado in [158] using a suspended microchannel resonator that implements Archimedes' method in a microfluidic system. The resonator consists of a silicon cantilever with an embedded microfluidic channel. The cantilever oscillates under vacuum at a frequency proportional to its mass, and its vibrations are monitored optically. When a cell passes through the microchannel it changes the resonance frequency proportionally to its buoyant mass. In particular, two fluids of different densities are loaded in the microchannel and the buoyant mass measured. (Figure 4.2 describes more in detail the concept of the technology). The absolute mass, volume, and density of the cell can be determined by plotting the linear relationship between recorded buoyant masses and fluid densities. The authors validated the device also with naïve and activated CD8⁺ T cells. They observed lower dry density and higher dry mass for activated T cells with respect to unstimulated ones, as a result of the fact that, upon activation, changes in cell chemical composition occur. The increase of dry mass of activated T cells reflects the growth of cells, as they undergo proliferation, while the low mass values of naïve T cells reveal their compactness and little cytoplasm. Moreover, dry density - related to the chemical composition of cells (RNA, proteins, lipids, etc.) - is higher for naïve T cells. This possibly reflects their reduced cytoplasm and the density of organelles which are rich in lipids. Despite its high sensitivity, the system of Delgado et al. presents lower throughput (500 cells/hour) and it requires a complex system for a precise control of flow and of vacuum.

Alternative approaches based on the dielectric properties of cells can be used to assess T cell activation in label-free. Electrical-based measurements can be integrated

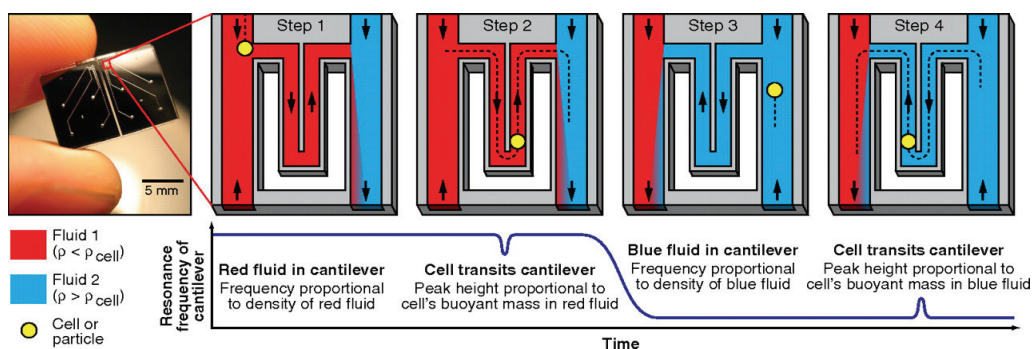


Figure 4.2: Schematics of the buoyant mass measurement using a suspended microcantilever. Single-cell density is evaluated by loading two different fluids in the channel. At first, the buoyant mass of a cell suspended in a low-density fluid is measured from the resonance peak. Then, when the cell enters in a greater density fluid, the direction of the flow is switched and the buoyant mass of the cell is measured in the high-density fluid. Pneumatic vacuum and two computer-controlled solenoid valves are required to control the flow [158].

easily on the chip taking advantage of the advancement of portable electronics. Different systems will be described more in details in the next section (4.1.3).

4.1.3 Electrical-based on chip solutions for activated T cells detection and characterization

The characterization of the dielectric properties of cells through dielectrophoresis (DEP) [159], [160], electrorotation (EROT) [160], [161] and IS (section 1.1) have a longstanding history in the context of label-free cell analysis and manipulation. These techniques, moreover, have been already successfully applied to assess the detection of activated T cells.

Hu et al. analysed the activation of T and B lymphocytes by EROT [162]. Upon mitogenic stimulation, the capacitance of cells considered to be activated (according to their change in size) was measured. Activated cells showed an approximate doubling of the membrane capacitance (up to $1.4 \mu\text{F}/\text{cm}^2$) and an increase of the membrane conductivity. Dielectric parameters of cell membrane and cytoplasm were derived from EROT and DEP analysis by fitting the single shell model to experimental data and assuming that cells are smooth spheres with complex membrane structures. The increase in membrane capacitance and membrane conductivity strongly correlated with the increase in size as cells enter in the cell division cycle after activation.

The authors support the idea that changes in membrane area, such as the dramatic increase in membrane folding, are the main cause of the specific membrane capacitance variation they observed and that the increase of membrane conductivity reflects, presumably, an increase in activity of ion transport pumps.

The possible correlation between dielectric properties and phases in the cell division cycle in activated T cells, was studied by Huang et al. using EROT [163]. They confirmed the increase in surface membrane capacitance observed by Hu et al. as cells moved from their resting G_0 phase into cell division cycle upon mitogenic stimulation. The authors point out how the change in membrane surface capacitance observed upon activation is not the result of the cell change in radius, since the increase in size would cause a reduction of capacitance, if the total membrane capacitance was preserved. Indeed, the specific membrane capacitance is defined as the total membrane capacitance divided by the surface area of a smooth sphere having a radius equal to that of the cell, according to the standard model. The total capacitance is instead determined by membrane dielectric permittivity and its area divided by its thickness [164]. Membrane structures, such as microvilli, ruffles, folds and blebs increase the total membrane area and hence the total cell capacitance. Upon activation, the surface configuration of the membrane displays increased sur-

face complexity, in terms of microvilli and its density, as revealed also by SEM analysis [163] resulting in the increase of surface capacitance.

Physiological changes in the membrane associated to T cell activation were explored also by Pethig et al. [165]. The authors investigate by DEP the possible relationship between the dielectrophoretic signal distributions and the cell cycle, corroborating the results reported with EROT by the previously described works.

The morphological change and the increase in adherence of activated T cell can be also monitored by impedance-based strategies [166]. Guan et al. recorded the impedance change of activated Jurkat cells with anti-CD3 and anti-CD8 antibodies by the impedance-based xCelligence system already described in (1.2.1). In this case, the stimulation of cells led to cytoskeletal rearrangement that resulted in an increase of the surface contacts between the sample and the sensor, causing an increase in electrical impedance signal.

In the light of the fabrication results reported in Chapter 3, we aimed to exploit our 3D microelectrodes to develop a microfluidic platform to measure, the impedance signature of activated primary CD8⁺ lymphocytes in suspension. The activation is performed by mitogenic stimulation with anti-CD3 and anti-CD28 antibodies. By this label-free approach we analyzed T cells sample suspended in physiological medium, without the need to adjust its conductivity, differently from DEP and EROT. Moreover, this approach based on impedance microcytometry allows to perform single-cell measurement, guaranteeing at the same time a high-throughput and overcoming the limitations of the other electrical techniques presented above.

4.2 Materials and methods

4.2.1 Device fabrication

The microfluidic device was fabricated as described in section 3.2 through a combination of thin-layer deposition, photolithographic and etching techniques. The 3D microelectrodes were combined with SU-8 to obtain chips with electrodes outlined on passive 3D structures embedded in a microfluidic channel as described in 3.4 (Figure 4.3). The microchannel was formed by bonding a PDMS module on the top of the chip (3.3).

The microchannel featured one single sensor composed of three micropillar electrodes aligned in the direction normal to the flow and occupying the entire width of the channel (150 μm). The micropillar electrodes were 30 μm wide, 30 μm deep and 50 μm high and were characterized by an inter-electrode gap of 30 μm . Each

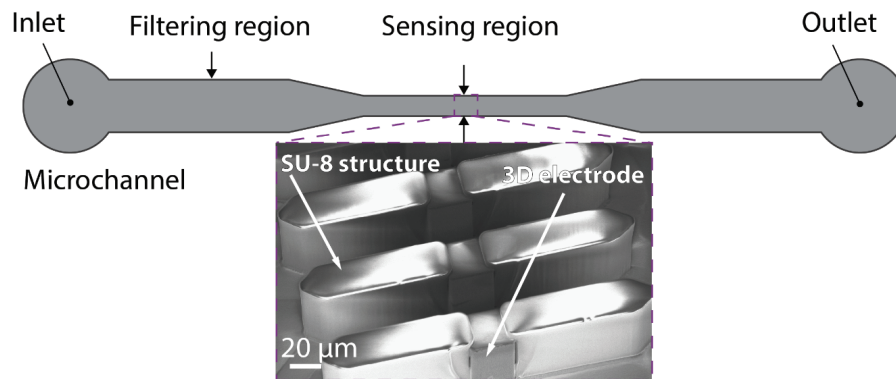


Figure 4.3: The schematic shows an overview of the microfluidic device. The dashed box shows the position of the impedance sensor in the microfluidic channel. The SEM pictures shows the 3D microelectrodes integrated in SU-8 passive structures (indicated by white arrows).

microelectrode was connected through individual planar lines to pads located on the chip border. The microelectrodes, the microchannel and both upstream and downstream SU-8 structures were fabricated with a matching height of 50 μm . In order to prevent clogging, SU-8 filters were placed 1.8 mm upstream of the sensor. The chip was clamped with a custom-designed poly(methyl methacrylate) (PMMA) holder and a printed circuit board (PCB) providing both fluidic and electrical connections. The PCB comprised spring-loaded pins to contact the electrode pads on the device once screwed on the PMMA holder. The silicon substrate was connected to ground.

Samples were loaded into a glass syringe and injected into the chip via silicone tubes under controllable continuous-flow by a syringe pump (Pump 11 Elite, Harvard Apparatus) at a flow rate of 1 $\mu\text{l}/\text{min}$. The device was primed with 100 mM NaOH and de-ionized water before injections and rinsed with the same solution after each

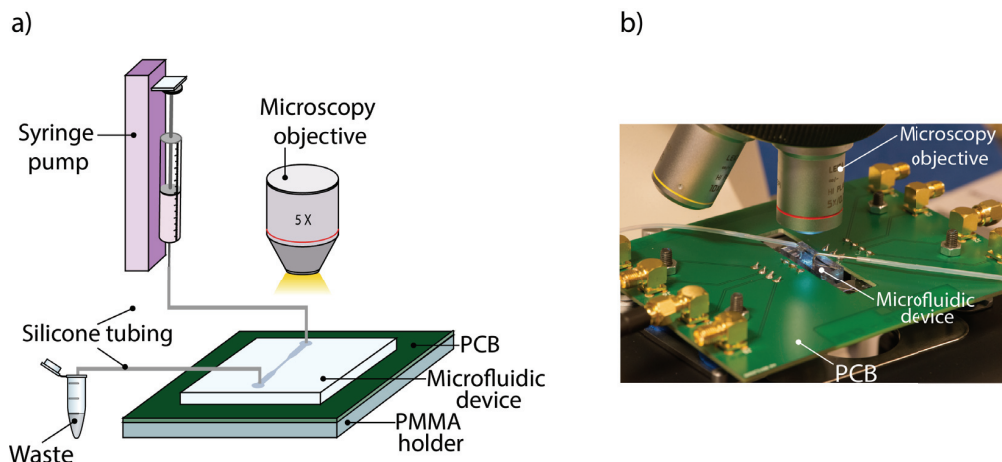


Figure 4.4: a) The sketch schematically shows the chip held in the PCB and docked onto the microscope. A syringe pump system provides the control of the fluid in the microchannel. b) Picture of the setup under the microscope.

measurement. When needed, a 0.02% Tween-20 PBS buffer was used to remove larger debris accumulated after injections. During the washing steps flowrates were always kept below 50 $\mu\text{l}/\text{min}$.

The chip was placed under an upright fluorescence microscope (DM2500 Leica) to observe, either in bright field or in fluorescence, the passage of cells through the 3D microelectrodes. Synchronized videos were acquired simultaneously to the acquisition of the electrical measurements by means of a high-speed sCMOS camera (Andor Neo 5.5). A schematic view and a picture of the setup are shown in Figure 4.4a) and b) respectively.

4.2.2 Impedance-based characterization of cells in flow

The impedance of cells flowing through the sensor was sampled in differential mode at a rate of 3100 samples/sec. An alternating voltage (V_s) of 400 mV amplitude and 0° phase was applied to the central microelectrode (labelled as '2' in Figure 4.5). The output signals from the two outer microelectrodes were converted and amplified by a transimpedance amplifier (HF2TA, Zurich Instruments) with a gain of 10 kV/A before being differentially recorded and demodulated by a lock-in amplifier (HF2LI, Zurich Instruments). The differential approach was chosen because it significantly reduces the electrical noise and cancels out thermal fluctuations and variations in the composition of the fluid [167].

The signal output of the lock-in is expressed as the in-phase and the 90° out-of-phase components of the current I_r (real and imaginary, respectively) and it is inversely proportional to the differential microchannel impedance under test (Z_m) according to:

$$I_r = \frac{V_s}{Z_m}$$

Equation 4.1

For this reason, the current signal can be directly used as characteristic signal in the measurements and displayed using either the in-phase and the out-of-phase parts of the magnitude and phase components.

The real and imaginary components of six demodulated frequencies in the 100 kHz - 27 MHz range were acquired simultaneously and used to characterize the particles flowing through the sensor, on the basis of their electrical properties. The passage of a single particle through one of the gaps perturbs the sensing area impedance for a few tens of milliseconds, depending on the flow rate and the particle size. Such change in impedance generates one peak over the baseline for

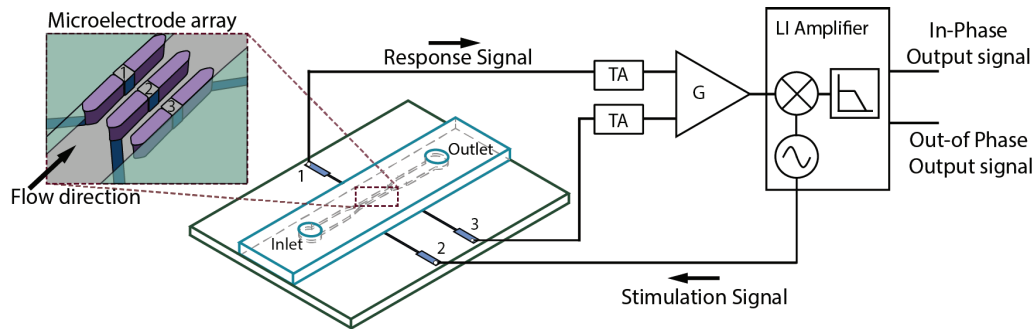


Figure 4.5: A sinusoidal voltage is applied using six simultaneous frequencies (ranging from 100 kHz to 27 MHz) to the central microelectrode ('2' in the cartoon). The current outputs from the outer microelectrodes ('1', '3') are converted to voltage by transimpedance amplifiers (TA) and then processed differentially by a lock-in amplifier. The zoomed-in detail reports a sketch of the sensor in the microfluidic channel.

each of the two components of the signal and for each single frequency.

Data were processed using a custom-written graphical user interface (GUI) coded with Matlab (R2015b, MathWorks). In order to improve the peak detection step and correct for any time-dependent drift, each signal was processed applying a wavelet-based de-noising as well as a baseline removal operation.

Peaks timestamps were determined on one component characterized by a high signal-to-noise ratio (typically the in-phase component at 6 MHz). Post data acquisition, the height and width of the peaks on each component were extracted and elaborated by the GUI to adjust automatically the detection parameters. Figure 4.6 shows a typical GUI interface used for the data processing.

4.2.3 Activation of CD8⁺ T lymphocytes and preparation of mixtures

Primary CD8⁺ T lymphocytes extracted from the spleen of laboratory mice hosted at the Ludwig Centre for Cancer Biology were purified using EasySep CD8 negative selection kits (STEMCELL Technology) according to the manufacturer's instructions. CD8⁺ cells (2 millions/ml) were stimulated with coated anti-CD3 (5 µg/ml, clone 145-2C11, eBioscience) and soluble anti-CD28 (1 µg/ml, clone 37.51, Biolegend) for 16 h.

After stimulation, cells were washed, re-suspended in FACS buffer (PBS with 3% FCS) and stained with CD8 and CD69 antibodies for 10 minutes at room temperature. The CD69 differentiation antigen is one of the earliest cell surface molecules express after the activation of T cells [168]. For this reason, the expression of CD69 is commonly used as a marker of activated T lymphocytes. Cells were then washed twice with FACS buffer and pool-sorted by FACS (Aria IIu, BD) according to the level of expression of CD69. The sorted CD69⁺ T cells were split in two and one of

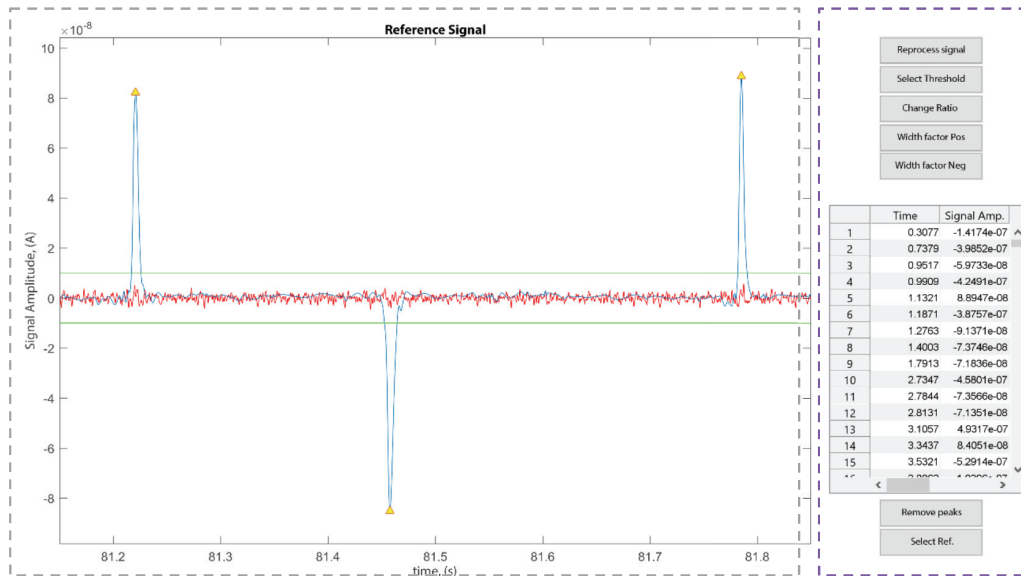


Figure 4.6: Typical GUI interface used for data processing. The signal represented in the dashed gray box (blue line) is filtered to remove noise and correct the baseline. Yellow triangles highlight the changes in the baseline which are identified as peaks. The line in green indicates the threshold for the peak detection. The noise filtered out from the signal is represented in red. The buttons on the right (violet dashed box in the figure) allow the user to change the parameters used for signal processing.

the subsets was stained with CFDA-SE (BioRad) for fluorescence imaging during the electrical measurements (Figure 4.7). These were performed approximately 24 hours from the beginning of the incubation with the antibodies.

The four cellular pools enlisted in Figure 4.7 [unstimulated T cells; non-activated CD69⁻ cells; activated CD69⁺ cells (either CFDA-SE stained or not)] as well as mixtures of CD69⁻ and fluorescent CD69⁺ cells were used for the experimental measurements. Cells were spiked with 10 μ m beads as internal reference and re-suspended in sterile-filtered PBS-Ficoll 65% (showing the same conductivity of standard PBS 1X - 15.98 mS/cm) at concentrations ranging from 300'000 cells/ml to 500.000 cells/ml. Ficoll was employed to minimize particle sedimentation at the low injection flowrates employed and to preserve the osmotic balance of the cells. Before each injection, cells in solution were re-suspended with a micropipette to guarantee sample uniformity.

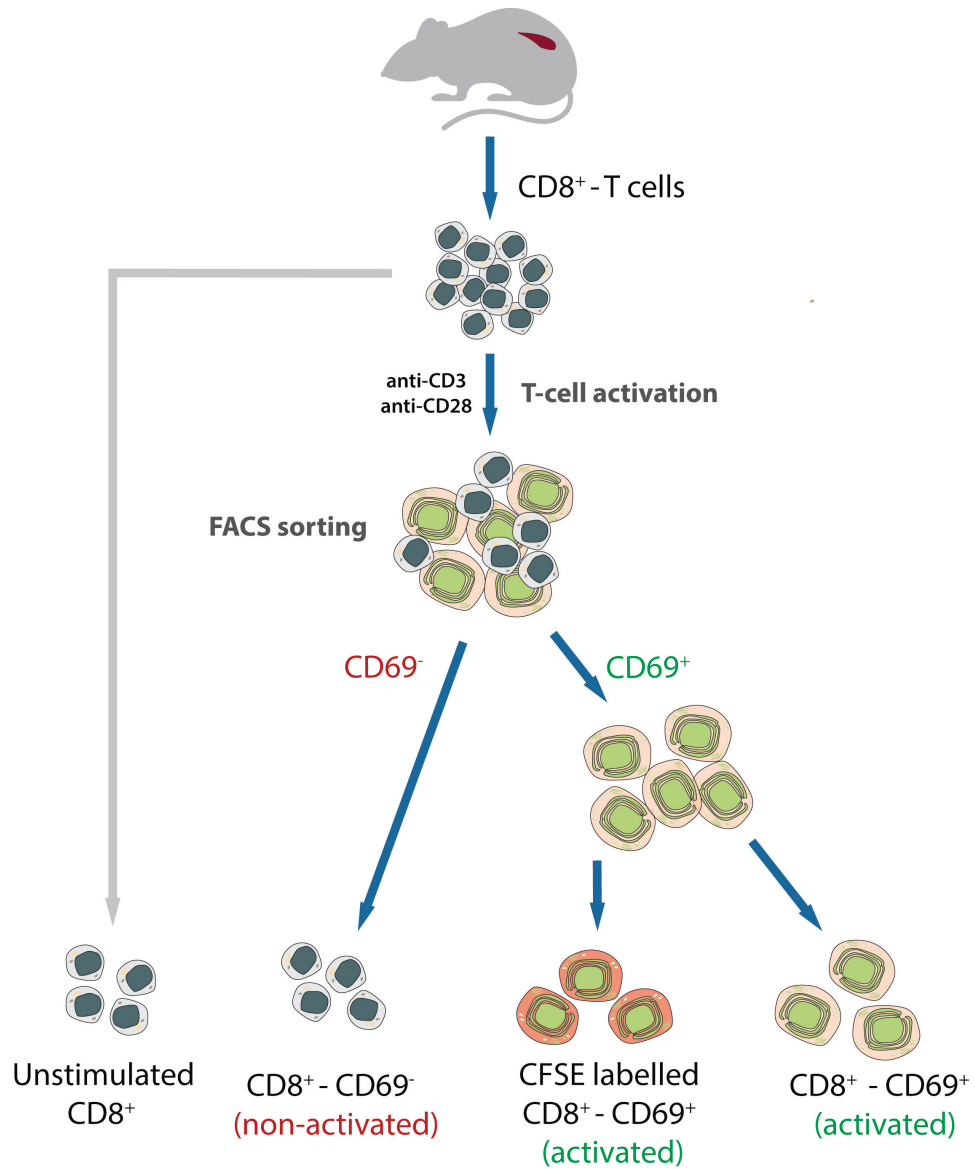


Figure 4.7: Schematic representation of the preparation of primary T lymphocytes samples. CD8⁺ T cells were purified from the spleen of laboratory animals and split in two subsets. One cell pool was activated with anti-CD3 and anti-CD28 antibodies, stained with anti-CD8 and anti-CD69 and then FACS sorted for CD69 expression. Sorted CD69⁺ cells were split in two and one of the subset was labelled with CFDA-SE for fluorescence imaging (acquired simultaneously to the electrical measurements).

4.2.1 Preparation of polystyrene beads mixtures

Commercial monodisperse polystyrene beads (Fulka, Sigma-Aldrich Chemie GmbH) with diameters of 8, 10 and 15 μm were employed. The sizes of the beads were chosen in order to match the size ranges of quiescent and activated T cells, according to optical-microscopy observations (not shown) and in agreement with what previously reported [169], [170].

Beads were diluted in a solution of sterile-filtered PBS-Ficoll 65% to a concentration of 500'000 beads/ml.

4.3 Results and discussion

Mixtures of cells and beads were injected into the chip at concentrations that limited significantly the possibility of having two cells pass simultaneously through the sensor, as verified by continuous optical observation of the sensor area. The passage of a cell through either interelectrode gates of the sensor perturbs the impedance of the volume between facing electrodes. As shown in Figure 4.8, the sign of the peak amplitude can be either positive or negative with respect to the baseline of the signal. This depends on which interelectrode gate is crossed by the particle (cell/bead) at that time, considering that the signal is acquired differentially from the two external microelectrodes.

Due to possible differences related to electrodes microfabrication, the amplitudes of opposite peaks of comparable particles might be different. For this reason, signal analysis has to be applied to individualise the analysis for the two interelectrode gates.

Being aware of possible variation of the signal due to cell characteristics, beads of 10 μm in diameter were used as reference by spiking them in cell samples. In this way, potential drifts or variations during the measurements could be monitored concomitantly to the analysis. During the experiments we noticed how such variations can be caused both by the instrument parameters (i.e. response signal is different from one combination of frequencies to the other), or by factors that perturb the sensing regions, such as minor contaminants in solution (e.g. small particles of dust) or microbubbles. To take this into account, we filtered our solutions prior to use through 0.22 μm filter and thoroughly cleaned the microchannel by ultrasonic bath in a detergent solution (typically 0.02% Tween-20 in 1X PBS) applied for few minutes. Measurement conditions can be also affected by cell debris adhering on

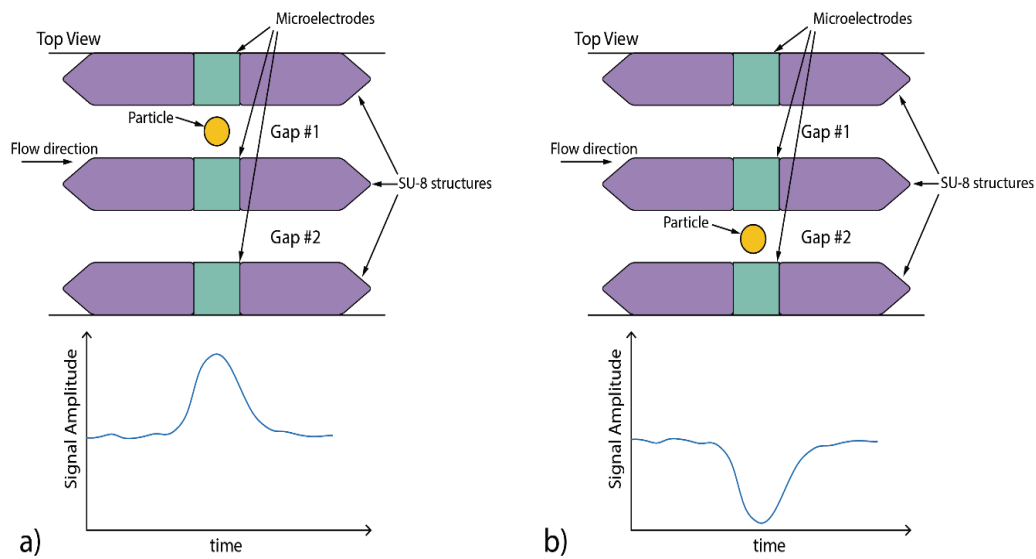


Figure 4.8: Sketch of the sensor in the microchannel (top view) and of the signal change due to the passage of a single particle (cell/bead). Due to the differential configuration, the amplitude peak assumes positive (a) or negative sign (b) respect the signal baseline, depending on the position of the particle in the sensor (Gap #1/Gap #2 in the figure).

the surfaces of the pillars. To prevent this, the channel was cleaned with 100 mM NaOH every time the syringe was loaded with a new sample (considering the average duration of a measurement session, a cleaning step of the microchannel was then performed usually every 20 min). In addition to all these precautions, all the undesired perturbation of the measurement, causing unexpected variation of the output signal, were subsequently corrected by the data processing procedure.

In the light of our experience, beads play an important role as reference to monitor and consequently correct the measurements when needed. Beads of 10 μm in diameter, bigger than cell sizes, were chosen as reference to easily distinguish their impedance signature from the cells' ones.

4.3.1 Discrimination of polystyrene particles based on their size

Electrical measurements of both homogeneous samples and mixtures of beads were performed at different frequencies. The in-phase component of the output signal of 8 μm beads for six different frequencies in the 300 kHz - 17 MHz range is shown in Figure 4.9. Peaks generated by an 8 μm bead flowing across an interelectrode gate outstand from the noise for each frequency, being 10 MHz the component with the lowest signal to noise ratio. It should be pointed out that opposite peaks are typically not symmetric. Intrinsic differences of the microelectrodes may introduce this asymmetry, which has to be taken into account during data analysis. As a consequence,

different thresholds for peak detection are necessary and for this reason, among the six frequencies employed, a reference component with high SNR is chosen, when processing data to extract the peaks. In addition, the same reference component is chosen to extract both positive and negative peaks and to reduce data processing time.

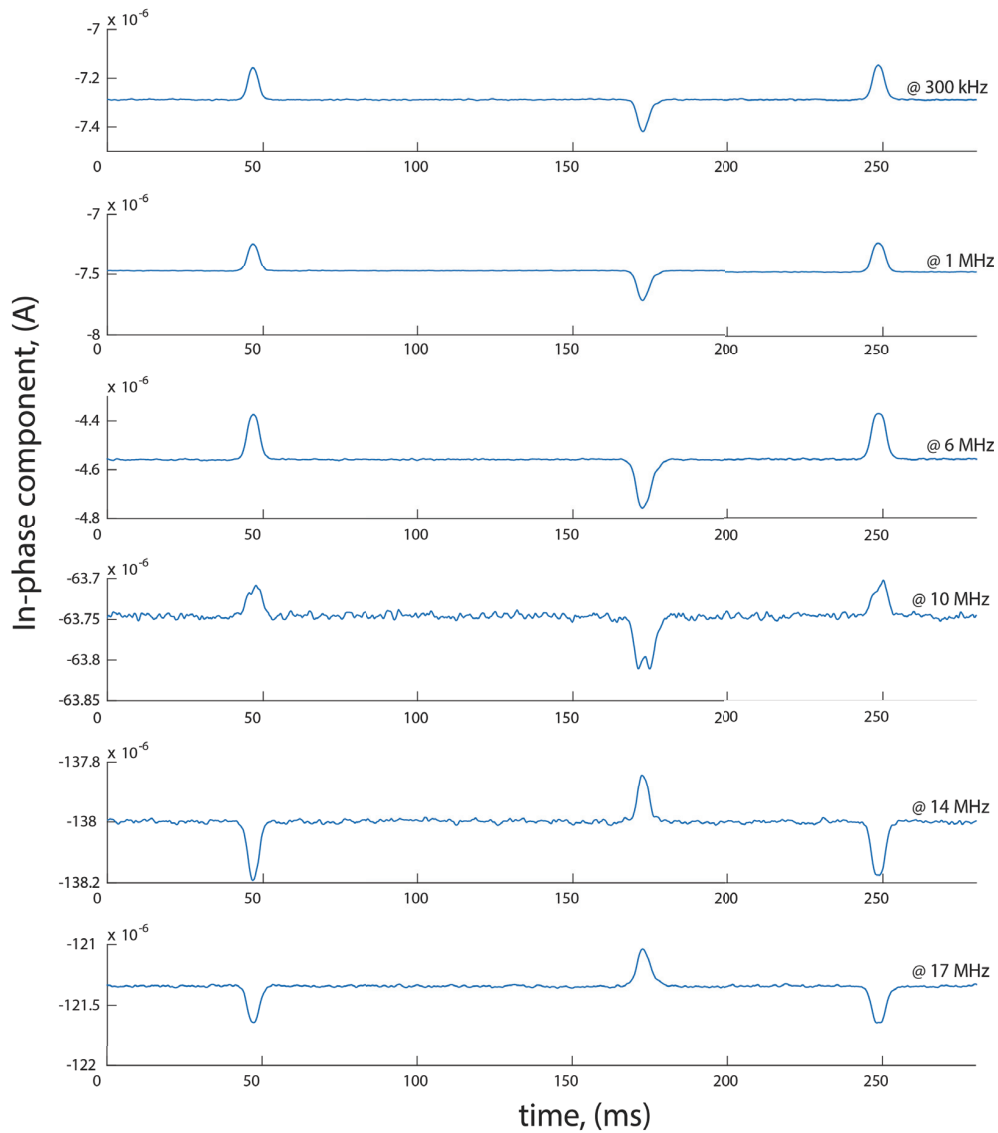


Figure 4.9: Raw in-phase component signals recorded at six different frequencies simultaneously. Peaks correspond to the passage of a single 8 μm -diameter beads in either interelectrode gaps.

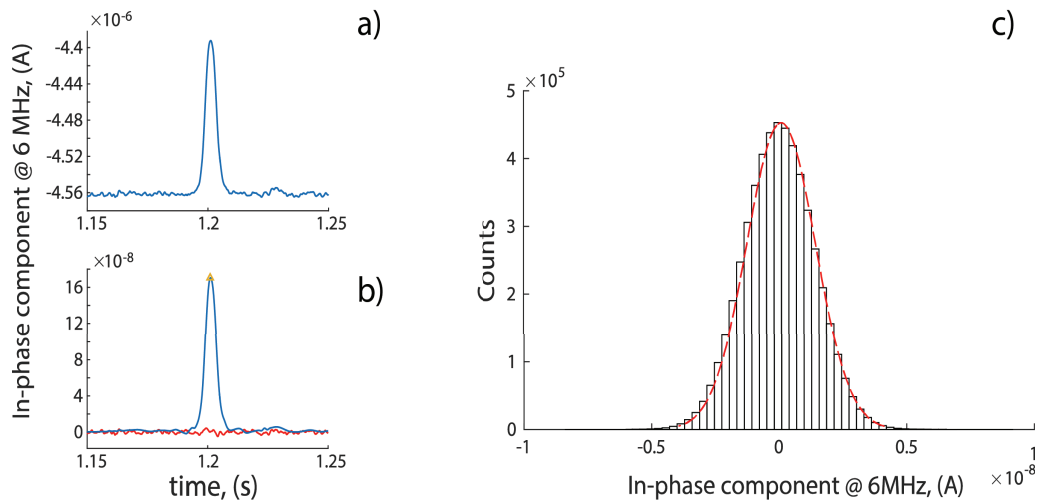


Figure 4.10: Typical signal output for an 8 μm bead before (a) and after (b) the signal processing procedure. (c) Histogram of the measurement noise extracted for the in-phase component at 6MHz. Noise distribution is fitted by a normal density function (dashed line in red).

The Matlab routine employed filters both in-phase and out-of-phase components before peak amplitude extraction. An example of data treatment of a single peak before (a) and after (b) the noise filtering and baseline removal is shown in Figure 4.10. The noise (in red in Figure 4.10b) follows a normal distribution with a standard deviation of 1.368 nA ($R^2=0.998$) (Figure 4.10c). The standard deviation of the noise is larger for higher frequencies for both in-phase and out-of-phase components (Figure 4.11a). The signal to noise ratio, calculated as the ratio of the average of the peak amplitudes for 8 μm beads and the standard deviation of the noise, is represented in Figure 4.11b. In this configuration, the best detection performance is achieved with the in-phase component at 1 MHz and both components at 6 MHz.

In order to identify the best component for discriminating beads based on their size, the variability of the signal of 8 μm beads has been analyzed for all components. As expected, the lowest CV is attained when using the highest signal-to-noise components (Figure 4.12b)

Polystyrene beads of different sizes were used to determine the performance of the system in discriminating particles based on size. Figure 4.13 shows the height of the peaks extracted for the in-phase component acquired at 6 MHz for a mixed population of 8, 10 and 15 μm diameter beads. The three subpopulations distribute differently according to their size and they can be easily distinguished. The change of the impedance signal is proportional to the particles volume as shown in Figure 4.14 and thus scales as the third power of radius ($R^2=0.9981$).

The CV of the electrical signal is approximately 4% for 8 μm diameter beads, 6% for 10 μm diameter beads and 6.9% for 15 μm diameter beads. The manufacturer

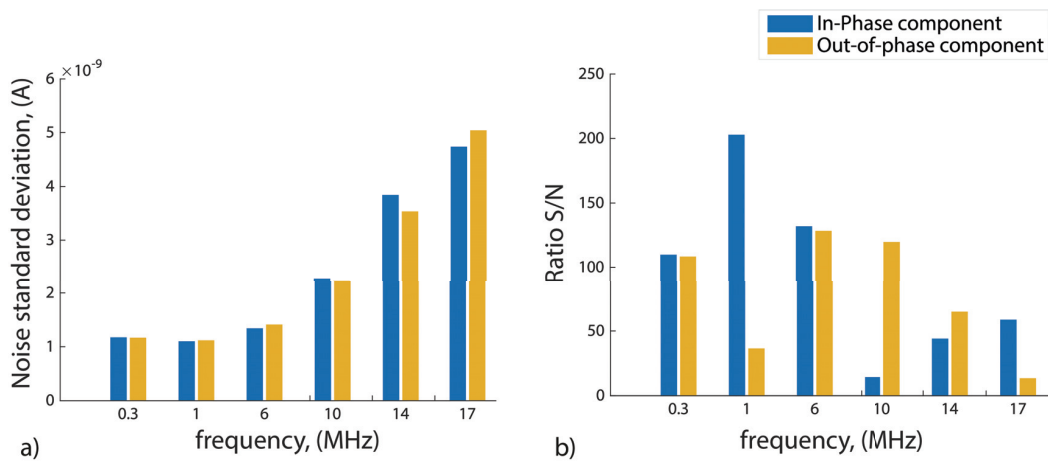


Figure 4.11: (a) Variation of noise standard deviation of the in-phase (blue) and out-of-phase component (yellow) of the output signal respect frequency. (b) Variation of the ratio between the peak amplitudes of 8 μm -diameter beads and the corresponding noise standard deviation versus frequency.

declares a CV (in diameter) of 1.13%, 1.19% and 2%, for 8 μm , 10 μm and 15 μm beads respectively. This translates into a volume CV of approximately: 3.3%, 3.6% and 6.1%. The values are summarized in Table 4.1.

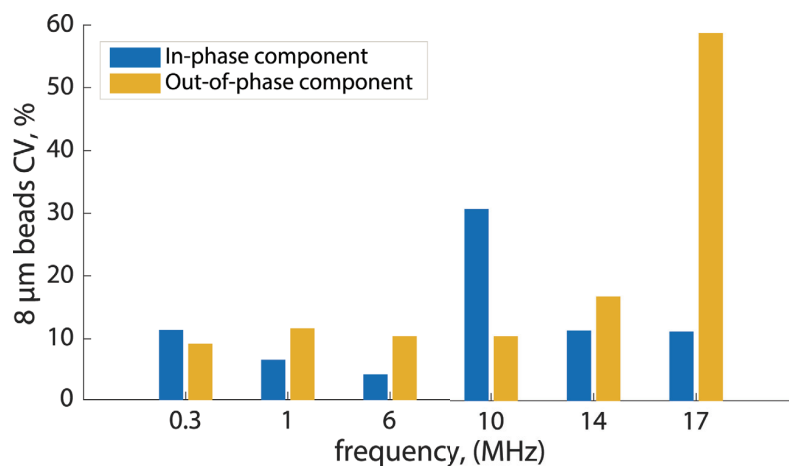


Figure 4.12: Variation of CV of the peak amplitudes of 8 μm -diameter beads evaluated for both in-phase (blue) and out-of-phase (yellow) components of the output signal recorded at six different frequencies simultaneously (more than 600 events).

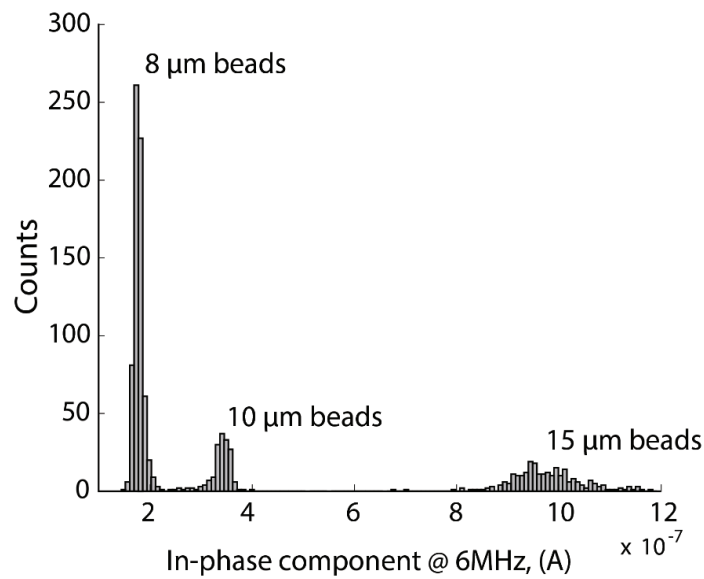


Figure 4.13: Histogram of the impedance signature of 8, 10 and 15 μm beads (668, 169 and 238 events respectively) plotted against the in-phase component recorded at 6 MHz.

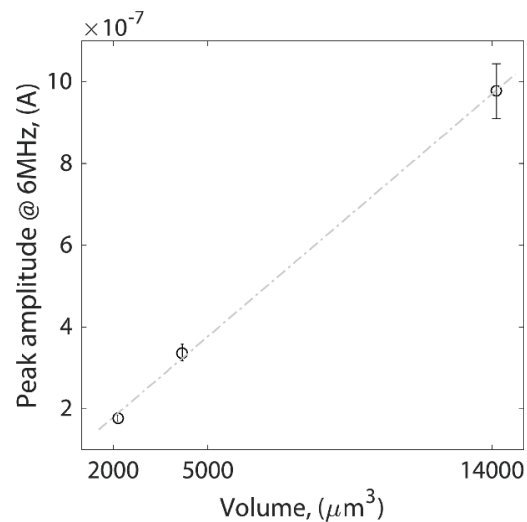


Figure 4.14: Variation of the in-phase component at 6 MHz for the mixture beads population respect their volume.

The CV of the impedance volume increases with the beads size, reflecting the volume CV. The values of CV obtained from our electrical measurements are slightly higher (in particular for the 10 μm beads) than the nominal variability of the size of the beads. It is important to observe that the events corresponding to 10 μm beads are less numerous compared to the ones of 8 μm and 15 μm , and this difference in numerosity might have affected our estimations. Despite the slight difference, the electrical measurements well approximate the

nominal values. We thus chose not to provide the device with a focusing module to position the particles in the center of the interelectrode gap. This might indeed reduce the variability of the impedance signal [171], but it would imply a more complex fluidic setup. Typical CVs of commercial Coulter counters, as reported by the manufacturers, are larger than 2% hence showing that our device has state of art performance.

Table 4.1: Values of CV of 8 μm , 10 μm and 15 μm diameter beads measured by the sensor and provided by the manufacturer.

	8 μm	10 μm	15 μm
CV of impedance signal	4%	6%	6.9%
Nominal CV	3.3%	3.6%	6.1%

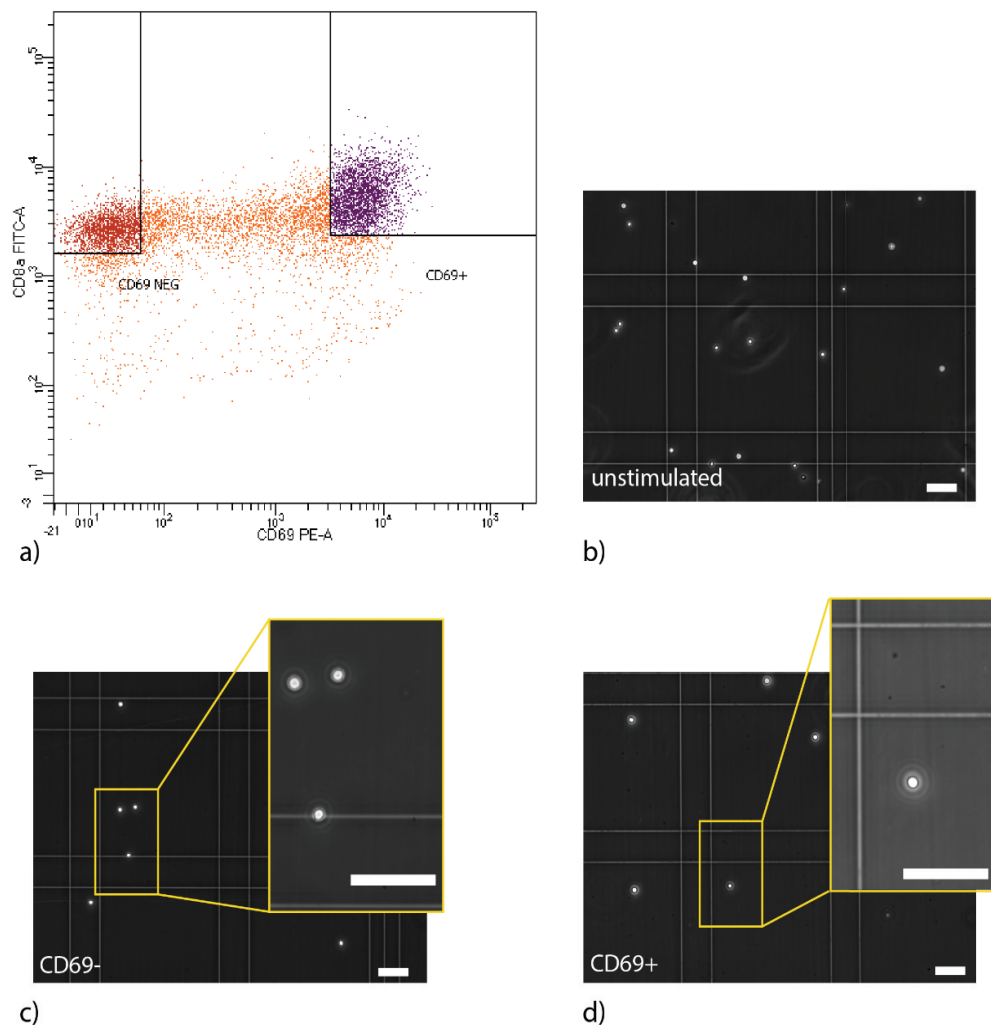


Figure 4.15: (a) FACS analysis of stimulated T lymphocytes during cell sorting. Gated CD69^- cells are represented in red and the gated CD69^+ population in violet. Optical microscope images of unstimulated (b), CD69^- (c) and of the CD69^+ cells (d) sorted by FACS. (Bar size 50 μm).

4.3.2 Cell impedance measurements

The results of FACS sorting (performed at the LCCB) are shown in Figure 4.15. The signal corresponding to the expression levels of CD69 and CD8 are represented respectively on x- and y-axis. The gating strategy to sort cells according to their CD69 expression was chosen to enrich for high CD69 expresser (assuming a marked activation of the corresponding cell pool). Microscopy inspections of the sorted groups of unstimulated, CD69⁻ and CD69⁺ cells are reported in Figure 4.15b, c and d.

Unstimulated T cells were then measured over the whole range of frequency. Figure 4.16 shows the change of electrical impedance due to the passages of single cells. The cell-induced change of the real and imaginary parts of the differential signal are represented in Figure 4.16a and Figure 4.16b respectively with error bars reporting the variability over 500 or 1790 single cell events. The impact of cells on the baseline

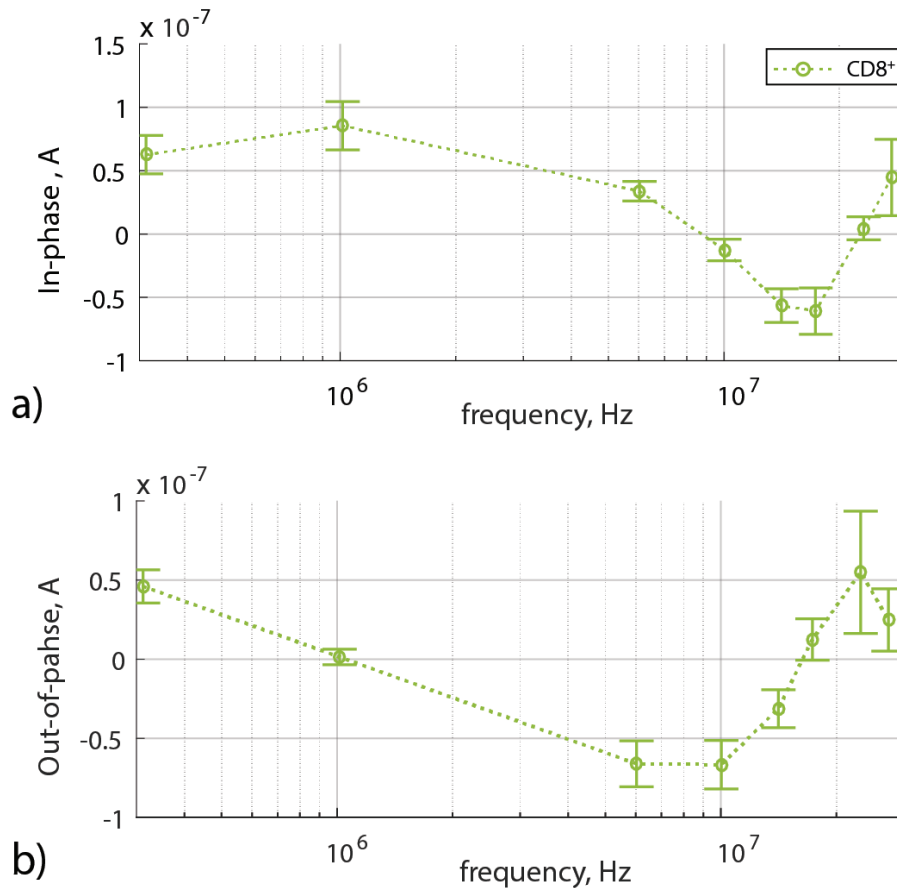


Figure 4.16: Changes of the in-phase and out-of-phase components generated by the passage of single unstimulated CD8⁺ T cells. The values are the measured peaks averaged over around 200 events or 1200 events depending on the frequency. The error bars correspond to the standard deviation of the measurements.

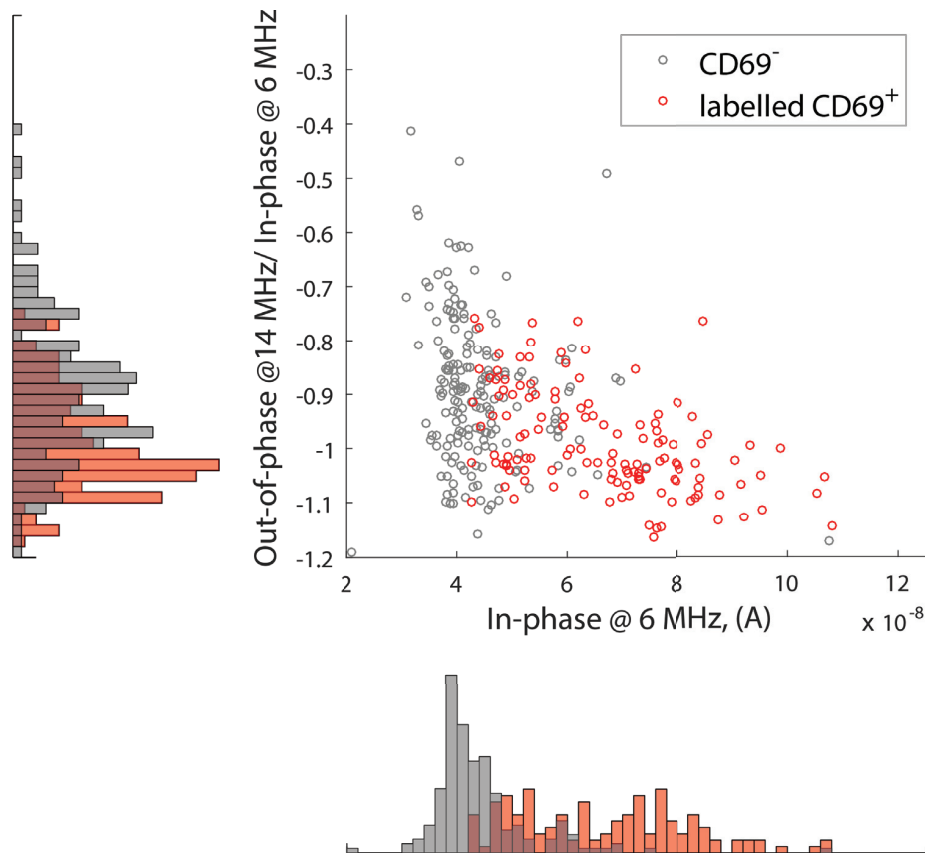


Figure 4.17: Injections of mixture of CD69⁻ (in grey, 313 events) and labelled CD69⁺ (in red, 131 events).

impedance is visible between approximately 100 kHz and 30 MHz, where both the contribution of the electrode interface capacitance at the lower frequencies (approximately $1.5 \mu\text{F}/\text{cm}^2$) and of the parasitics at higher frequencies are attenuated.

As previously mentioned, in order to observe the impedance changes induced by activated and non-activated T lymphocytes, we selected the components that maximized the signal-to-noise ratio, namely the in-phase component at 6 MHz and the out-of-phase component at 14 MHz.

These signals are represented on the scatter plots of Figure 4.17, which reports the lower frequency component on the x-axis and the ratio of the higher over lower frequency component on the y-axis. The cells of the mixture identified as activated by fluorescence are indicated with red circles on the plot.

This population experiences a marked shift on the component at 6 MHz. We assume that the major contribution to this change is the size increase of cells after mitogenic stimulation and that the spread of the response at 6 MHz relates mostly to the asynchronous re-entry in the cell cycle of activated cells upon stimulation (hence, the heterogeneity in size of the cell pool). We nevertheless cannot rule out the detection of activation-dependent membrane features, which would be visible at that very same frequency [172], [173].

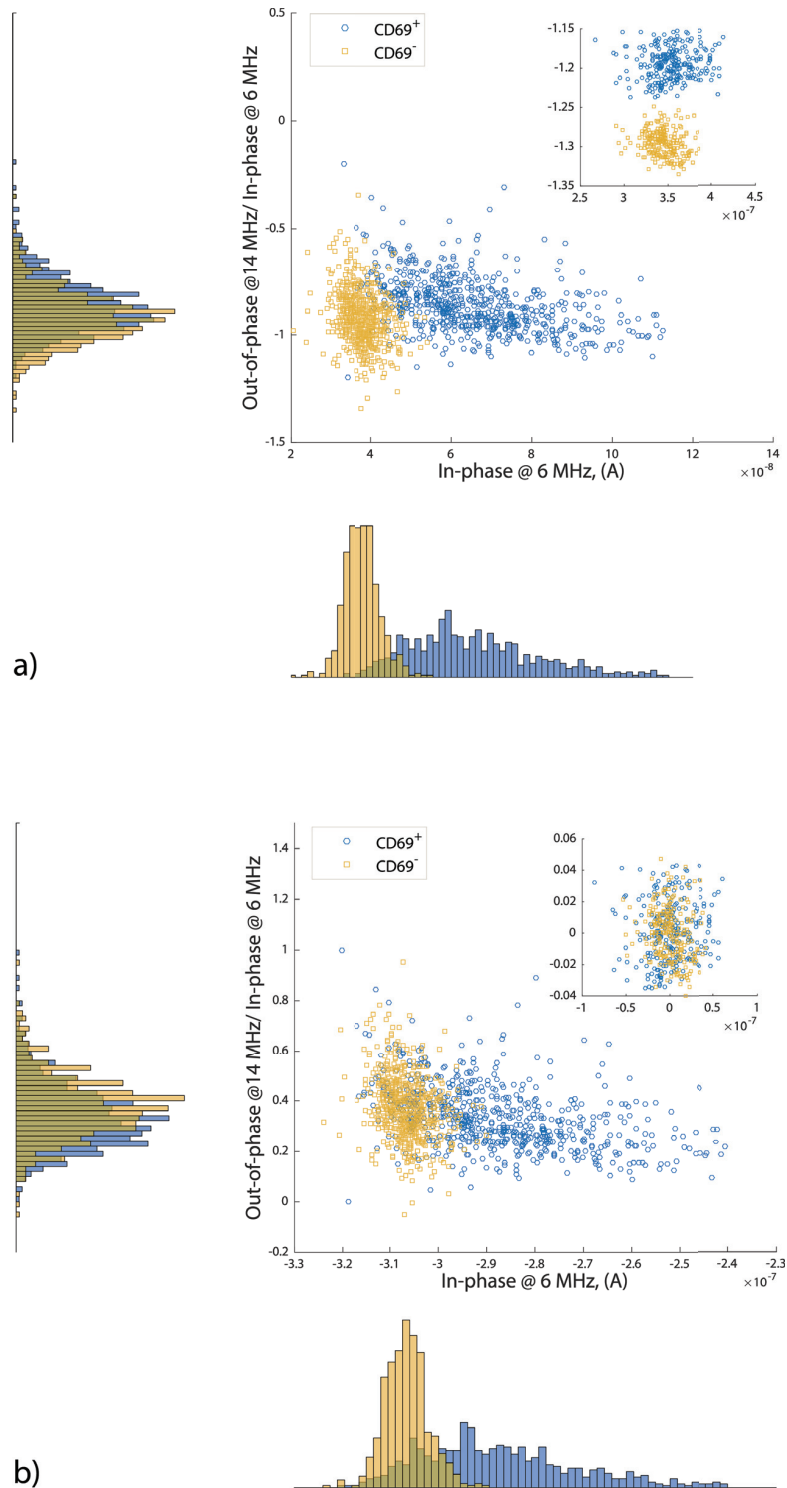


Figure 4.18: (a) Individual injections of CD69⁻ T cells / 10 μm beads mixtures and CD69⁺ T cells / 10 μm beads mixtures (yellow squares and blue circles, respectively) before correction. (b) The values of each population have been adjusted on both axes by subtracting the median value of the corresponding beads' population. The overlap of the beads populations before and upon correction is highlighted in the respective insets.

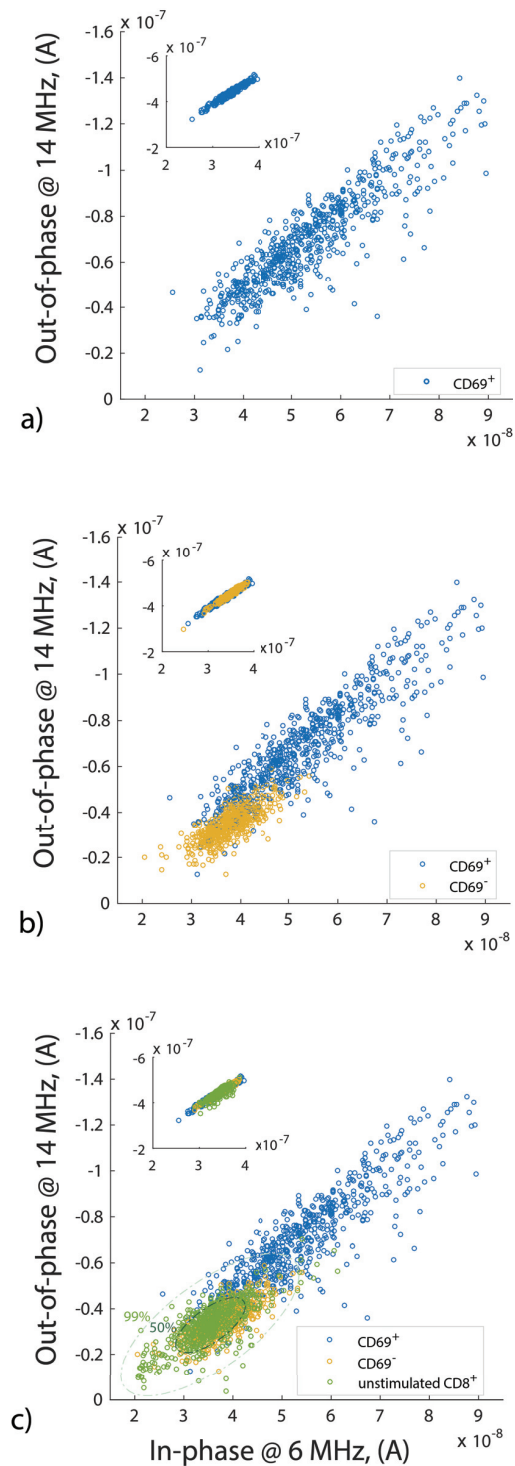


Figure 4.19: Scatter plot corresponding to the signal peaks of single cells at frequency of 6 MHz and 14 MHz for CD69⁺ cells (a), CD69⁺ and CD69⁻ cells (b) and CD69⁺, CD69⁻ and unstimulated cells (c). The peak values of CD69⁺ cells have been adjusted with respect to the beads populations. The insets highlight the overlap of the beads populations upon correction. c) The dashed line, representing the isocontour of the Gaussian distribution, allows to visualize a 2D confidence interval, showing the 50% and 99% confidence ellipses for the bivariate normally distributed data. This confidence ellipse defines the region that contains 50% (dark green) and 99% (light green) of the data.

Since the intrinsic electrical properties of cells are more evident towards higher frequency ranges, we highlight this contribution by plotting the ratio of the two components at 14 MHz and at 6 MHz (represented on the y-axis of the plot (in Figure 4.17)). This allows to appreciate a shift in the population of activated cells which is specific for the 14 MHz component. This signal could arise from cytoplasmic and membrane changes associated to activation - possibly, the remodeling of actin cytoskeleton [174] which in turn reflects on the reorganization of cell morphology [163] or the increment of nuclear volume [175]. In addition, a Student t-test was performed on the y-axis datasets, obtaining a p-value of less than 0.0001

The distribution of CD69⁻ cells over the 6 MHz component shows a smaller population of non-activated cells falling in the region where most activated cells reside. This is possibly due to CFDA-labelled activated cells that have escaped the detection through fluorescence while flowing through the sensor.

To compare the two clearly defined populations we performed injections of individual samples of CD69⁻ and CD69⁺ cells (respectively in yellow and in blue in Figure 4.18), both spiked with 10 μ m polystyrene beads to account for signal variation across different experiments. More particularly, the data points of Figure 4.18a were corrected for this variation, estimated from the signal shift of the spiked beads. The correction was obtained by subtracting the median value of the x- and y- components of the beads from the ones of the CD69⁻ and CD69⁺. Data after correction are shown in Figure 4.18b. When measuring sorted cells separately, the distribution of CD69⁻ cells shows a single peak, in support of our hypothesis on the presence of residual CD69⁺ cells that escaped the detection through fluorescence. Moreover, the shifts of the activated cells on both axes are in agreement with the previous experiment (summarised in Figure 4.17) corroborating how the staining performed on the activated cells in the mixture (Figure 4.17) cannot be accounted for the change in impedance.

The two components at 6 MHz and at 14 MHz, chosen to highlight the impedance change upon T cell activation, were used to characterize quantitatively the capability of the system to discriminate activated lymphocytes. Figure 4.19a and b show the scatter plots of CD69⁻ and CD69⁺ populations (yellow circles and blue circles, respectively). Unstimulated T cells are used as reference to set a boundary in the 2D space beyond which the cells are defined as activated (Figure 4.19c).

The boundary is determined by the confidence region that encompasses the unstimulated cells population. If considering a confidence region of 50% (Figure 4.19c – dark green dashed ellipse), our system has a sensitivity of 94% (i.e. 94% of the activated CD69⁺ cells fall within their corresponding area).

Moreover, we calculated the specificity of our detection by considering the percentage of CD69⁻ cells falling within the non-activated region (defined by the unstimulated pool), obtaining a value of 74%. Specificity reaches instead 99.66% when choosing the 99% confidence region of the non-activated pool Figure 4.19 c – light

green dashed ellipse), at the cost, though, of a much lower sensitivity (59.12%). While the system, in its current configuration, does not comply with the stringent requirements for the detection of antigen responsive T cell clones (down to $0.6 - 60$ cells over 10^6) [142] it does show that activation induces changes in individual cells, which in turn modify their electrical impedance.

The discrimination capability of the system is clearly impacted by the variability of the impedance signal of the activated lymphocyte pool, possibly due to different stages of both the cell cycle and cell activation at that time-point. Moreover, the variability of the impedance signature of activated T cells is much larger than the measurement error, which was extrapolated from tests on polystyrene beads shows above (~ 1 nA, 4.3.1). It is important to observe that the accuracy in determining cell size obtained with this sensor, is achieved despite the lack of a focusing strategy to control the position of the cell between the electrodes. It should be pointed out that, with this fabrication technology, the size of the pillars, the interelectrode distance and the height of the chamber could be reduced to achieve a 5 times larger cell-to-volume ratio [123] leading to a larger signal output. The fabrication technology presented allows to arrange a large number of sensors in the same chamber and multiple chambers on the same chip, opening the possibility to exploit the impedance signal to detect T cell activation on larger cell pools. In addition to a flow system with improved parallelism and performance, we foresee the possibility of monitoring the activation of T cells in real-time through impedance. This would require tailored sensor arrays conjugated to single-cell traps where individual T cells could be activated on chip with a strategy similar to what reported in [149] and screened for activation.

4.4 Summary

We show in this chapter the detection of activated T cells in flow through impedance, a label-free approach that circumvents some of the technical limitations typically encountered when screening T cells to employ in adoptive immunotherapy. The electrical characterization of single cells is performed in a microfabricated channel featuring vertical platinum electrodes and SU-8 microfluidic structures. The platform is obtained through a fabrication approach based on bulk micromachining on silicon that greatly improves reliability and allows to easily upscale the system for higher throughput. The possibility to display vertical-electrode features with high conductivity results in high-performance impedance microsensors that can be configured as high density arrays. Notably, conjugating impedance-based analytics with single clone segregation on chip would permit to follow in real-time - and non-

invasively - the activation of single T cells, with the potential of revealing information on the activation process and its stages.

5 | CONCLUSIONS AND FUTURE WORKS

5.1 Summary of achievements

Electrical-based techniques bear the potential to provide sensing and actuation functions to singularly addressable high-density locations on lab-on-chip devices. The realization of such concept is presently limited by the lack of a technology to obtain low-resistance free-standing electrodes and vertical electrode surfaces integrated in microfluidic structures. This thesis addresses this limitation by providing two solutions for the fabrication of highly conductive vertical platinum electrodes with high aspect-ratio that can be easily combined with microfluidic SU-8 structures.

The first process described is based on SU-8 photolithography, standard thin-film deposition and patterning techniques and allows to achieve high aspect-ratio and high density 3D electrode structures. The fabrication process and the achieved results have been published in the journal *Microelectromechanical Systems*, [124] and presented in the IEEE Engineering in Medicine and Biology Society conference (2015) [176]. Moreover, this process has been recently employed in our laboratory to achieve combined dielectrophoresis (DEP) and electrorotation (ROT) using M-17 neuroblastoma cells [177].

The second fabrication process is based on standard silicon micromachining. The cores of the 3D microelectrodes are obtained by etching silicon wafer and then passivated prior the metal deposition. The metal is sputtered and successively patterned by spray coating and dry etching. Similarly to the previous case, the process and the results of the microfabrication have been published in the journal *Sensors and Actuators B* [123] and presented in peer-reviewed conferences [178]–[180] showing the implementation of the technology for impedance-based measurements of particles and cells.

In both process, microelectrodes can be fabricated on silicon substrate and are hence CMOS-compatible enabling their implementation together with circuits. One of the major differences between the two described processes is that, in the first fabrication process, the cores of the electrodes are obtained by surface micromachining which patterns the microstructures on an additional SU-8 structural layer. Conversely, in the second fabrication process, the core structures are directly etched into the silicon wafer by bulk manufacturing, in a subtractive way. In this second case the electrodes are more robust and the process more reliable with respect to the one based on SU-8. Nevertheless, silicon structures need an electrical insulation layer. Moreover, spray coating is required to pattern planar connections, limiting the density of lines that can be obtained compared to the lift-off process.

The chips can undergo autoclave sterilization and be reused multiple times. Devices have been tested and used multiple times over many months without degrading their performances.

Recently we employed the silicon-based strategy to fabricate an impedance microfluidic cytometer used to characterize pools of in vitro activated T lymphocytes. We show, for the first time, that single activated T cells in flow can be identified by their peculiar electrical signal without the need to employ cell markers. This work originates from a collaboration with the LCCB and is inspired from the need to establish a strategy for a minimally-invasive analysis and manipulation of immune cells. These methodologies are in fact of great interest in the context of adoptive immunotherapy at the aim of reemploying characterized cells to treat patients. (Our results have been reported in a manuscript currently under review).

5.1 Future perspectives

Some of possible future investigations we outline below are currently undertaken and the preliminary results are presented.

Employment of glass substrate

SU-8-based microelectrodes could be fabricated on an insulating substrate, i.e. float glass. The use of a glass should reduce the capacitance between the electrodes and the substrate, increasing the upper frequency limit of the frequency measurement. The contribution of the parasitic capacitance in measurements is in fact determined by the thickness of the insulating layer underneath the electrodes, and by the material of the substrate itself (insulator in the case of glass or semiconductor in the case of silicon). We performed preliminary trials by fabricating metal-coated SU-8 microelectrodes with the same configuration used for the impedance-based cytometer

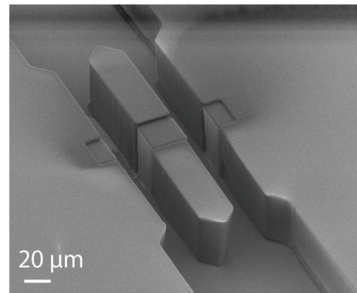


Figure 5.1: SEM picture shows SU-8-based 3D microelectrodes fabricated on a glass substrate and integrated in SU-8 microfluidic channel.

described in this work. When employing the electrodes for this application, an additional passivation step is required to insulate the planar metallic surfaces. We performed preliminary experiments with a pilot device (Figure 5.2), similarly to what shown in 4.2.1, but we encountered a main issue in the chip sealing, possibly caused by the presence of the insulating layer itself. The insulating layer poorly adheres on the glass substrate, and this affects the sealing of the microfluidic channel. Additional optimization is hence required (SiO_2 and Al_2O_3 have been tested so far). A possible strategy to overcome this issue consists in realising a holder allowing to clamp the PDMS and the chip and to screw them together.

Impedance sensor arrays

Multiple sensors featuring arrays of 3D electrodes can be fabricated in the same channel separated by SU-8 structures that would prevent the passage of cells between neighbouring sensors (see Figure 5.2). In this way, wider channels can be obtained, resulting in upscaled throughput, as well as in the reduction of pressure in the microchannel and in a reduced risk of clogging.

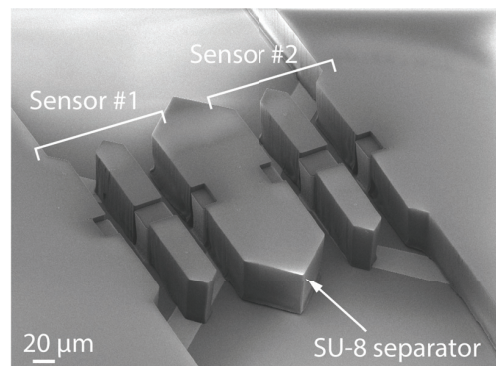


Figure 5.2: SEM picture of multiple sensors in a single microfluidic channel. The SU-8 separator prevent cells flowing through the interelectrode gap of the two different sensors.

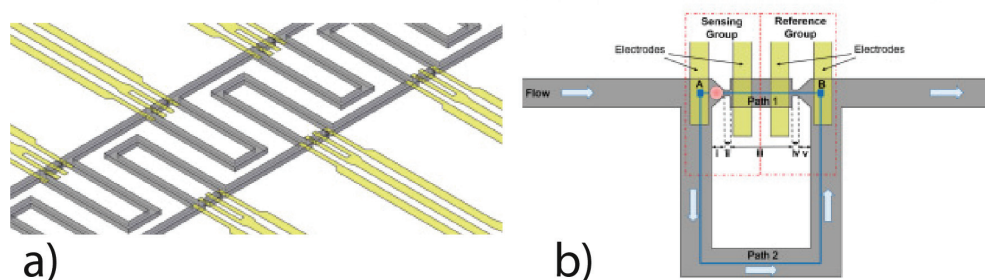


Figure 5.3: (a) Schematic of the microfluidic device featuring integrated coplanar electrodes (in yellow). (b) Schematic of a close up view of a single trapping site combined with the sensing electrodes.

Application in adoptive immunotherapy

As already discussed in 4.3.2, the detection of antigen-specific T cells has stringent requirements, due to their low frequency in the sample, that cannot be satisfied by the current system configuration. To overcome this limitation, we foresee a new device that features an array of sensing sites integrated in single-cell traps to monitor in real-time the activation of single T cells through impedance measurements.

Different published works already report on microfluidic platforms to assess single-cell impedance [181]–[187], but each proposed solution employs coplanar electrodes, hence presenting the drawbacks already discussed in 1.3.1. On the basis of these works, we are currently developing a platform featuring trapping sites conjugated with vertical electrodes to monitor the impedance response in real-time. The electrodes we envision could be used to individually release or treat (i.e. induce cell lysis) the trapped cells by applying appropriate electric field. In addition, vertical electrodes and a transparent cover would allow to couple the impedance measurements with microscopy to monitor cell morphological changes or signalling (i.e. calcium dynamics thorough fluorescent dyes [155]).

The design and fabrication of this platform have been recently undertaken. On the basis of the hydrodynamic trapping concept proposed by Tan and Takeuchi in [188], we performed numerical simulations (not shown here) to optimize the design parameters of the microfluidic traps tailored for our application. The schematic of the design of a single-cell trap including the vertical electrodes is shown in Figure 5.4a. An analogous scheme for cell trapping have been lately developed also by Zhou et al. [186] Their solution combined the trap with coplanar electrodes to monitor single cell lysis through impedance (Figure 5.3).

Recently, we succeeded in the fabrication of the vertical electrodes integrated into single-cell traps, employing respectively the processes described in 2.1.1 and in 2.1.3 (Figure 5.4b and c).

We foresee further experiments to characterize the device using polystyrene beads

and successively challenging it with measurements on T cells. We foresee to further extend the analysis by integrating the monitoring of cell impedance with the actual activation of cellular clones directly on chip. We will proceed along this line by defining, in first instance, the protocol for the activation of the T cells directly on chip.

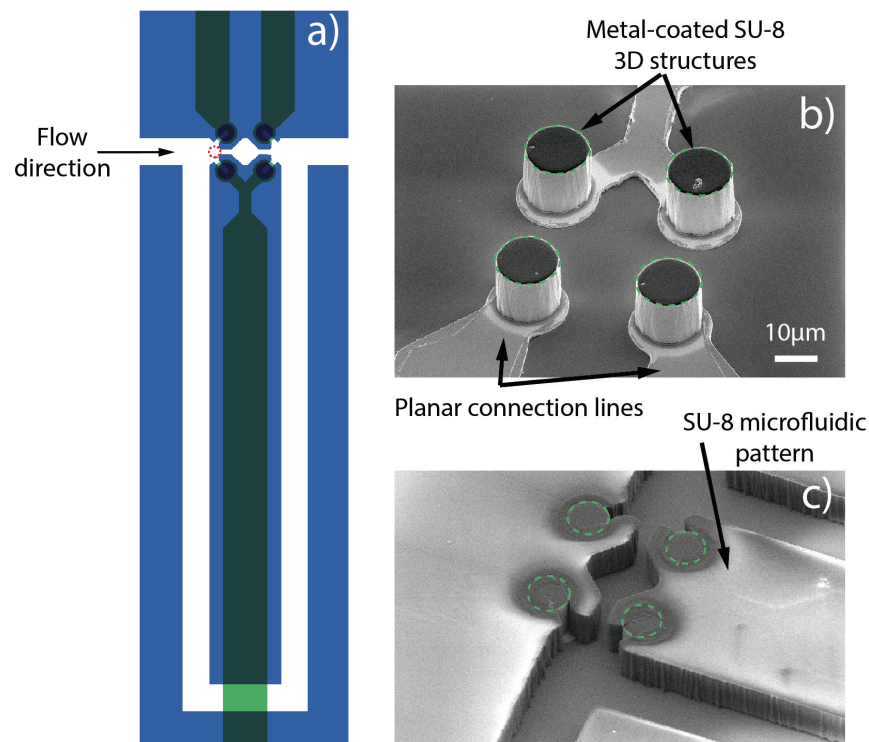


Figure 5.4: (a) Schematic top view of the trap sites. The red dashed circles indicate the position that would be occupied by a cell in the trap sites between two round-shape pillars. According to direction of the flow one trap would be occupied by a cell and the other would remain empty, working as reference. The metal connections are represented in green and are partially buried by the SU-8 microfluidic pattern represented in blue. The microchannel is represented in white. According to the design proposed by Tan et al., when the trap is empty the flow resistance in the short channel is lower than that one in the loop channel. Therefore, a cell in the microchannel is carried into the trap if it is empty, while it is carried in the loop channel if the trap is filled. (b) SEM image of four round-shape pillars. The green circles indicate the top edge of the metal-coated SU-8 micropillars. (c) SEM image of the four round-shape pillars incorporated into the SU-8 microfluidic pattern. The green circles indicate the top edge of the metal-coated SU-8 micropillars.

REFERENCES

- [1] Jean Berthier and Pascal Silberzan, *Microfluidics for Biotechnology*. Artech House, 2010.
- [2] D. Mark, F. von Stetten, and R. Zengerle, “Microfluidic Apps for off-the-shelf instruments,” *Lab. Chip*, vol. 12, no. 14, pp. 2464–2468, Jul. 2012.
- [3] G. M. Whitesides, “Cool, or simple and cheap? Why not both?,” *Lab Chip*, vol. 13, no. 1, pp. 11–13, 2013.
- [4] Oliver Geschke, Henning Klank, and Pieter Telleman, *Microsystem Engineering of Lab-on-a-chip Devices*. Wiley, 2006.
- [5] Y. Temiz, R. D. Lovchik, G. V. Kaigala, and E. Delamarche, “Lab-on-a-chip devices: How to close and plug the lab?,” *Microelectron. Eng.*, vol. 132, pp. 156–175, Jan. 2015.
- [6] D. J. Harrison, K. Fluri, K. Seiler, Z. Fan, C. S. Effenhauser, and A. Manz, “Micromachining a miniaturized capillary electrophoresis-based chemical analysis system on a chip,” *Science*, vol. 261, no. 5123, pp. 895–897, Aug. 1993.
- [7] S. Liu, Y. Shi, W. W. Ja, and R. A. Mathies, “Optimization of High-Speed DNA Sequencing on Microfabricated Capillary Electrophoresis Channels,” *Anal. Chem.*, vol. 71, no. 3, pp. 566–573, Feb. 1999.
- [8] H. Andersson and A. van den Berg, “Microfluidic devices for cellomics: a review,” *Sens. Actuators B Chem.*, vol. 92, no. 3, pp. 315–325, Jul. 2003.
- [9] E. W. K. Young and D. J. Beebe, “Fundamentals of microfluidic cell culture in controlled microenvironments,” *Chem. Soc. Rev.*, vol. 39, no. 3, pp. 1036–1048, Mar. 2010.
- [10] C. W. Shields, C. D. Reyes, and G. P. López, “Microfluidic Cell Sorting: A Review of the Advances in the Separation of Cells from Debulking to Rare Cell Isolation,” *Lab. Chip*, vol. 15, no. 5, pp. 1230–1249, Feb. 2015.
- [11] J. El-Ali, P. K. Sorger, and K. F. Jensen, “Cells on chips,” *Nature*, vol. 442, no. 7101, pp. 403–411, Jul. 2006.
- [12] “Single cells or large populations?,” *Lab. Chip*, vol. 7, no. 5, pp. 544–546, May 2007.

- [13] J. Seidl, R. Knuechel, and L. A. Kunz-Schughart, "Evaluation of membrane physiology following fluorescence activated or magnetic cell separation," *Cytometry*, vol. 36, no. 2, pp. 102–111, Jun. 1999.
- [14] J. R. Macdonald, "Impedance spectroscopy," *Ann. Biomed. Eng.*, vol. 20, no. 3, pp. 289–305, 1992.
- [15] J. R. Macdonald, *Impedance Spectroscopy, Theory Experiment and Applications*. .
- [16] Vadim F. Lvovich, *Impedance Spectroscopy: Applications to Electrochemical and Dielectric Phenomena*, 2012th ed. Wiley.
- [17] J. S. Daniels and N. Pourmand, "Label-Free Impedance Biosensors: Opportunities and Challenges," *Electroanalysis*, vol. 19, no. 12, pp. 1239–1257, May 2007.
- [18] Fritz Scholz, *Electroanalytical Methods: Guide to Experiments and Applications*. Springer.
- [19] L. L. Zhang and X. S. Zhao, "Carbon-based materials as supercapacitor electrodes," *Chem. Soc. Rev.*, vol. 38, no. 9, p. 2520, 2009.
- [20] H. Morgan, T. Sun, D. Holmes, S. Gawad, and N. G. Green, "Single cell dielectric spectroscopy," *J. Phys. Appl. Phys.*, vol. 40, no. 1, p. 61, 2007.
- [21] S. Zheng, M. Liu, and Y.-C. Tai, "Micro coulter counters with platinum black electroplated electrodes for human blood cell sensing," *Biomed. Microdevices*, vol. 10, no. 2, pp. 221–231, Apr. 2008.
- [22] S. Gawad, L. Schild, and P. Renaud, "Micromachined impedance spectroscopy flow cytometer for cell analysis and particle sizing," *Lab. Chip*, vol. 1, no. 1, pp. 76–82, Jan. 2001.
- [23] K. Asami, "Characterization of biological cells by dielectric spectroscopy," *J. Non-Cryst. Solids*, vol. 305, no. 1–3, pp. 268–277, Jul. 2002.
- [24] James Clerk Maxwell, *A Treatise on Electricity and Magnetism*. 1873.
- [25] R. Pethig and D. B. Kell, "The passive electrical properties of biological systems: their significance in physiology, biophysics and biotechnology," *Phys. Med. Biol.*, vol. 32, no. 8, p. 933, 1987.
- [26] H. P. Schwan, "Electrical properties of tissue and cell suspensions," *Adv. Biol. Med. Phys.*, vol. 5, pp. 147–209, 1957.
- [27] K. Asami, Y. Takahashi, and S. Takashima, "Dielectric properties of mouse lymphocytes and erythrocytes," *Biochim. Biophys. Acta*, vol. 1010, no. 1, pp. 49–55, Jan. 1989.
- [28] H. G. L. Coster, T. C. Chilcott, and A. C. F. Coster, "Impedance spectroscopy of interfaces, membranes and ultrastructures," *Bioelectrochem. Bioenerg.*, vol. 40, no. 2, pp. 79–98, Aug. 1996.

- [29] Marco Di Berardino, "Electrical Detection in Microfluidic Flow Cytometers," in *The Microflow Cytometer*, 0 vols., Pan Stanford Publishing, 2010.
- [30] R. A. Hoffman, T. S. Johnson, and W. B. Britt, "Flow cytometric electronic direct current volume and radiofrequency impedance measurements of single cells and particles," *Cytometry*, vol. 1, no. 6, pp. 377–384, May 1981.
- [31] S. Gawad, K. Cheung, U. Seger, A. Bertsch, and P. Renaud, "Dielectric spectroscopy in a micromachined flow cytometer: theoretical and practical considerations," *Lab. Chip*, vol. 4, no. 3, pp. 241–251, Jun. 2004.
- [32] K. Cheung, S. Gawad, and P. Renaud, "Impedance spectroscopy flow cytometry: On-chip label-free cell differentiation," *Cytometry A*, vol. 65A, no. 2, pp. 124–132, Jun. 2005.
- [33] T. Sun, S. Gawad, N. G. Green, and H. Morgan, "Dielectric spectroscopy of single cells: time domain analysis using Maxwell's mixture equation," *J. Phys. Appl. Phys.*, vol. 40, no. 1, p. 1, 2007.
- [34] P. Gascoyne, C. Mahidol, M. Ruchirawat, J. Satayavivad, P. Watcharasit, and F. F. Becker, "Microsample preparation by dielectrophoresis: isolation of malaria," *Lab. Chip*, vol. 2, no. 2, p. 70, 2002.
- [35] S. C. Bürgel, C. Escobedo, N. Haandbæk, and A. Hierlemann, "On-chip electroporation and impedance spectroscopy of single-cells," *Sens. Actuators B Chem.*, vol. 210, pp. 82–90, Apr. 2015.
- [36] V. Raicu, G. Raicu, and G. Turcu, "Dielectric properties of yeast cells as simulated by the two-shell model," *Biochim. Biophys. Acta BBA - Bioenerg.*, vol. 1274, no. 3, pp. 143–148, Jun. 1996.
- [37] K. Asami, T. Hanai, and N. Koizumi, "Dielectric analysis of Escherichia coli suspensions in the light of the theory of interfacial polarization," *Biophys. J.*, vol. 31, no. 2, pp. 215–228, Aug. 1980.
- [38] R. Höber, "Eine Methode, die elektrische Leitfähigkeit im Innern von Zellen zu messen," *Pflüg. Arch. Für Gesamte Physiol. Menschen Tiere*, vol. 133, no. 4–6, pp. 237–253, 1910.
- [39] Hugo Fricke, and Howard, Curtis J., "Electric Impedance of Suspensions of Leucocytes," *Nature*, vol. 135, no. 436–436, 1935.
- [40] H. Fricke, "The Electric Impedance of Suspensions of Biological Cells," *Cold Spring Harb. Symp. Quant. Biol.*, vol. 1, pp. 117–124, Jan. 1933.
- [41] H. Fricke and H. J. Curtis, "The Electric Impedance of Hemolyzed Suspensions of Mammalian Erythrocytes," *J. Gen. Physiol.*, vol. 18, no. 6, pp. 821–836, Jul. 1935.
- [42] K. S. Cole and H. J. Curtis, "ELECTRIC IMPEDANCE OF SINGLE MARINE EGGS," *J. Gen. Physiol.*, vol. 21, no. 5, pp. 591–599, May 1938.

- [43] K. S. Cole and R. H. Cole, "ELECTRIC IMPEDANCE OF ASTERIAS EGGS," *J. Gen. Physiol.*, vol. 19, no. 4, pp. 609–623, Mar. 1936.
- [44] K. S. Cole, "ELECTRIC IMPEDANCE OF SUSPENSIONS OF SPHERES," *J. Gen. Physiol.*, vol. 12, no. 1, pp. 29–36, Sep. 1928.
- [45] K. S. Cole, "ELECTRIC IMPEDANCE OF SUSPENSIONS OF ARBACIA EGGS," *J. Gen. Physiol.*, vol. 12, no. 1, pp. 37–54, Sep. 1928.
- [46] I. Giaever and C. R. Keese, "Monitoring fibroblast behavior in tissue culture with an applied electric field," *Proc. Natl. Acad. Sci. U. S. A.*, vol. 81, no. 12, pp. 3761–3764, Jun. 1984.
- [47] I. Giaever and C. R. Keese, "A morphological biosensor for mammalian cells," *Nature*, vol. 366, no. 6455, pp. 591–592, Dec. 1993.
- [48] I. Giaever and C. R. Keese, "Use of electric fields to monitor the dynamical aspect of cell behavior in tissue culture," *IEEE Trans. Biomed. Eng.*, vol. 33, no. 2, pp. 242–247, Feb. 1986.
- [49] I. Giaever and C. R. Keese, "Micromotion of mammalian cells measured electrically," *Proc. Natl. Acad. Sci. U. S. A.*, vol. 88, no. 17, pp. 7896–7900, Sep. 1991.
- [50] R. Ehret, W. Baumann, M. Brischwein, A. Schwinde, K. Stegbauer, and B. Wolf, "Monitoring of cellular behaviour by impedance measurements on interdigitated electrode structures," *Biosens. Bioelectron.*, vol. 12, no. 1, pp. 29–41, 1997.
- [51] Z. Zou, S. Lee, and C. H. Ahn, "A Polymer Microfluidic Chip With Interdigitated Electrodes Arrays for Simultaneous Dielectrophoretic Manipulation and Impedimetric Detection of Microparticles," *IEEE Sens. J.*, vol. 8, no. 5, pp. 527–535, May 2008.
- [52] B. Eker, R. Meissner, A. Bertsch, K. Mehta, and P. Renaud, "Label-free recognition of drug resistance via impedimetric screening of breast cancer cells," *PloS One*, vol. 8, no. 3, p. e57423, 2013.
- [53] F. Asphahani, K. Wang, M. Thein, O. Veiseh, S. Yung, J. Xu, and M. Zhang, "Single-cell bioelectrical impedance platform for monitoring cellular response to drug treatment," *Phys. Biol.*, vol. 8, no. 1, p. 15006, Feb. 2011.
- [54] M. Thakur, K. Mergel, A. Weng, S. Frech, R. Gilabert-Oriol, D. Bachran, M. F. Melzig, and H. Fuchs, "Real time monitoring of the cell viability during treatment with tumor-targeted toxins and saponins using impedance measurement," *Biosens. Bioelectron.*, vol. 35, no. 1, pp. 503–506, May 2012.
- [55] F. Liu, T. Chen, X. Zhang, F. Li, and I. Voiculescu, "Study of Long Term Viability of Endothelial Cells on Biochip for Rapid and Reliable Water Toxicity Measurements," p. V001T02A002, Feb. 2013.
- [56] J. Wegener, C. R. Keese, and I. Giaever, "Electric cell-substrate impedance sens-

- ing (ECIS) as a noninvasive means to monitor the kinetics of cell spreading to artificial surfaces,” *Exp. Cell Res.*, vol. 259, no. 1, pp. 158–166, Aug. 2000.
- [57] W. J. Ashby and A. Zijlstra, “Established and Novel Methods of Interrogating Two-Dimensional Cell Migration,” *Integr. Biol. Quant. Biosci. Nano Macro*, vol. 4, no. 11, pp. 1338–1350, Nov. 2012.
- [58] L. Wang, J. Zhu, C. Deng, W. Xing, and J. Cheng, “An automatic and quantitative on-chip cell migration assay using self-assembled monolayers combined with real-time cellular impedance sensing,” *Lab. Chip*, vol. 8, no. 6, pp. 872–878, May 2008.
- [59] C. R. Keese, N. Karra, B. Dillon, A. M. Goldberg, and I. Giaever, “Cell-substratum interactions as a predictor of cytotoxicity,” *ResearchGate*, vol. 11, no. 2, pp. 183–192, Jun. 1998.
- [60] R. Meissner, B. Eker, H. Kasi, A. Bertsch, and P. Renaud, “Distinguishing drug-induced minor morphological changes from major cellular damage via label-free impedimetric toxicity screening,” *Lab. Chip*, vol. 11, no. 14, pp. 2352–2361, Jun. 2011.
- [61] S. Arndt, J. Seebach, K. Psathaki, H.-J. Galla, and J. Wegener, “Bioelectrical impedance assay to monitor changes in cell shape during apoptosis,” *Biosens. Bioelectron.*, vol. 19, no. 6, pp. 583–594, Jan. 2004.
- [62] Y. Qiu, R. Liao, and X. Zhang, “Impedance-Based Monitoring of Ongoing Cardiomyocyte Death Induced by Tumor Necrosis Factor- α ,” *Biophys. J.*, vol. 96, no. 5, pp. 1985–1991, Mar. 2009.
- [63] T. B. Tran, C. Baek, and J. Min, “Electric Cell-Substrate Impedance Sensing (ECIS) with Microelectrode Arrays for Investigation of Cancer Cell – Fibroblasts Interaction,” *PLoS ONE*, vol. 11, no. 4, Apr. 2016.
- [64] C. M. Lo, C. R. Keese, and I. Giaever, “Impedance analysis of MDCK cells measured by electric cell-substrate impedance sensing,” *Biophys. J.*, vol. 69, no. 6, pp. 2800–2807, Dec. 1995.
- [65] L. Wang, L. Wang, H. Yin, W. Xing, Z. Yu, M. Guo, and J. Cheng, “Real-time, label-free monitoring of the cell cycle with a cellular impedance sensing chip,” *Biosens. Bioelectron.*, vol. 25, no. 5, pp. 990–995, Jan. 2010.
- [66] C. Bird and S. Kirstein, “Real-time, label-free monitoring of cellular invasion and migration with the xCELLigence system,” *Nat. Methods*, vol. 6, no. 8, 2009.
- [67] Coulter Wallace H, “Means for counting particles suspended in a fluid.”
- [68] R. W. DeBlois and C. P. Bean, “Counting and Sizing of Submicron Particles by the Resistive Pulse Technique,” *Rev. Sci. Instrum.*, vol. 41, no. 7, pp. 909–916, Jul. 1970.
- [69] U. D. Larsen, G. Blankenstein, and J. Branebjerg, “Microchip Coulter particle counter,” in , *1997 International Conference on Solid State Sensors and Actuators*,

1997. *TRANSDUCERS '97 Chicago*, 1997, vol. 2, pp. 1319–1322 vol.2.

[70] M. Koch, A. G. R. Evans, and A. Brunnschweiler, “Design and fabrication of a micromachined Coulter counter,” *J. Micromechanics Microengineering*, vol. 9, no. 2, p. 159, 1999.

[71] D. Satake, H. Ebi, N. Oku, K. Matsuda, H. Takao, M. Ashiki, and M. Ishida, “A sensor for blood cell counter using MEMS technology,” *Sens. Actuators B Chem.*, vol. 83, no. 1–3, pp. 77–81, Mar. 2002.

[72] O. A. Saleh and L. L. Sohn, “Quantitative sensing of nanoscale colloids using a microchip Coulter counter,” *Rev. Sci. Instrum.*, vol. 72, no. 12, pp. 4449–4451, Dec. 2001.

[73] O. A. Saleh and L. L. Sohn, “Direct detection of antibody–antigen binding using an on-chip artificial pore,” *Proc. Natl. Acad. Sci.*, vol. 100, no. 3, pp. 820–824, Apr. 2003.

[74] J. J. Kasianowicz, E. Brandin, D. Branton, and D. W. Deamer, “Characterization of individual polynucleotide molecules using a membrane channel,” *Proc. Natl. Acad. Sci.*, vol. 93, no. 24, pp. 13770–13773, Nov. 1996.

[75] M. Langecker, D. Pedone, F. C. Simmel, and U. Rant, “Electrophoretic Time-of-Flight Measurements of Single DNA Molecules with Two Stacked Nanopores,” *Nano Lett.*, vol. 11, no. 11, pp. 5002–5007, Nov. 2011.

[76] R. W. DeBlois and R. K. Wesley, “Sizes and concentrations of several type C oncornaviruses and bacteriophage T2 by the resistive-pulse technique,” *J. Virol.*, vol. 23, no. 2, pp. 227–233, Jan. 1977.

[77] J. Zhe, A. Jagtiani, P. Dutta, J. Hu, and J. Carletta, “A micromachined high throughput Coulter counter for bioparticle detection and counting,” *J. Micromechanics Microengineering*, vol. 17, no. 2, p. 304, 2007.

[78] J. H. Nieuwenhuis, F. Kohl, J. Bastemeijer, P. M. Sarro, and M. J. Vellekoop, “Integrated Coulter counter based on 2-dimensional liquid aperture control,” *Sens. Actuators B Chem.*, vol. 102, no. 1, pp. 44–50, Sep. 2004.

[79] R. Rodriguez-Trujillo, O. Castillo-Fernandez, M. Garrido, M. Arundell, A. Valencia, and G. Gomila, “High-speed particle detection in a micro-Coulter counter with two-dimensional adjustable aperture,” *Biosens. Bioelectron.*, vol. 24, no. 2, pp. 290–296, Oct. 2008.

[80] A. V. Jagtiani, J. Zhe, J. Hu, and J. Carletta, “Detection and counting of micro-scale particles and pollen using a multi-aperture Coulter counter,” *Meas. Sci. Technol.*, vol. 17, no. 7, p. 1706, 2006.

[81] A. V. Jagtiani, R. Sawant, and J. Zhe, “A label-free high throughput resistive-pulse sensor for simultaneous differentiation and measurement of multiple particle-laden analytes,” *J. Micromechanics Microengineering*, vol. 16, no. 8, p. 1530, 2006.

- [82] W. Hasenkamp, G. Mernier, N. Piacentini, and P. Renaud, "Multiple-frequency impedance measurements in continuous flow for automated evaluation of yeast cell lysis," *Sens. Actuators B Chem.*, vol. 170, pp. 2–6, Jul. 2012.
- [83] G. Mernier, N. Piacentini, R. Tornay, N. Buffi, and P. Renaud, "Cell viability assessment by flow cytometry using yeast as cell model," *Sens. Actuators B Chem.*, vol. 154, no. 2, pp. 160–163, Jun. 2011.
- [84] H. Morgan, D. Holmes, and N. G. Green, "High speed simultaneous single particle impedance and fluorescence analysis on a chip," *Curr. Appl. Phys.*, vol. 6, no. 3, pp. 367–370, Jun. 2006.
- [85] D. K. Wood, G. B. Braun, J.-L. Fraikin, L. J. Swenson, N. O. Reich, and A. N. Cleland, "A feasible approach to all-electronic digital labeling and readout for cell identification," *Lab. Chip*, vol. 7, no. 4, p. 469, 2007.
- [86] U. Hassan and R. Bashir, "Electrical cell counting process characterization in a microfluidic impedance cytometer," *Biomed. Microdevices*, vol. 16, no. 5, pp. 697–704, Oct. 2014.
- [87] C. H. Clausen, G. E. Skands, C. V. Bertelsen, and W. E. Svendsen, "Coplanar Electrode Layout Optimized for Increased Sensitivity for Electrical Impedance Spectroscopy," *Micromachines*, vol. 6, no. 1, pp. 110–120, Dec. 2014.
- [88] T. Lanz, S. Hafizovic, J. Rothe, R. Streichan, N. Goedecke, F. Heer, and A. Hierlemann, "Differential impedance spectrometer and vision system for analysis of single cells," in *TRANSDUCERS 2009 - 2009 International Solid-State Sensors, Actuators and Microsystems Conference*, 2009, pp. 1297–1300.
- [89] G. Benazzi, D. Holmes, T. Sun, M. C. Mowlem, and H. Morgan, "Discrimination and analysis of phytoplankton using a microfluidic cytometer," *IET Nanobiotechnology IET*, vol. 1, no. 6, pp. 94–101, Dec. 2007.
- [90] C. Küttel, E. Nascimento, N. Demierre, T. Silva, T. Braschler, P. Renaud, and A. G. Oliva, "Label-free detection of *Babesia bovis* infected red blood cells using impedance spectroscopy on a microfabricated flow cytometer," *Acta Trop.*, vol. 102, no. 1, pp. 63–68, Apr. 2007.
- [91] E. Du, S. Ha, M. Diez-Silva, M. Dao, S. Suresh, and A. P. Chandrakasan, "Electric impedance microflow cytometry for characterization of cell disease states," *Lab. Chip*, vol. 13, no. 19, pp. 3903–3909, Aug. 2013.
- [92] C. Grenvall, C. Antfolk, C. Z. Bisgaard, and T. Laurell, "Two-dimensional acoustic particle focusing enables sheathless chip Coulter counter with planar electrode configuration," *Lab. Chip*, vol. 14, no. 24, pp. 4629–4637, Nov. 2014.
- [93] T. Sun, N. G. Green, S. Gawad, and H. Morgan, "Analytical electric field and sensitivity analysis for two microfluidic impedance cytometer designs," *IET Nanobiotechnology IET*, vol. 1, no. 5, pp. 69–79, Oct. 2007.

- [94] S. C. Bürgel, Z. Zhu, N. Haandbæk, O. Frey, and A. Hierlemann, “Dynamic and static impedance spectroscopy for single particle characterization in microfluidic chips,” in *2012 IEEE 25th International Conference on Micro Electro Mechanical Systems (MEMS)*, 2012, pp. 1033–1036.
- [95] L. Wang, L. Flanagan, and A. P. Lee, “Side-Wall Vertical Electrodes for Lateral Field Microfluidic Applications,” *J. Microelectromechanical Syst.*, vol. 16, no. 2, pp. 454–461, Apr. 2007.
- [96] G. Schade-Kampmann, A. Huwiler, M. Hebeisen, T. Hessler, and M. Di Berardino, “On-chip non-invasive and label-free cell discrimination by impedance spectroscopy,” *Cell Prolif.*, vol. 41, no. 5, pp. 830–840, Oct. 2008.
- [97] D. Holmes, T. Sun, H. Morgan, J. Holloway, J. Cakebread, and D. Davies, “Label-Free Differential Leukocyte Counts Using a Microfabricated, Single-Cell Impedance Spectrometer,” in *2007 IEEE Sensors*, 2007, pp. 1452–1455.
- [98] V. S. Hollis, J. A. Holloway, S. Harris, D. Spencer, C. van Berkel, and H. Morgan, “Comparison of Venous and Capillary Differential Leukocyte Counts Using a Standard Hematology Analyzer and a Novel Microfluidic Impedance Cytometer,” *PLoS ONE*, vol. 7, no. 9, Sep. 2012.
- [99] D. Holmes, D. Pettigrew, C. H. Reccius, J. D. Gwyer, C. van Berkel, J. Holloway, D. E. Davies, and H. Morgan, “Leukocyte analysis and differentiation using high speed microfluidic single cell impedance cytometry,” *Lab. Chip*, vol. 9, no. 20, pp. 2881–2889, Oct. 2009.
- [100] M. Evander, A. J. Ricco, J. Morser, G. T. A. Kovacs, L. L. K. Leung, and L. Giovangrandi, “Microfluidic impedance cytometer for platelet analysis,” *Lab. Chip*, vol. 13, no. 4, pp. 722–729, Jan. 2013.
- [101] D. Spencer, V. Hollis, and H. Morgan, “Microfluidic impedance cytometry of tumour cells in blood,” *Biomicrofluidics*, vol. 8, no. 6, p. 64124, Nov. 2014.
- [102] N. Haandbæk, S. C. Bürgel, F. Rudolf, and A. Hierlemann, “Characterization of Single Yeast Cell Phenotypes Using Microfluidic Impedance Cytometry and Optical Imaging,” *ACS Sens. Artic. ASAP*, Jul. 2016.
- [103] N. Haandbæk, S. C. Bürgel, F. Heer, and A. Hierlemann, “Characterization of subcellular morphology of single yeast cells using high frequency microfluidic impedance cytometer,” *Lab. Chip*, vol. 14, no. 2, pp. 369–377, Dec. 2013.
- [104] C. Bernabini, D. Holmes, and H. Morgan, “Micro-impedance cytometry for detection and analysis of micron-sized particles and bacteria,” *Lab. Chip*, vol. 11, no. 3, pp. 407–412, Feb. 2011.
- [105] C. Iliescu, D. P. Poenar, M. Carp, and F. C. Loe, “A microfluidic device for impedance spectroscopy analysis of biological samples,” *Sens. Actuators B Chem.*, vol. 123, no. 1, pp. 168–176, Apr. 2007.

- [106] N. Demierre, T. Braschler, P. Linderholm, U. Seger, H. van Lintel, and P. Renaud, "Characterization and optimization of liquid electrodes for lateral dielectrophoresis," *Lab. Chip*, vol. 7, no. 3, pp. 355–365, Mar. 2007.
- [107] C. Yu, J. Vykoukal, D. M. Vykoukal, J. A. Schwartz, L. Shi, and P. R. C. Gascoyne, "A three-dimensional dielectrophoretic particle focusing channel for microcytometry applications," *J. Microelectromechanical Syst.*, vol. 14, no. 3, pp. 480–487, 2005.
- [108] J.-W. Choi, S. Rosset, M. Niklaus, J. R. Adleman, H. Shea, and D. Psaltis, "3-dimensional electrode patterning within a microfluidic channel using metal ion implantation," *Lab. Chip*, vol. 10, no. 6, pp. 783–788, Mar. 2010.
- [109] J. Ozhikandathil, S. Badilescu, and M. Packirisamy, "Synthesis and characterization of silver-PDMS nanocomposite for the biosensing applications," *Proc SPIE*, vol. 50, no. 4, pp. 8007–8017, 2011.
- [110] Y. Wei, Z. Xu, M. A. Cachia, J. Nguyen, Y. Zheng, C. Wang, and Y. Sun, "Embedded silver PDMS electrodes for single cell electrical impedance spectroscopy," *J. Micromechanics Microengineering*, vol. 26, no. 9, p. 95006, 2016.
- [111] A.-L. Deman, M. Brun, M. Quatresous, J.-F. Chateaux, M. Frenea-Robin, N. Haddour, V. Semet, and R. Ferrigno, "Characterization of C-PDMS electrodes for electrokinetic applications in microfluidic systems," *J. Micromechanics Microengineering*, vol. 21, no. 9, p. 95013, 2011.
- [112] A. Pavesi, F. Piraino, G. B. Fiore, K. M. Farino, M. Moretti, and M. Rasponi, "How to embed three-dimensional flexible electrodes in microfluidic devices for cell culture applications," *Lab. Chip*, vol. 11, no. 9, pp. 1593–1595, May 2011.
- [113] L. Wang, L. A. Flanagan, N. L. Jeon, E. Monuki, and A. P. Lee, "Dielectrophoresis switching with vertical sidewall electrodes for microfluidic flow cytometry," *Lab. Chip*, vol. 7, no. 9, pp. 1114–1120, Aug. 2007.
- [114] J. Voldman, M. Toner, M. L. Gray, and M. A. Schmidt, "Design and analysis of extruded quadrupolar dielectrophoretic traps," *J. Electrostat.*, vol. 57, no. 1, pp. 69–90, 2003.
- [115] N. C. Hogan, G. Talei-Franzesi, O. Abudayyeh, A. Taberner, and I. Hunter, "Low-cost, flexible polymer arrays for long-term neuronal culture," *Conf. Proc. Annu. Int. Conf. IEEE Eng. Med. Biol. Soc. IEEE Eng. Med. Biol. Soc. Annu. Conf.*, vol. 2012, pp. 803–806, 2012.
- [116] C. Wang, G. Jia, L. H. Taherabadi, and M. J. Madou, "A novel method for the fabrication of high-aspect ratio C-MEMS structures," *J. Microelectromechanical Syst.*, vol. 14, no. 2, pp. 348–358, Apr. 2005.
- [117] B. Mustin and B. Stoeber, "Low cost integration of 3D-electrode structures into microfluidic devices by replica molding," *Lab. Chip*, vol. 12, no. 22, pp. 4702–4708,

Oct. 2012.

[118] S. Rajaraman, S.-O. Choi, R. H. Shafer, J. D. Ross, J. Vukasinovic, Yoonsu Choi, S. P. DeWeerth, A. Glezer, and M. G. Allen, "Microfabrication technologies for a coupled three-dimensional microelectrode, microfluidic array," *J. Micromechanics Microengineering*, vol. 17, no. 1, p. 163, 2007.

[119] H. Lorenz, M. Despont, P. Vettiger, and P. Renaud, "Fabrication of photo-plastic high-aspect ratio microparts and micromolds using SU-8 UV resist," *Microsyst. Technol.*, vol. 4, no. 3, pp. 143–146.

[120] A. del Campo and C. Greiner, "SU-8: a photoresist for high-aspect-ratio and 3D submicron lithography," *J. Micromechanics Microengineering*, vol. 17, no. 6, p. R81, 2007.

[121] P. M. Dentinger, K. L. Krafcik, K. L. Simison, R. P. Janek, and J. Hachman, "High aspect ratio patterning with a proximity ultraviolet source," *Microelectron. Eng.*, vol. 61–62, pp. 1001–1007, Jul. 2002.

[122] S. Jiguet, A. Bertsch, H. Hofmann, and P. Renaud, "Conductive SU8-silver composite photopolymer," in *Micro Electro Mechanical Systems, 2004. 17th IEEE International Conference on. (MEMS)*, 2004, pp. 125–128.

[123] E. Rollo, S. C. Kilchenmann, E. Bianchi, and C. Guiducci, "Metal-coated silicon micropillars for freestanding 3D-electrode arrays in microchannels," *Sens. Actuators B Chem.*, vol. 185, pp. 713–719, Aug. 2013.

[124] S. C. Kilchenmann, E. Rollo, P. Maoddi, and C. Guiducci, "Metal-Coated SU-8 Structures for High-Density 3-D Microelectrode Arrays," *J. Microelectromechanical Syst.*, vol. 25, no. 3, pp. 425–431, Jun. 2016.

[125] V. M. Blanco Carballo, J. Melai, C. Salm, and J. Schmitz, "Moisture resistance of SU-8 and KMPR as structural material," *Microelectron. Eng.*, vol. 86, no. 4–6, pp. 765–768, Apr. 2009.

[126] Marc J. Madou, *Fundamentals of Microfabrication and Nanotechnology*, 2012th ed. CRC Press.

[127] *MicroChemicals, Photolithography, Theory and Application of Photoresist, Etchants and Solvents*. 2012.

[128] G. J. Brug, A. L. G. van den Eeden, M. Sluyters-Rehbach, and J. H. Sluyters, "The analysis of electrode impedances complicated by the presence of a constant phase element," *J. Electroanal. Chem. Interfacial Electrochem.*, vol. 176, no. 1, pp. 275–295, Sep. 1984.

[129] B. Albert, A. Johnson, J. Lewis, M. Raff, K. Roberts, and P. Walter, *Molecular biology of the cell, 5th edition by B. Alberts, A. Johnson, J. Lewis, M. Raff, K. Roberts, and P. Walter*. Garland Science, 2008.

[130] S. J. F. Cronin and J. M. Penninger, "From T-cell activation signals to signaling

- control of anti-cancer immunity,” *Immunol. Rev.*, vol. 220, pp. 151–168, Dec. 2007.
- [131] M. H. Andersen, D. Schrama, P. thor Straten, and J. C. Becker, “Cytotoxic T Cells,” *J. Invest. Dermatol.*, vol. 126, no. 1, pp. 32–41, Jan. 2006.
- [132] N. Joseph, B. Reicher, and M. Barda-Saad, “The calcium feedback loop and T cell activation: how cytoskeleton networks control intracellular calcium flux,” *Biochim. Biophys. Acta*, vol. 1838, no. 2, pp. 557–568, Feb. 2014.
- [133] B. Reicher and M. Barda-Saad, “Multiple pathways leading from the T-cell antigen receptor to the actin cytoskeleton network,” *FEBS Lett.*, vol. 584, no. 24, pp. 4858–4864, Dec. 2010.
- [134] M. Oh-hora and A. Rao, “Calcium signaling in lymphocytes,” *Curr. Opin. Immunol.*, vol. 20, no. 3, pp. 250–258, Jun. 2008.
- [135] N. P. Restifo, M. E. Dudley, and S. A. Rosenberg, “Adoptive immunotherapy for cancer: harnessing the T cell response,” *Nat. Rev. Immunol.*, vol. 12, no. 4, pp. 269–281, Apr. 2012.
- [136] R. Houot, L. M. Schultz, A. Marabelle, and H. Kohrt, “T-cell-based Immunotherapy: Adoptive Cell Transfer and Checkpoint Inhibition,” *Cancer Immunol. Res.*, vol. 3, no. 10, pp. 1115–1122, Oct. 2015.
- [137] C. S. Hinrichs and S. A. Rosenberg, “Exploiting the curative potential of adoptive T-cell therapy for cancer,” *Immunol. Rev.*, vol. 257, no. 1, pp. 56–71, Jan. 2014.
- [138] S. A. Rosenberg and N. P. Restifo, “Adoptive cell transfer as personalized immunotherapy for human cancer,” *Science*, vol. 348, no. 6230, pp. 62–68, Apr. 2015.
- [139] C. Yee, “Adoptive T cell therapy: Addressing challenges in cancer immunotherapy,” *J. Transl. Med.*, vol. 3, p. 17, 2005.
- [140] K. Perica, J. C. Varela, M. Oelke, and J. Schneck, “Adoptive T Cell Immunotherapy for Cancer,” *Rambam Maimonides Med. J.*, vol. 6, no. 1, Jan. 2015.
- [141] J. Couzin-Frankel, “Breakthrough of the year 2013. Cancer immunotherapy,” *Science*, vol. 342, no. 6165, pp. 1432–1433, Dec. 2013.
- [142] P. Bacher and A. Scheffold, “Flow-cytometric analysis of rare antigen-specific T cells,” *Cytometry A*, vol. 83A, no. 8, pp. 692–701, Aug. 2013.
- [143] L. Kabilan, G. Andersson, F. Lolli, H. P. Ekre, T. Olsson, and M. Troye-Blomberg, “Detection of intracellular expression and secretion of interferon-gamma at the single-cell level after activation of human T cells with tetanus toxoid in vitro,” *Eur. J. Immunol.*, vol. 20, no. 5, pp. 1085–1089, May 1990.
- [144] T. Schmidt and M. Sester, “Detection of Antigen-Specific T Cells Based on Intracellular Cytokine Staining Using Flow-Cytometry,” in *Virus-Host Interactions*, S. M. Bailer and D. Lieber, Eds. Humana Press, 2013, pp. 267–274.
- [145] O. Sabek, M. T. Dorak, M. Kotb, A. O. Gaber, and L. Gaber, “Quantitative

detection of T-cell activation markers by real-time PCR in renal transplant rejection and correlation with histopathologic evaluation,” *Transplantation*, vol. 74, no. 5, pp. 701–707, Sep. 2002.

[146] A. Caruso, S. Licenziati, M. Corulli, A. D. Canaris, M. A. De Francesco, S. Fiorentini, L. Peroni, F. Fallacara, F. Dima, A. Balsari, and A. Turano, “Flow cytometric analysis of activation markers on stimulated T cells and their correlation with cell proliferation,” *Cytometry*, vol. 27, no. 1, pp. 71–76, Jan. 1997.

[147] J. Geginat, F. Sallusto, and A. Lanzavecchia, “Cytokine-driven Proliferation and Differentiation of Human Naive, Central Memory, and Effector Memory CD4+ T Cells,” *J. Exp. Med.*, vol. 194, no. 12, pp. 1711–1720, Dec. 2001.

[148] D. Di Carlo and L. P. Lee, “Dynamic single-cell analysis for quantitative biology,” *Anal. Chem.*, vol. 78, no. 23, pp. 7918–7925, Dec. 2006.

[149] M. Junkin and S. Tay, “Microfluidic single-cell analysis for systems immunology,” *Lab. Chip*, vol. 14, no. 7, p. 1246, 2014.

[150] A. J. Torres, R. L. Contento, S. Gordo, K. W. Wucherpfennig, and J. C. Love, “Functional single-cell analysis of T-cell activation by supported lipid bilayer-tethered ligands on arrays of nanowells,” *Lab. Chip*, vol. 13, no. 1, pp. 90–99, Jan. 2013.

[151] I. Zaretsky, M. Polonsky, E. Shifrut, S. Reich-Zeliger, Y. Antebi, G. Aidelberg, N. Waysbort, and N. Friedman, “Monitoring the dynamics of primary T cell activation and differentiation using long term live cell imaging in microwell arrays,” *Lab. Chip*, vol. 12, no. 23, p. 5007, 2012.

[152] S. Faley, K. Seale, J. Hughey, D. K. Schaffer, S. VanCompernelle, B. McKinney, F. Baudenbacher, D. Unutmaz, and J. P. Wikswo, “Microfluidic platform for real-time signaling analysis of multiple single T cells in parallel,” *Lab. Chip*, vol. 8, no. 10, pp. 1700–1712, Oct. 2008.

[153] H. Zhu, G. Stybayeva, M. Macal, E. Ramanculov, M. D. George, S. Dandekar, and A. Revzin, “A microdevice for multiplexed detection of T-cell-secreted cytokines,” *Lab. Chip*, vol. 8, no. 12, p. 2197, 2008.

[154] M. Kirschbaum, M. S. Jaeger, T. Schenkel, T. Breinig, A. Meyerhans, and C. Duschl, “T cell activation on a single-cell level in dielectrophoresis-based microfluidic devices,” *J. Chromatogr. A*, vol. 1202, no. 1, pp. 83–89, Aug. 2008.

[155] K. Chung, C. A. Rivet, M. L. Kemp, and H. Lu, “Imaging single-cell signaling dynamics with a deterministic high-density single-cell trap array,” *Anal. Chem.*, vol. 83, no. 18, pp. 7044–7052, Sep. 2011.

[156] S. Sarkar, V. Motwani, P. Sabhachandani, N. Cohen, and T. Konry, “T Cell Dynamic Activation and Functional Analysis in Nanoliter Droplet Microarray,” *J. Clin. Cell. Immunol.*, vol. 6, no. 3, Jun. 2015.

[157] D. R. Gossett, H. T. K. Tse, S. A. Lee, Y. Ying, A. G. Lindgren, O. O. Yang,

- J. Rao, A. T. Clark, and D. D. Carlo, "Hydrodynamic stretching of single cells for large population mechanical phenotyping," *Proc. Natl. Acad. Sci.*, vol. 109, no. 20, pp. 7630–7635, May 2012.
- [158] F. F. Delgado, N. Cermak, V. C. Hecht, S. Son, Y. Li, S. M. Knudsen, S. Olcum, J. M. Higgins, J. Chen, W. H. Grover, and S. R. Manalis, "Intracellular Water Exchange for Measuring the Dry Mass, Water Mass and Changes in Chemical Composition of Living Cells," *PLOS ONE*, vol. 8, no. 7, p. e67590, Jul. 2013.
- [159] T. B. Jones, "Basic theory of dielectrophoresis and electrorotation," *IEEE Eng. Med. Biol. Mag.*, vol. 22, no. 6, pp. 33–42, Nov. 2003.
- [160] A. D. Goater and R. Pethig, "Electrorotation and dielectrophoresis," *Parasitology*, vol. 117 Suppl, pp. S177-189, 1998.
- [161] W. M. Arnold and U. Zimmermann, "Rotating-Field-Induced Rotation and Measurement of the Membrane Capacitance of Single Mesophyll Cells of *Avena sativa*," *Z. Für Naturforschung C*, vol. 37, no. 10, pp. 908–915, 2014.
- [162] X. Hu, W. M. Arnold, and U. Zimmermann, "Alterations in the electrical properties of T and B lymphocyte membranes induced by mitogenic stimulation. Activation monitored by electro-rotation of single cells," *Biochim. Biophys. Acta BBA - Biomembr.*, vol. 1021, no. 2, pp. 191–200, Jan. 1990.
- [163] Y. Huang, X.-B. Wang, P. R. C. Gascoyne, and F. F. Becker, "Membrane dielectric responses of human T-lymphocytes following mitogenic stimulation," *Biochim. Biophys. Acta BBA - Biomembr.*, vol. 1417, no. 1, pp. 51–62, Feb. 1999.
- [164] Y. Huang, X. B. Wang, F. F. Becker, and P. R. Gascoyne, "Membrane changes associated with the temperature-sensitive P85gag-mos-dependent transformation of rat kidney cells as determined by dielectrophoresis and electrorotation," *Biochim. Biophys. Acta*, vol. 1282, no. 1, pp. 76–84, Jun. 1996.
- [165] R. Pethig, V. Bressler, C. Carswell-Crumpton, Y. Chen, L. Foster-Haje, M. E. García-Ojeda, R. S. Lee, G. M. Lock, M. S. Talary, and K. M. Tate, "Dielectrophoretic studies of the activation of human T lymphocytes using a newly developed cell profiling system," *ELECTROPHORESIS*, vol. 23, no. 13, pp. 2057–2063, Jul. 2002.
- [166] N. Guan, J. Deng, T. Li, X. Xu, J. T. Irelan, and M.-W. Wang, "Label-free monitoring of T cell activation by the impedance-based xCELLigence system," *Mol. Biosyst.*, vol. 9, no. 5, pp. 1035–1043, May 2013.
- [167] S. Gawad, D. Holmes, G. Benazzi, P. Renaud, and H. Morgan, "Impedance spectroscopy and optical analysis of single biological cells and organisms in microsystems," *Methods Mol. Biol. Clifton NJ*, vol. 583, pp. 149–182, 2010.
- [168] F. Borrego, M. J. Robertson, J. Ritz, J. Peña, and R. Solana, "CD69 is a stimulatory receptor for natural killer cell and its cytotoxic effect is blocked by CD94 inhibitory receptor," *Immunology*, vol. 97, no. 1, pp. 159–165, May 1999.

- [169] D. M. Vykoukal, P. R. C. Gascoyne, and J. Vykoukal, "Dielectric characterization of complete mononuclear and polymorphonuclear blood cell subpopulations for label-free discrimination," *Integr. Biol.*, vol. 1, no. 7, p. 477, 2009.
- [170] A. L. Maizel, S. R. Mehta, S. Hautf, D. Franzini, L. B. Lachman, and R. J. Ford, "Human T lymphocyte/monocyte interaction in response to lectin: kinetics of entry into the S-phase.," *J. Immunol.*, vol. 127, no. 3, pp. 1058–1064, 1981.
- [171] D. Spencer and H. Morgan, "Positional dependence of particles in microfluidic impedance cytometry," *Lab. Chip*, vol. 11, no. 7, p. 1234, 2011.
- [172] H. Morgan, T. Sun, D. Holmes, S. Gawad, and N. G. Green, "Single cell dielectric spectroscopy," *J. Phys. Appl. Phys.*, vol. 40, no. 1, p. 61, Jan. 2007.
- [173] T. Sun and H. Morgan, "Single-cell microfluidic impedance cytometry: a review," *Microfluid. Nanofluidics*, vol. 8, no. 4, pp. 423–443, Mar. 2010.
- [174] S. Kumari, S. Curado, V. Mayya, and M. L. Dustin, "T cell antigen receptor activation and actin cytoskeleton remodeling," *Biochim. Biophys. Acta*, vol. 1838, no. 2, pp. 546–556, Feb. 2014.
- [175] G. Setterfield, R. Hall, T. Bladon, J. Little, and J. G. Kaplan, "Changes in structure and composition of lymphocyte nuclei during mitogenic stimulation.," *J. Ultrastruct. Res.*, vol. 82, no. 3, pp. 264–282, Mar. 1983.
- [176] Samuel, Kilchenmann, Enrica, Rollo, and Carlotta, Guiducci, "Vertical Electrodes based on Metal-Coated SU-8 Structures," presented at the IEEE Engineering in Medicine and Biology Society, Milan, 2015.
- [177] Samuel, Kilchenmann, Iness, Benmessaoud1, Hacer, Arik, Laszlo Forro, and Carlotta, Guiducci, "A fully automated electrorotation system based on 3-D electrodes integrated in microfluidic channels."
- [178] E. Rollo, E. Bianchi, S. Kilchenmann, F. M. Bellati, E. Accastelli, and C. Guiducci, "Detecting particles flowing through interdigitated 3D microelectrodes," in *2012 Annual International Conference of the IEEE Engineering in Medicine and Biology Society*, San Diego, 2012, pp. 5002–5005.
- [179] Enrica, Rollo, Enrico, Tenaglia, Andrea Joseph, De Micheli, Raphael, Genolet, Alexandre, Harari, and Carlotta, Guiducci, "Label-Free Strategy for Single-Cell Detection of in Vitro Activated T Lymphocytes," presented at the IEEE Engineering in Medicine and Biology Society, Milan, 2015.
- [180] Enrica, Rollo, Enrico, Tenaglia, Raphael, Genolet, Alexandre, Harari, and Carlotta, Guiducci, "A 3D pillars impedance-based strategy for the discrimination of in vitro activated T-lymphocytes," presented at the MicroTAS, Dublin, 2016.
- [181] D. Kim, E. Choi, S. S. Choi, S. Lee, J. Park, and K.-S. Yun, "Measurement of Single-Cell Deformability Using Impedance Analysis on Microfluidic Chip," *Jpn. J. Appl. Phys.*, vol. 49, no. 12, p. 127002, Dec. 2010.

-
- [182] Z. Zhu, O. Frey, D. S. Ottoz, F. Rudolf, and A. Hierlemann, “Microfluidic single-cell cultivation chip with controllable immobilization and selective release of yeast cells,” *Lab. Chip*, vol. 12, no. 5, pp. 906–915, 2012.
- [183] D. Malleo, J. T. Nevill, L. P. Lee, and H. Morgan, “Continuous differential impedance spectroscopy of single cells,” *Microfluid. Nanofluidics*, vol. 9, no. 2–3, pp. 191–198, Aug. 2010.
- [184] L.-S. Jang and M.-H. Wang, “Microfluidic device for cell capture and impedance measurement,” *Biomed. Microdevices*, vol. 9, no. 5, pp. 737–743, May 2007.
- [185] H. S. Kim, Y. H. Cho, A. B. Frazier, Z. G. Chen, D. M. Shin, and A. Han, “Whole Cell Impedance Analysis of Metastatic and Non-Metastatic Cancer Cells,” in *IEEE 22nd International Conference on Micro Electro Mechanical Systems, 2009. MEMS 2009*, 2009, pp. 399–402.
- [186] Y. Zhou, S. Basu, E. D. Laue, and A. A. Seshia, “Dynamic monitoring of single cell lysis in an impedance-based microfluidic device,” *Biomed. Microdevices*, vol. 18, 2016.
- [187] Y. Zhou, S. Basu, E. Laue, and A. A. Seshia, “Single cell studies of mouse embryonic stem cell (mESC) differentiation by electrical impedance measurements in a microfluidic device,” *Biosens. Bioelectron.*, vol. 81, pp. 249–258, Jul. 2016.
- [188] W.-H. Tan and S. Takeuchi, “A trap-and-release integrated microfluidic system for dynamic microarray applications,” *Proc. Natl. Acad. Sci. U. S. A.*, vol. 104, no. 4, pp. 1146–1151, Jan. 2007.

CURRICULUM VITAE

Enrica Rollo

MAIL ADDRESS enrica.rollo@gmail.com
BIRTH 20.07.1987
NATIONALITY Italian

- EDUCATION

- 2012- 2016** PhD student in Microsystems and Microelectronics, Laboratory of Life Sciences Electronics, Ecole Polytechnique Fédérale de Lausanne (EPFL).
- 2009-2011** M.Sc. in Biomedical Engineering, Politecnico di Torino, Italy.
- 2006-2009** B.Sc. in Biomedical Engineering, Politecnico di Torino, Italy.

- PROJECTS AND INTERNSHIPS

- 2011** Master's Thesis, Laboratory of Life Sciences Electronics, Ecole Polytechnique Fédérale de Lausanne (EPFL).
- 2009** Im3D S.p.A.- Medical Imaging Lab, Torino.

- PUBLICATIONS

- 2016** E. Rollo, E. Tenaglia, R. Genolet, A. HararI, G. Coukos and C. Guiducci- "Label-free identification of activated T lymphocytes through 3D electrode-based impedance microsensors on chip" (under review).
- 2016** E. Rollo, E. Tenaglia, R. Genolet, A. HararI and C. Guiducci. "A 3d pillars impedance-based strategy for the discrimination of in vitro activated t-lymphocytes". Conference paper, MicroTAS, Dublin, Ireland.
- 2016** S. C. Kilchenmann, E. Rollo, P. Maoddi, C. Guiducci. "Metal-coated SU-8 structures for high density 3D microelectrode arrays". IEEE Journal of Microelectromechanical Systems.

- 2013** E. Rollo and S. C. Kilchenmann, E. Bianchi, C. Guiducci. “Metal-coated silicon micropillars for freestanding 3D-electrode arrays in microchannels”. *Sensor and Actuators B: Chemical*, (185), (2013), pp. 713–719.
- 2012** E. Rollo and E. Bianchi, S. Kilchenmann, F. Bellati, and C. Guiducci. “Detecting Particles Flowing through Interdigitated 3D Microelectrodes”. Conference paper, 34th Annual International Conference of the IEEE Engineering in Medicine & Biology Society, San Diego, California, USA.

